Chapter 1. The Martian Environment

1.1 Introduction

Among our discoveries concerning Mars, one stands out above all others: the possible presence of liquid water either in the ancient past or preserved in the subsurface today. Since the announcement that fossils may have been found in Martian meteorite ALH 84001 (McKay *et al.*, 1996) there has been renewed interest in the search for water on Mars as prerequisite for life (Briggs, 2000). Habitability is a complex subject that depends on many different factors (Cockell *et al.,* 2016) and so finding water alone is not proof that a planet is habitable, but water appears to be a necessary condition for life as we know it (Jones and Lineweaver, 2010; 2012). Since neither pure liquid water nor brines are likely to exist on the Martian surface for more than a few hours (Martinez and Renno, 2013; Fischer et al., 2013; 2014), we seek to extend this search into the subsurface where conditions are more favorable (Clifford, 1993).

Pure liquid water is unlikely to exist on the surface of Mars due to several environmental factors. For one, the average surface temperature of the planet is below the freezing point of water. This implies that any water found would likely take the form of ice. Another consideration is that the atmospheric pressure is below the partial pressure of water vapor. This means that any liquid water present on the surface would quickly boil away. Finally, measurements of the water vapor abundance in the Martian atmosphere suggest that the atmosphere is extremely dry. This has the implication that any liquid water present on the surface would evaporate and is transient

in nature. These three factors limit the locations and times at which pure liquid water may occur on Mars.

The discovery of perchlorate salts (Hecht *et al.,* 2009; Kounaves *et al.,* 2010; 2014) and evidence for brines (Renno *et al.,* 2009) by the Phoenix lander may imply that liquid saline solutions are more likely than previously thought. This is significant because when salts dissolve in water; the freezing point temperature, saturation water vapor pressure, and evaporation rate is lowered. The minimum temperature at which the brine of a given salt can be liquid is known as the solution eutectic temperature, T_e, and there are several brines with eutectic temperatures lower than 210 K that might exist on Mars (Martinez and Renno, 2013). In fact, even NaCl which has a relatively high eutectic temperature at 252 K may allow liquid water to form sporadically on the surface of Mars (Haberle *et al.*, 2001). Recent research conducted by Gough *et al.* (2011; 2014), Nuding *et al.* (2014) and Nikolakakos *et al.* (2015) has shown that liquid saline solutions can form at small scales via deliquescence of atmospheric water vapor on various perchlorate salts found on Mars. However, experiments at Martian conditions by Elliott *et al.* (2012) and Fischer *et al.* (2013; 2014) have shown that this process may be inhibited by low pressures which will reduce the number of water molecules available to bind to the salt. Fischer *et al.* was able to observe the melting of solid ice to form an aqueous solution in the presence of those same salts but noted a significant depletion in the amount of water present in the sample cells due to evaporation.

Based on the discussion above, we can say that it is likely that there are regions of Mars where the conditions are right to form brine pockets but these brines will be small, short lived and transient in nature. Alas, we are unlikely to find a pool or puddle of water which is stable on

the surface Mars. However, we may still be able to find sub-surface aquifers and regions where salty soils absorb and emit water vapor over seasonal and diurnal time scales. The search for present-day water on Mars calls for an investigation of the subsurface and this work seeks to answer that call.

1.2 Ground Penetrating Radar

Remote detection of brines is a challenge because it requires us to peer beneath the surface of the planet. Two ground penetrating radars (GPR) have already flown on Martian orbiters: MARSIS on ESA's Mars Express mission and SHARAD on NASA's Mars Reconnaissance Orbiter. While the orbiters are able to look for ice (Holt, *et al.* 2008) and map dielectric properties of the large-scale subsurface of Mars (Mouginot *et al.,* 2014), they are limited in spatial resolution and more importantly temporal resolution because they do not sample the diurnal cycle. Both spacecraft are sun-synchronous and will pass any given point on the surface at the same time each day in order to provide consistent illumination for cameras and other imaging instruments. Mounting a GPR on a lander or rover could solve this problem and allow measurements throughout the day. Grant *et al.* (2003) first proposed a prototype GPR for the mission that later became known as the Mars Science Laboratory Rover, but it was not flown. Fortunately, NASA's 2020 Mars Rover will fly the RIMFAX GPR (Hamran *et al.,* 2015) and ESA's Exomars Rover will fly the WISDOM GPR (Corbel *et al.,* 2006), but both of these missions will land on the equatorial region where brines are less likely to form. Therefore, investigation of another technique to search for brine on Mars led us to the use of interferometric GNSS-R in the context of Earth science and whether this technique could be applied to telecommunications signals transmitted or received by a spacecraft on Mars.

1.3 Interferometric GNSS-R

A relatively new technique, Global Navigation Satellite Systems Reflectometry (GNSS-R), offers us the opportunity to determine the dielectric constant of soils (Rodriguez-Alvarez *et al.,* 2009) and snow pack depth (Rodriguez-Alvarez *et al.,* 2011) on Earth. GNSS-R uses pre-existing signals transmitted by Global Navigation Satellite Systems (GNSS) to form a bistatic radar (Larson et al, 2009; Ruf et al., 2012). The direct signal is received through a zenith antenna to determine the relative transmitting and receiving satellite positions and to provide a timing reference. A second antenna pointed downward gathers the signal scattered by the target object's surface, revealing information about such as layer height, relative permittivity, and surface roughness.

In our case, we aim to apply GNSS-R like techniques to transmissions from the Deep Space Network (DSN) transmitters to determine changes in the relative permittivity caused by the formation of brine. The DSN consists of three large Earth-based antennas that provide the telecommunications, navigation, telemetry, and spacecraft commands with far ranging deep space missions, such as Voyager I (Imbriale, 2005). By passively measuring the reflection of these signals off of the surface, it is possible to have a GPR like measurement without the need to carry a dedicated radar instrument on the spacecraft. We created a comprehensive ray tracing model to simulate the signal propagation from the Earth to Mars and that signal's interactions with the surface and subsurface layers. This model was then used to explore the interpretation of the interference patterns resulting from the measurements. The model and technique for the interpretation of the measurements was tested using experimental results and confirm that the technique we propose could be used to detect liquid water (brine) on Mars.

1.4 The Martian Atmosphere: Temperature, Pressure and Humidity on Mars

The Martian atmosphere is composed primarily of CO_2 (96%), N_2 (2%), Ar (2%) and trace amounts of other gases such as CO, H_2O, and CH_4 (Mahaffy *et al.,* 2013). The atmospheric pressure varies with season and location with a range from about 650 Pa to 1050 Pa at previous landing sites (Martinez *et al.,* 2017). To put this in perspective, the mean sea level pressure on the Earth is 101,325 Pa meaning the atmospheric pressure at the surface of Mars is a little less than 1% of the value on the Earth's surface. This pressure is roughly analogous to that of the Earth stratosphere. The extremely thin atmosphere on Mars makes for dramatic diurnal temperature swings. Over the course of a day on Mars the equatorial temperatures can swing from 173 K to 293 K (Martínez *et al.,* 2017) and at the poles, temperatures can dip as low as 148 K. This is below the freezing point of CO_2 (216 K), so on Mars this primary atmospheric constituent freezes out seasonally. This variation in the bulk atmospheric mass as CO_2 condenses on the polar caps is a process called atmospheric collapse, which is the primary cause of the seasonal pressure oscillation. The mean surface temperature is below the freezing point of H_2O (273 K). However, there are such large diurnal and seasonal temperature fluctuations on Mars that temperatures above the freezing point are possible and may allow the presence of liquid water temporarily (Henderson-Sellers and Meadows, 1976).

The Martian atmosphere is extremely dry. Jakosky and Haberle (1992) estimated that the globally averaged column abundance (thickness of liquid water, if the entire column content were condensed onto the surface) to be ~10 precipitable μm (pr μm). For comparison, the corresponding quantity in the Earth's atmosphere is several centimeters; Mars is about 4 orders

of magnitude drier than Earth. Such extreme dryness also makes the presence of water or even ice on the surface at mid to low latitudes unlikely due to the processes of evaporation and sublimation.

For pure water to be stable with respect to evaporation, the partial pressure of water vapor must be higher than the saturation water vapor pressure at the temperature of the water. In the current Martian climate, this condition is never satisfied on the surface. Indeed, the partial pressure of water vapor at the surface of Mars is of the order of ~1 Pa or less (Savijärvi, 1995; Zent *et al.,* 2010; Jones and Lineweaver, 2012). This value is more than two orders of magnitude lower than the saturation water vapor pressure at the triple point (611.73 Pa). Thus, only an extreme augmentation of water vapor pressure could allow pure liquid water to be stable on the surface at these pressures (Martinez and Renno, 2013). Several experiments have been conducted regarding the evaporation rate of liquid water at Martian conditions this varies from 0.04 mm h^{-1} for some brines (Chevrier *et al.,* 2009; Altheide *et al.,* 2009) to as much as 1.35 mm h^{-1} for pure water (Hecht, 2002; Sears and Moore, 2005; Altheide *et al.,* 2009).

1.5 Research Objective

The objective of this research is to test whether an interferometric measurement of soil moisture content and layer depth can be made using the X-band telecommunications system commonly used on interplanetary spacecraft. To do this we will explore two tasks: (1) to create a ray tracing model of the telecom signal and track the direct signal and multipath reflections off the surface and (2) to conduct experiments in the lab validating this model using Mars analog soils.

Chapter 2. The Relative Permittivity of Water, Ice and Soils

2.1 Pure Liquid Water and Brine

Our comprehensive ray tracing model simulates the propagation of radio signal from the Earth to Mars and its interactions with the Mars surface and subsurface. Thus, the relative permittivities of dry Martian regolith, pure water and brine are needed as input to the model. After reviewing the literature, we chose to use the results from Meissner and Wentz (2004) that was developed to predict the relative permittivities of sea water at salt concentrations from 0 to 40 ppt. The inputs to the model are the frequency of the EM wave, the temperature, and the salinity of the water. The output is the complex relative permittivity based on a double Debye relaxation law. The formulas used by Meissner and Wentz (2004) were tested between the temperatures of 253 K and 313 K, and frequencies from 0 to 500 GHz. There are two caveats we must keep in mind when using the formulas proposed by Meissner and Wentz (2004). The first is that they are valid at the upper limit of temperature range for Mars, but fortunately as the temperature decreases we should expect a transition to water ice. The second is that these formulations assume brine of NaCl salt, not the perchlorates we believe would be most relevant on Mars. To our knowledge no data currently exists for the relative permittivity of water at Martian conditions or for perchlorate brines of various concentrations. We consider Meissner and Wentz (2004) a first estimate for brines, but recognize that we should consider liquid brines at Martian conditions in the future.

2.2 H_2O and CO_2 Ice

In the case of ice on Mars, the relative permittivity values of ice of two substances are important: H_2O and CO_2. For H_2O ice, we based our initial estimates on the measurements by Matsuoka *et al.* (1996) for temperatures between 190 and 265 K at a frequency of 10 GHz. We also considered the measurements and models of Hoekstra and Cappillino (1971) which conducted experiments at temperatures as low as 190 K, as well as Vant *et al.* (1974; 1978) and Hallikainen *et al.* (1988). Because we are trying to understand the behavior not just of pure ice, but of an ice formed from brine the model becomes significantly more complicated than that of pure substances. Most of the data available in the literature is for higher temperatures and lower salinities than we might expect on Mars. Still, as a starting point, Ulaby *et al.* (2014) provide a modeling framework that treats sea ice as a mixed phase media of pure H_2O ice, air, and brine inclusions. This model considers the temperature dependence of salinity, but a few questions remain regarding the shape and orientation of these brine inclusions and so this is not complete model for our purposes.

For CO_2 ice, we use the time domain reflectometry values from Pettinelli *et al.,* (2003) at 1 MHz. The values for the real part of the permittivity are relatively flat above 10^4 Hz, but the imaginary part is still decreasing and likely has some high frequency relaxation above 10^6 Hz. This data will suffice for a first test, but ideally direct measurements of the relative permittivity of CO_2 ice should be made at X-band frequencies.

2.3 Soils

Soil is a complex mixed phase media and as such its dielectric constant varies with factors such as soil bulk density (compaction), soil composition (particle size distribution and composition), soil water content, temperature, and salinity (Dobson *et al.* 1985). Soil is composed not only of solids such as rock fragments, minerals, and organic matter, but also liquids such as water and gases (Russell, 1957). Modeling this dielectric mixture presents a challenge because we must consider the soil, bound water, free water, and gases separately. To make matters worse, the dielectric constant of the bound water and free water depend on frequency, temperature, and the salinity of solutions (Hallikainen, et al. 1985; Or and Wraith, 1999; Wraith and Or, 1999).

The dielectric model of the soil that we use considers the particle size of the solid components as well as the mass fraction of water. To classify the particle size we use the same scheme as Russell (1957) which defines gravel as the largest component with a diameter larger than 2.0 mm, then there is sand with particles ranging in size from 2.0 to 0.05 mm, silt from 0.05 to 0.002 mm, and clay with any particle less than 0.002 mm. Using a series of sieves and weighing each family of particles we can then define a texture class based on the mass fraction of gravel, sand, silt, or clay (see Figure 1). This process works by first removing the gravel particles and then determining the percentages of the remaining components. Using Figure 1, we would define a soil with a mass fraction of 60% sand, 10% clay, and 30% silt as a "sandy loam." If this soil also contained 20% or more gravel, we would call this a "gravelly sandy loam." Determining these textures classes is important because they also play a role in the determination of the density and therefore the relative permittivity of the soil.

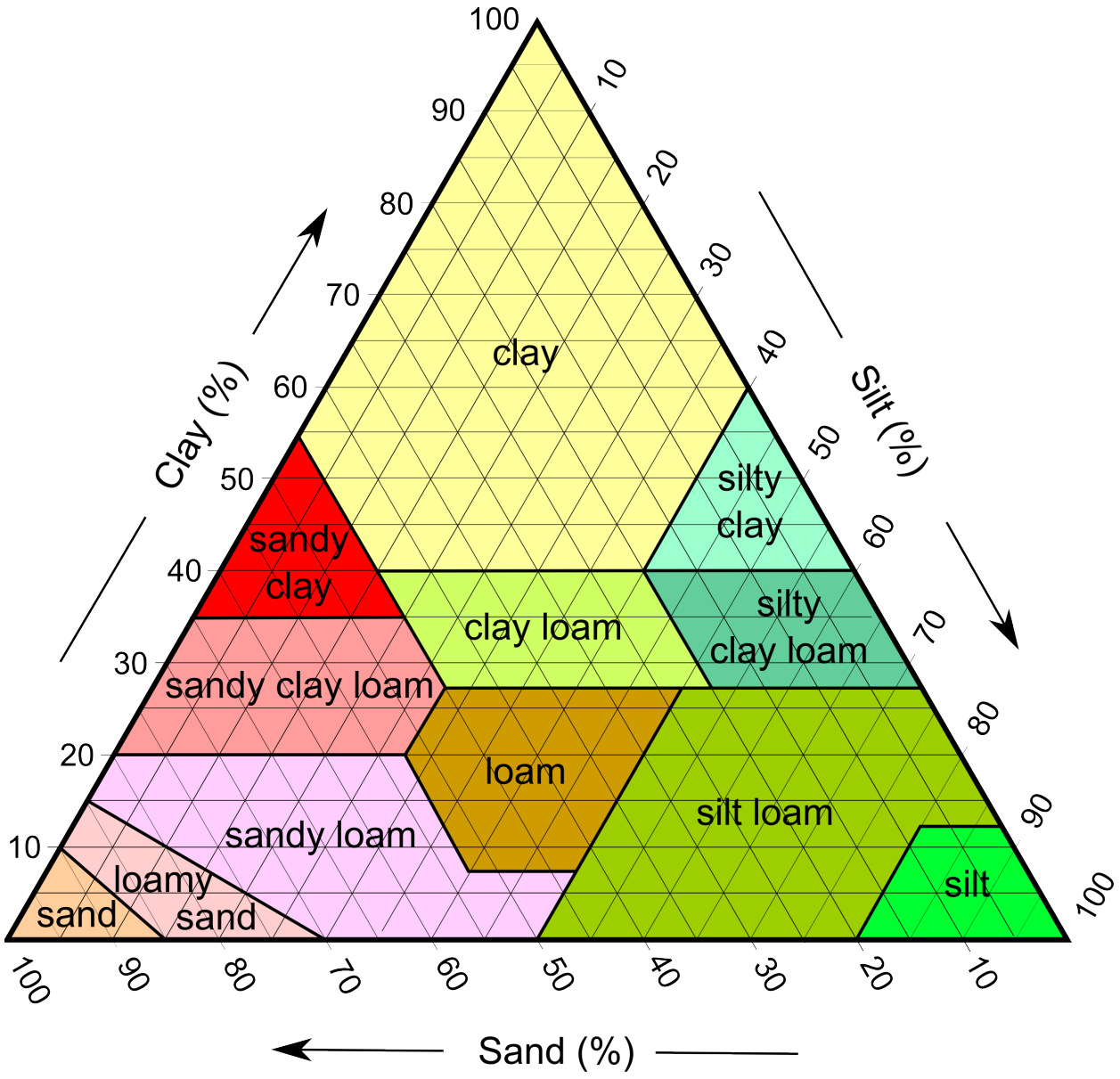

Figure 1. The soil texture categories as defined by the mass fraction of Sand, Silt or Clay (Russell, 1957).

Wang and Schmugge (1980) conducted a review of the existing experimental data and mixing formulas at the time and recognized that none of the existing models provided a good fit to recent experimental data at microwave frequencies and most were unique to a particular soil

type. To address this gap in knowledge, they created a four-component model with a mixture of air, free water, bound water, and rock. To compute the dielectric properties of the free water term, Wang and Schmugge used a modified form of the Debye relation (Cole and Cole 1941, Hoekstra and Delaney 1974). Since the dielectric properties of the bound water were not known the authors introduced the assumption that the dielectric constant of ice would correctly describe this behavior. This work resulted in the first comprehensive model that could be applied to multiple soils at the frequencies of 1.4 and 5 GHz. While Wang and Schmugge's model matched the experimental data well for the real component of the dielectric constant it failed to consistently predict the behavior of the loss factor.

Dobson *et al.* (1985) used new experimental data from Hallikainen *et al.* (1985) to once again revise the previous models. Indeed, Dobson *et al.* (1985) tested two approaches: (i) A revised four-component model using updated values from Wang and Schmugge (1980) and (ii) a new semi-empirical model. In the updated four-component model, Dobson et al. (1985) use the empirical expressions derived by Stogryn (1971) for saline water. They also tested the assumption that ice could be used as a proxy for the bound water term and checked three values: $\varepsilon_{bw} = \varepsilon_{H2O\ ice} = 3.15$, $\varepsilon_{bw} = \varepsilon_{sea\ water}$, and $\varepsilon_{bw} = 35 - 15i$. Showing that the assumption of $\varepsilon_{bw} = 35 - 15i$ yields a better fit to the experimental data than the Wang and Schmugge's assumption of $\varepsilon_{bw} = 3.15$. In our model, we used equations 21 and 22 and the assumption of $\varepsilon_{bw} = 35 - 15i$ from Dobson *et al.* and then combined this with the two Debye relaxation fits for saline water from Meissner and Wentz (2004), equations 6-8 and 11-17. This resulted in a model of the relative permittivity as a function of soil's specific density (ρ_s), volumetric moisture (m_v), temperature (T), and salinity (S) at each frequency (f). Dobson *et al.* (1985)

semi-empirical model is also based upon refractive volumetric mixing (Birchak *et al.* 1974) of four components. Using equations 26-31 from Dobson *et al.* (1985) and the updated empirically derived expression for the effective conductivity in equation 10 from Pelinski *et al.* (1995) we were able to model the relative permittivity based on a soil's composition (% Sand, % Silt, % Clay), bulk density (ρ_b), specific density (ρ_s), volumetric moisture (m_v) at each frequency (f). Both of these relative permittivity models can be used interchangeably in our ray tracing code depending on the soil properties of interest.

Since Dobson *et al.* (1985) several other models have been proposed. Two frequently cited models that we will discuss are Mironov *et al.* (2009) and Park *et al.* (2017). The semi-empirical model in Dobson *et al.* (1985) combines the bound water and free water terms. Park *et al.* and Mironov *et al.* maintain the distinction between the two and divide the soil into three moisture regimes. The driest is when the volumetric mixing ratio of water lies below the wilting point – when the bound water term dominates. Then there is a mixed regime where the volumetric mixing ratio is above the wilting point, but below the porosity. The third is when the volumetric mixing ratio is above the porosity and the relative permittivity of free water dominates. While this method reduces the model error when compared to experiments, it adds complexity to the calculations. Since we were largely interested in the impact of temperature and salinity we mostly focused on the earlier four component model. In future work, it would be worthwhile to investigate the potential of adding the sensitivity to salinity and temperature to the newer models of Mironov (2009) and Park (2017). Some additional work has been done here by Mironov *et al.* (2010) to consider temperature in arctic soils containing permafrost, but more work must be done to incorporate this into our model.

Chapter 3. The EM Propagation Model

3.1 Introduction to Electromagnetic Waves

In order to study the propagation and interference of electromagnetic (EM) waves, we created a comprehensive ray tracing model to track changes to our radio signal as it encounters various mediums such as layered terrain. A ray tracing model works by approximating an EM wave to a narrow beam of radiation which can be traced as it is modified by the mediums through which the radiation passes.

We will begin with the *Helmholtz equation* or *wave equation* for an electric field,

$$\nabla^2 \vec{E} + k^2 \vec{E} = 0, \tag{3.1.1}$$

where $\vec{E}$ is the electric field vector and k is a propagation constant known as the wavenumber (Pozar, 1998). The wave number is given by $k = \omega\sqrt{\mu\epsilon}$ where $\epsilon = \epsilon_r \epsilon_0$ is the absolute permittivity, $\mu = \mu_r \mu_0$ is the absolute permeability, and $\omega = 2\pi f$ is the angular frequency, f is the wave's frequency in Hertz (Hz). The vacuum permittivity $\epsilon_0 = 8.854 \times 10^{-12}$ Faraday/meter (F/m) and the vacuum permeability $\mu_0 = 4\pi \times 10^{-7}$ Henry/meter (H/m) are universal constants while the subscript r denotes a relative term or ratio of these parameters for a specific medium.

If we were to consider a basic plane wave solution to this partial differential equation with an electric field in the $\hat{x}$ direction, magnetic field in the $\hat{y}$ direction, propagating in the $\hat{z}$

direction, and with no variation in the x and y directions ($\frac{\partial}{\partial x} = \frac{\partial}{\partial y} = 0$) then the Helmholtz equation can be simplified to the form,

$$\frac{\partial^2 E_x}{\partial z^z} + k^2 E_x = 0. \tag{3.1.2}$$

There are two independent solutions to this equation, each with the form, $E_x(z) = E_0 e^{\pm ikz}$, where E_0 is an amplitude constant for the initial electric field vector with a magnitude given in units of V/m and $i = \sqrt{-1}$ (Pozar, 1998). If we assume a sinusoidal time dependence we can rewrite this equation as a harmonic in the time domain,

$$\mathcal{E}_x(z,t) = E_0 \, cos(kz \pm \omega t)\,. \tag{3.1.3}$$

Here we will assume a solution in the form of $E_x(z) = E_0 e^{-i\omega t}$ convention to remain consistent with Pozar and Ulaby's texts. To switch between one form and the other with the positive sign convention one must remember to take complex conjugate of the value. Calculating the phase velocity, v_p, or the speed at which a fixed point on the wave travels by we can show that,

$$v_p = \frac{dz}{dt} = \frac{\omega}{k} = \frac{1}{\sqrt{\mu\epsilon}}. \tag{3.1.4}$$

This is known as the *dispersion relation* (Pozar, 1998). In the case of a wave propagating through free space we have the classical solution, $v_p = \mathrm{c} = \frac{1}{\sqrt{\mu_0 \epsilon_0}} = 2.998 \times 10^8 \, m/s$, which is the speed of light. Note that in a media where the relative permittivity and relative permeability are greater than unity then the phase velocity of the wave slows. Each of these waves has a characteristic wavelength, λ, in meters and frequency, f, in Hertz which are related to each other and the phase velocity by,

$$v_p = \lambda \cdot f \tag{3.1.5}$$

Here, we are focusing solely on waves in the radio wave region of the spectrum. While precise definitions can vary, radio waves are generally defined as any EM wave with wavelengths on the order of 1 millimeter to 100 meters or frequencies from 3 MHz to 300 GHz. The electromagnetic spectrum with the radar frequency bands defined by IEEE Standard 521-2002 is shown in Figure 2.

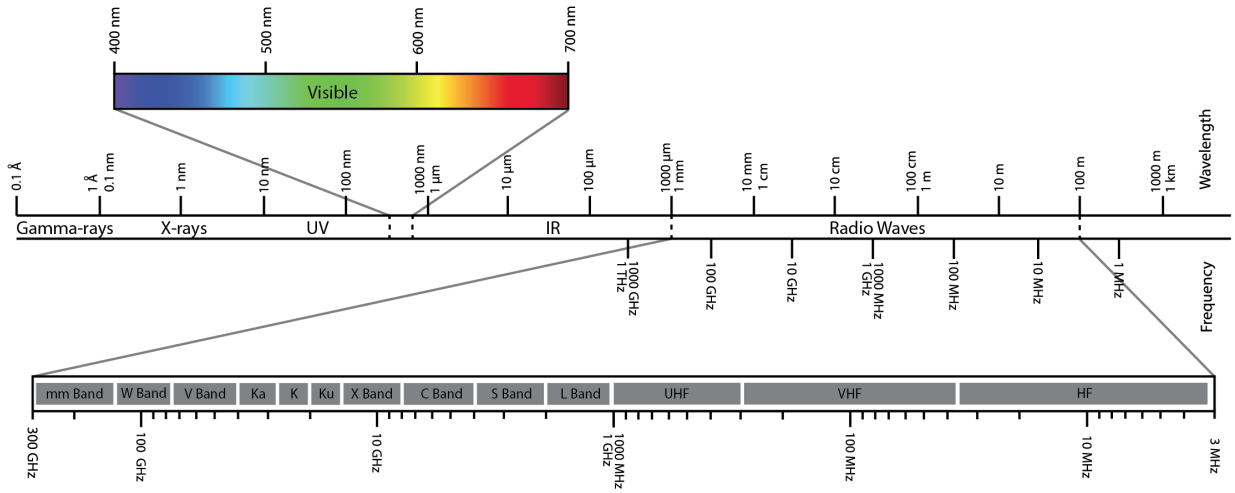

Figure 2. The electromagnetic spectrum with radar frequency bands as defined by IEEE Standard 521-2002.

Much of the work in this thesis focuses on the X-band telecommunications frequencies since radios operating at these frequencies are currently available on spacecraft orbiting Mars. In the broader context of telecommunications science there has been a tendency to move from lower frequencies to higher frequencies over time as technology improves. As a general trend, moving to higher frequencies reduces the physical size of the antenna and allows for a higher data rate, but one downside of this is the larger path loss (Section 3.4). Since the path loss scales with $1/f^2$ using a higher frequency implies a trade between the antenna size and the transmitter power required to close the link budget.

3.2 The Poynting Vector

Now, to quantify the strength of the signal or amount of energy transmitted by an electromagnetic wave we will define a quantity known as the *Poynting vector*, $\overrightarrow{S} = \vec{E} \times \overrightarrow{H}$. The magnitude of the Poynting vector is a measurement of the power density (W/m^2) and its direction is the same as that of the wave's propagation,

$$\langle S \rangle = \frac{1}{2\eta} |E_0|^2, \tag{3.2.1}$$

where $\eta = \omega\mu/k = \sqrt{\mu/\epsilon}$ is called the intrinsic impedance of the medium and E_0 is the amplitude of the electric field vector (V/m) (Ulaby et al., 1981; Pozar, 1998). When we talk about a ray of electromagnetic radiation, we're really talking about visualizing the wave's Poynting vector.

3.3 Polarization of an EM Wave

The polarization of a plane wave refers to the orientation of the electric field vector. In our earlier derivation, we assumed a plane wave with an E-field aligned to the $\hat{x}$ direction and which was propagating in the $\hat{z}$ direction, here we will define this orientation to be the *vertical polarization* (V-pol). We can also imagine a case where in the same coordinate system the plane wave is rotated 90° such that the E-field aligned to the $\hat{y}$ direction and propagating in the $\hat{z}$ direction, we will define this orientation to be the *horizontal polarization* (H-pol). Further, we can consider a case where these two plane waves are superimposed on one another and the E-field traces a curve on the xy-plane. When this curve is a circle, the wave is said to be *circularly polarized*. When it is an ellipse, it is said to be *elliptically polarized*. Finally, we may note that

the tip of the E-field vector moves either in a clockwise or counter-clockwise direction along the $\hat{z}$ direction. If we take our thumbs and orient them in the direction of propagation, we might notice that our fingers of our right-hand point in the counter-clockwise direction while our left-hand points in the clockwise direction. So, if we had a circular wave rotating in the counter-clockwise direction then we would call this a *right-hand circularly polarized* (RHCP) wave and vice versa. This is consistent with the engineering convention in Pozar and Ulaby as opposed to the physics convention which defines the rotation in time.

3.4 Path Loss in Free Space Transmission

This will be the most general case of our ray tracing model. We begin with a radio wave that has some characteristic wavelength, λ, traveling some distance, r_{AB}, from a transmitter at A to a receiver at B (See Figure 3).

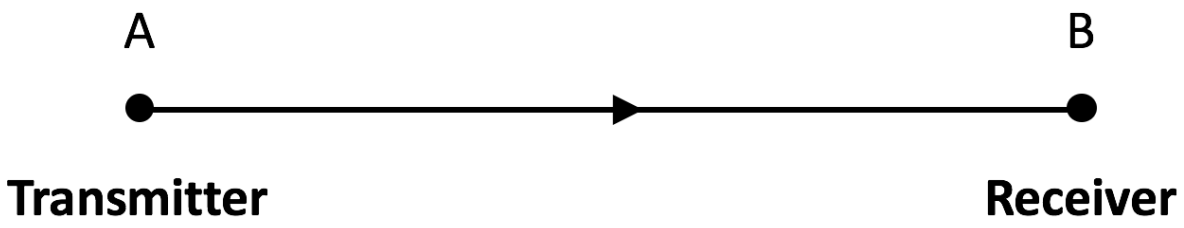

Figure 3. A simple ray tracing model depicting an EM wave as a "pencil" or a "laser beam" of radiation.

If we assume the radiation propagates spherically from the source, we can use the *Friis Transmission Equation* (Pozar, 1998) and assume the use of two isotropic antennas with a gain of 1 to calculate the ratio of the power spectral density (W/m^2) received at B (P_B) relative to the power transmitted from A (P_A),

$$\frac{P_B}{P_A} = \left(\frac{\lambda}{4\pi \cdot r_{A\to B}}\right)^2 . \tag{3.4.1}$$

Converting wavelength to frequency, we can rewrite 3.4.1 as,

$$\frac{P_B}{P_A} = \left(\frac{v_p}{4\pi \cdot r_{A\to B} \cdot f}\right)^2 , \tag{3.4.2}$$

where f is the frequency and v_p is the phase velocity. It is often convenient to give these power ratios in terms of decibel notation and so we could write this power ratio as a loss term known as the path loss,

$$L_{path,A\to B} = -20 \cdot \log_{10}\left(\frac{4\pi \cdot r_{A\to B} \cdot f}{v_p}\right) . \tag{3.4.3}$$

If we wanted to find the magnitude of E-field at B, then we can simply convert back to field quantities using equation 3.2.1,

$$|E_B| = \sqrt{2 \cdot \eta \cdot P_A \cdot 10^{\,L_{path,A\to B}/10}} \tag{3.4.4}$$

3.5 Reflection and Transmission at Interfaces Between Media

Anytime an EM wave travels from one medium to another, there is a potential for the signal to be reflected and/or altered as it is transmitted through the medium. These changes are dictated by the *Fresnel reflection equations*. These equations will be used to predict what fraction of signal is reflected or transmitted, the angle of refraction for the transmitted light, and the phase shift of the signal. The Fresnel reflection equations assume that a plane wave is obliquely incident on a planar interface between two dielectric regions (see Figure 4). In these

equations, we must consider two orientations of the electric field, the first is in the XZ plane (vertical or parallel polarization) and the second is normal to the XZ plane (horizontal or perpendicular polarization). Any incident plane wave may have a polarization that is either V-pol or H-pol or some linear combination of these two cases.

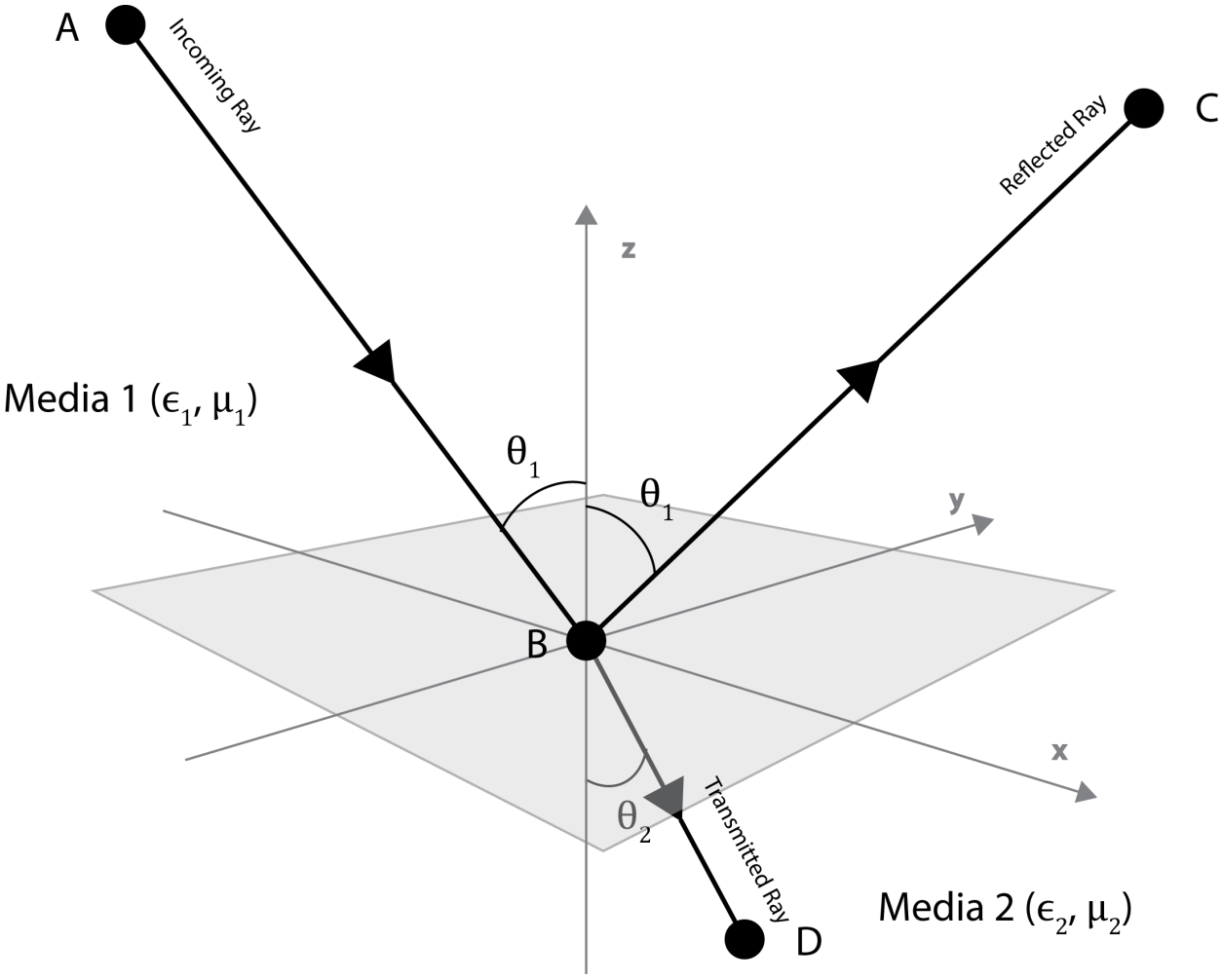

Figure 4. A ray encountering an interface between Media 1 and Media 2 as defined by their dielectric properties, in three dimensions.

Notice that in Figure 4, we marked two angles, θ_1 and θ_2. This is because the ray will continue forward on two paths. The first is the specular reflection, which proceeds back up through media

1 at angle θ_1 to point C. The second is the transmission through the interface into media 2, which continues to propagate forward at angle θ_2, the refraction angle to point D. The refraction angle is related to the incidence angle and the dielectric properties of both media by *Snell's law* (Beckmann, 1967; Ulaby, 1981; Pozar, 1998),

$$\sin\theta_2 = \sqrt{\frac{\mu_1\epsilon_1}{\mu_2\epsilon_2}}\sin\theta_1\,. \tag{3.5.1}$$

Let us also define two new terms, the *reflection coefficient*,

$$R = \frac{E_{reflected}}{E_{incident}}, \tag{3.5.2}$$

and the *transmission coefficient*,

$$T = \frac{E_{transmitted}}{E_{incident}}. \tag{3.5.3}$$

As you might expect, these two terms are related such that the magnitude of the incident ray is equal to the sum of the transmitted and reflected rays,

$$E_{incident} = E_{transmitted} + E_{reflected}, \tag{3.5.4}$$

or,

$$1 = T + R. \tag{3.5.5}$$

To calculate the intensity of the reflected and transmitted e-field we use the Fresnel reflection equations (Beckmann, 1967; Ulaby, 1981; Pozar, 1998). In these calculations the

reflection coefficient, R, is a decimal value between 1 (total transmission) and -1 (total reflection) as the wave traverses from one media to another. Let us also add a subscript to these terms to track the direction of propagation from one media to another. For instance, in the case of a transition from media 1 to media 2 we will use the subscript, $R_{1\to2}$. From media 2 back up into media 1, we will use $R_{2\to1}$. The value of is R as determined by the Fresnel reflection equations is dependent on the polarization and the ratio of the relative impedances of the two media, Z_1 and Z_2,

$$R_{1\to2}(Z_1, Z_2; pol) = \frac{Z_2 - Z_1}{Z_2 + Z_1}. \tag{3.5.6}$$

where the relative impedance of each media and is then given by,

$$Z_i = \begin{cases} \eta_i \cos\theta_i; \ for\ v-pol \\ \eta_i \sec\theta_i; \ for\ h-pol' \end{cases} \tag{3.5.7}$$

and the relative intrinsic impedance,

$$\eta_i = \sqrt{\frac{\mu_i}{\epsilon_i}}\,. \tag{3.5.8}$$

Here we will deviate slightly from the texts and leave the magnetic permeability, μ_i, in the following derivations. Many authors will assume that the magnetic permeability is equal to one (Davis and Chudobiak, 1975; Ulaby et al. 1981; Pozar, 1998) and this approximation works in many cases, but some ferric soils like those we might find on Mars do exhibit magnetic properties (Mullins, 1977). Indeed, Scott (1983) shows that the magnetic permeability for a soil ranges from 1.00001 to 14, with a typical value of 1.0006. The relative permittivity or dielectric

constant, ϵ_i, is some function of the material composition, porosity, and density (for more on this see Chapter 2: The Relative Permittivity of Water, Ice and Soils). Re-evaluating the Fresnel reflection coefficient in terms of the magnetic permeability and relative permittivity we can show that:

$$R_{1\to2}(\epsilon_1, \epsilon_2, \theta_1, \theta_2; v-pol) = \frac{\sqrt{\frac{\mu_2}{\epsilon_2}}\cos\theta_2 - \sqrt{\frac{\mu_1}{\epsilon_1}}\cos\theta_1}{\sqrt{\frac{\mu_1}{\epsilon_1}}\cos\theta_1 + \sqrt{\frac{\mu_2}{\epsilon_2}}\cos\theta_2} \tag{3.5.9}$$

$$R_{1\to2}(\epsilon_1, \epsilon_2, \theta_1, \theta_2; h-pol) = \frac{\sqrt{\frac{\mu_2}{\epsilon_2}}\sec\theta_2 - \sqrt{\frac{\mu_1}{\epsilon_1}}\sec\theta_1}{\sqrt{\frac{\mu_1}{\epsilon_1}}\sec\theta_1 + \sqrt{\frac{\mu_2}{\epsilon_2}}\sec\theta_2}. \tag{3.5.10}$$

Multiplying both the numerator and denominator of the H-pol equation (3.5.10) by both $\cos\theta_1$ and $\cos\theta_2$, we can show:

$$R_{1\to2}(\epsilon_1, \epsilon_2, \theta_1, \theta_2; -pol) = \frac{\sqrt{\frac{\mu_2}{\epsilon_2}}\cos\theta_2 - \sqrt{\frac{\mu_1}{\epsilon_1}}\cos\theta_1}{\sqrt{\frac{\mu_1}{\epsilon_1}}\cos\theta_1 + \sqrt{\frac{\mu_2}{\epsilon_2}}\cos\theta_2} \tag{3.5.11}$$

$$R_{1\to2}(\epsilon_1, \epsilon_2, \theta_1, \theta_2; h-pol) = \frac{\sqrt{\frac{\mu_2}{\epsilon_2}}\cos\theta_1 - \sqrt{\frac{\mu_1}{\epsilon_1}}\cos\theta_2}{\sqrt{\frac{\mu_1}{\epsilon_1}}\cos\theta_2 + \sqrt{\frac{\mu_2}{\epsilon_2}}\cos\theta_1} \tag{3.5.12}$$

To eliminate the dependence on the angle of refraction, we can use Snell's law to re-write the Fresnel reflection coefficients solely in terms of the incidence angle, the dielectric constant of each media and the polarization. We begin this transformation with the trigonometric identify,

$$\cos\theta_2 = \sqrt{1 - \sin^2\theta_2}\,, \tag{3.5.13}$$

when we apply Snell's law (3.5.1), this becomes,

$$\cos\theta_2 = \sqrt{1 - \left(\frac{\mu_1\epsilon_1}{\mu_2\epsilon_2}\right)\sin^2\theta_1}\,. \tag{3.5.14}$$

Inserting 3.5.14 into the Fresnel reflection coefficients and simplifying the terms we can show that:

$$R_{1\to2}(\epsilon_1, \epsilon_2, \theta_1; v-pol) = \frac{\sqrt{1 - \left(\frac{\mu_1\epsilon_1}{\mu_2\epsilon_2}\right)\sin^2\theta_1} - \sqrt{\frac{\mu_1\epsilon_2}{\mu_2\epsilon_1}}\cos\theta_1}{\sqrt{\frac{\mu_1\epsilon_2}{\mu_2\epsilon_1}}\cos\theta_1 + \sqrt{1 - \left(\frac{\mu_1\epsilon_1}{\mu_2\epsilon_2}\right)\sin^2\theta_1}} \tag{3.5.15}$$

$$R_{1\to2}(\epsilon_1, \epsilon_2, \theta_1; h-pol) = \frac{\sqrt{\frac{\mu_2\epsilon_1}{\mu_1\epsilon_2}}\cos\theta_1 - \sqrt{1 - \left(\frac{\mu_1\epsilon_1}{\mu_2\epsilon_2}\right)\sin^2\theta_1}}{\sqrt{1 - \left(\frac{\mu_1\epsilon_1}{\mu_2\epsilon_2}\right)\sin^2\theta_1} + \sqrt{\frac{\mu_2\epsilon_1}{\mu_1\epsilon_2}}\cos\theta_1}. \tag{3.5.16}$$

Figure 5 shows the resulting magnitude (absolute value) of the reflection coefficient for the interface between air and three different surfaces; sea water ($\varepsilon = 54.5 - 36.8i$), wet soil ($\varepsilon = 9.7 - 2.5i$), and dry soil ($\varepsilon = 3.5 - 0.4i$) assuming the simplifying case of $\mu_1 = \mu_2$.

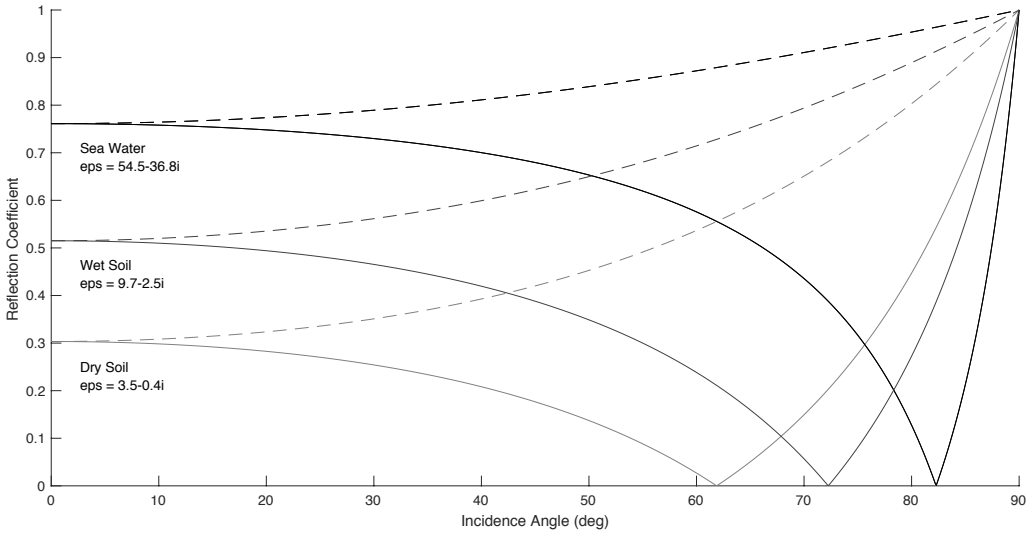

Figure 5. Reflection coefficients for the interface between air and dry soil, wet soil, and sea water; V-pol (solid), H-pol (dashed).

Note that in the case where $\mu_1 = \mu_2$ the H-pol reflection coefficient is relatively simple with a maximum of 1 at 90° incidence angle and a minimum at 0° set by the relative permittivity of the medium. The V-pol reflection coefficient is typically less than the H-pol at a given angle and has a unique minimum for each surface. The incidence angle where the minimum in the V-pol reflection coefficient occurs is known as the *Brewster angle*, θ_b, and this is the point at which the medium perfectly transmits the EM wave as if it were a transparent slab. The Brewster angle can be calculated using Snell's law (3.5.1) when we set $\theta_1 = \theta_b$ and $\theta_2 = 90° - \theta_b$. Now we can show that $\sin(90° - \theta_b) = \cos\theta_b$ and,

$$\theta_b = \tan^{-1}\sqrt{\frac{\mu_2\epsilon_2}{\mu_1\epsilon_1}}. \tag{3.5.17}$$

The Brewster angle is significant because if we can identify the angle in which this minimum in the reflected signal strength occurs, we get a direct measurement of the ratio between the two

relative permittivities. We should note that this is for the special case when $\mu_1 = \mu_2$. If $\mu_1 \neq \mu_2$, it is possible to have a Brewster angle in the H-pol reflection coefficient as well.

Now that we have defined the reflection and transmission coefficients and showed how to calculate these terms we can now calculate the electric field and power density at points C and D, taking care to consider the polarization of the incident wave (See Figure 6).

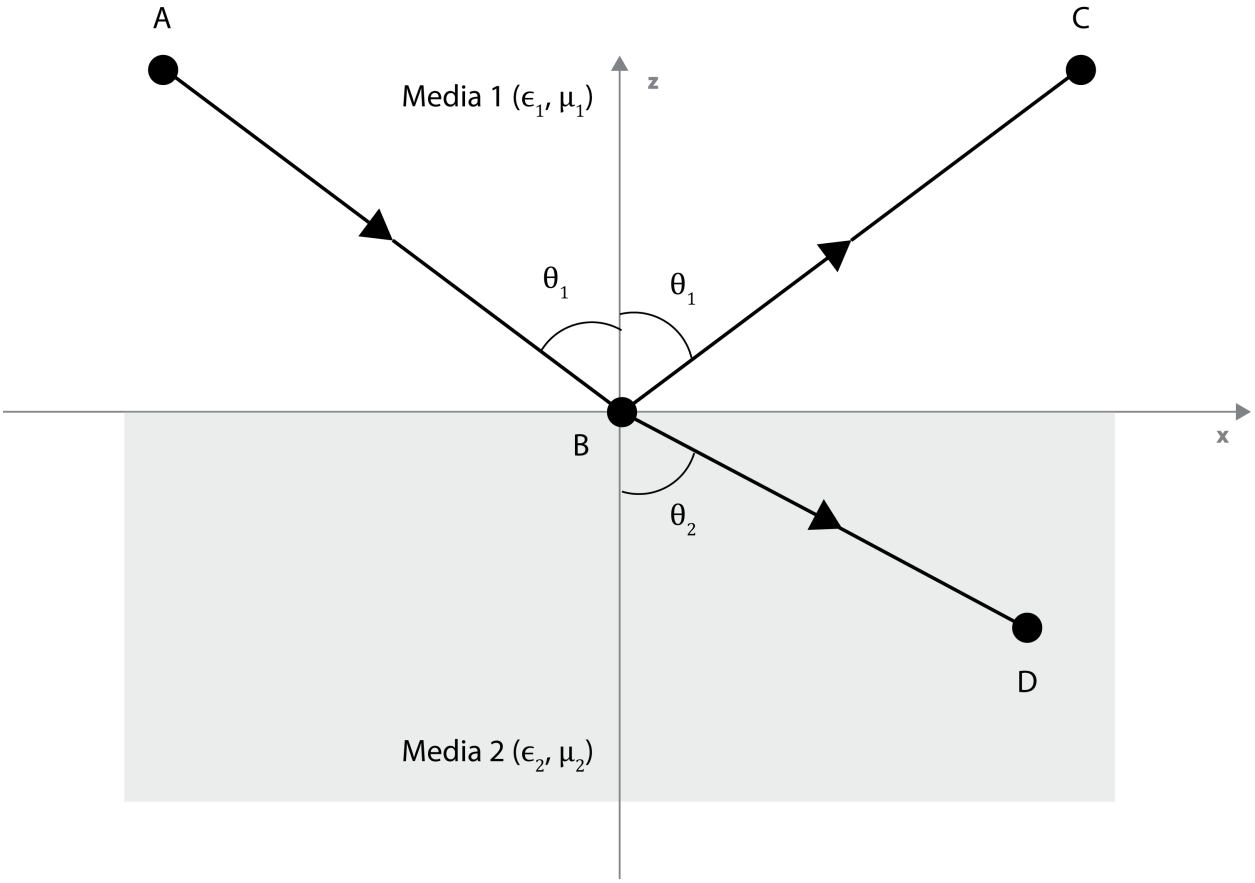

Figure 6. An infinite two-layer model with a ray encountering an interface.

In terms of the E-field,

$$E_{B\ (refl)} = R_{1\to 2} \cdot E_{B\ (inc)} \tag{3.5.18}$$

$$E_{B\ (tran)} = T_{1\to 2} \cdot E_{B\ (inc)} \tag{3.5.19}$$

and so considering the reflection and the total path loss from A to B to C,

$$|E_C| = R_{1\to 2} \cdot \sqrt{2 \cdot \eta \cdot P_A \cdot 10^{\frac{L_{path,A\to B\to C}}{10}}}. \tag{3.5.20}$$

3.6 Absorption Due to a Lossy Media

So far we have considered the path loss and an apparent loss due to transmission or reflection, but there is also another loss factor which we must incorporate into this model, the absorption in a lossy medium. Here we will define a term called the *attenuation constant*,

$$\alpha_i = \frac{2\pi}{\lambda_0}\left|Im\left(\sqrt{\mu_i \epsilon_i}\right)\right| = \frac{2\pi f}{c}\left|Im\left(\sqrt{\mu_i \epsilon_i}\right)\right|, \tag{3.6.1}$$

where λ_0 is the free space wavelength, f is the frequency, c the speed of light, μ_i is the magnetic permeability, and ϵ_i the complex permittivity of each media. If we go back to the equations above and assume that Media 2 is now a lossy material, we can add yet another loss term from B to D (see Figure 7) for the absorption in the media.

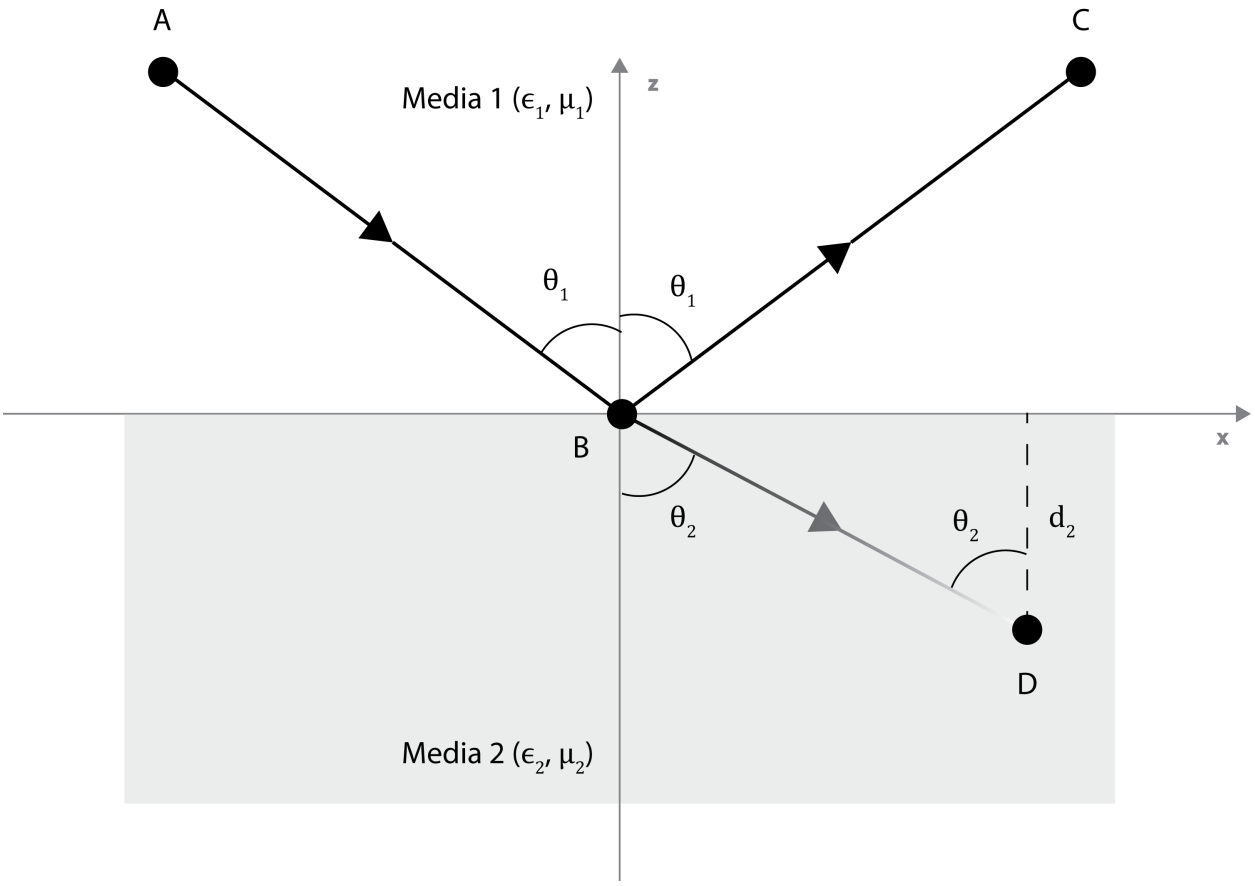

Figure 7. An infinite two-layer model where Media 2 is lossy.

As the plane wave propagates through media 2 we expect the e-field and power to decay exponentially with the attenuation constant giving the rate of decay with distance, $r_{B\to D}$, along the ray's path such that,

$$|E_D| = T_{1\to 2} \cdot e^{-\alpha_2 \cdot r_{B\to D}} \cdot \sqrt{2 \cdot \eta \cdot P_A \cdot 10^{\frac{L_{path,A\to B\to D}}{10}}}. \tag{3.6.2}$$

3.7 Interference Resulting from the Phase Offset Between Two Signals

One thing it's particularly important to track in this model is the phase of the signal. Whenever two EM rays are combined we need to be aware of the potential for constructive and

destructive interference. As we'll see later, the interference pattern resulting from two or more rays combining can tell us a lot about the environment. If we were designing the telecommunications systems solely to transmit data, we would call this multipath interference and try to avoid or mitigate it. However, for this particular science application, the multipath signal due to internal layering is a data product which can provide information about the subsurface structure and composition. To track changes to the phase of the signal we will define another term called the *phase constant*, β_i, which you may note looks very similar to the attenuation constant,

$$\beta_i = \frac{2\pi}{\lambda_0}\left|Re\left(\sqrt{\mu_i \epsilon_i}\right)\right| = \frac{2\pi f}{c}\left|Re\left(\sqrt{\mu_i \epsilon_i}\right)\right|. \tag{3.7.1}$$

Again $\lambda_0$is the free space wavelength, f is the frequency, c the speed of light, μ_i is the magnetic permeability, and ϵ_i the complex permittivity of each media (Pozar, 1998). The phase constant is equivalent to the wave number in lossless medium and it plays a similar role in a lossy medium as well. Since this term controls the phase offset of the E-field it will not change the power of the signal unless two or more rays are added together. When that happens the phase constant will result in an oscillating power term (gain or loss) which changes as a function of the path length or depth of a layer. The phase of the E-field from A to B takes the form,

$$\boldsymbol{\phi}_{A\to B} = \boldsymbol{e}^{\mathbf{i}\cdot\boldsymbol{\beta}_1\cdot\mathbf{r}_{A\to B}}, \tag{3.7.2}$$

B to C would be,

$$\boldsymbol{\phi}_{B\to C} = \boldsymbol{e}^{\mathbf{i}\cdot\boldsymbol{\beta}_1\cdot\mathbf{r}_{B\to C}}, \tag{3.7.3}$$

And B to D would be,

$$\boldsymbol{\phi}_{B\to D} = \boldsymbol{e}^{\mathbf{i}\cdot\boldsymbol{\beta}_2\cdot\mathbf{r}_{B\to D}}. \qquad (\mathbf{3.7.4})$$

If we have two ray paths to the same point, this phase term will create an interference pattern due to the difference in the path length.

Now, there is also a phase shift associated with reflection. When a ray travels from one medium to another with a higher index of refraction there will be a phase shift of 180° or π radians for both the vertical and horizontal polarization of light. If a ray travels from one medium to another with a lower index of refraction, then no phase shift will occur. Other phase shifts can occur for complex values of ϵ_i and μ_i, but these can be neglected in cases where the imaginary component is low.

3.8 Antenna Gain

In addition to the loss terms, it is also possible that there would be gains, particularly when we consider the use of directional antennas. In this section, we will cover how to incorporate a gain term for the transmit and receive antennas. The gain is defined as the ratio of the power received or transmitted along the beam axis relative to a hypothetical isotropic antenna. Note that due to reciprocity in electromagnetism the radiation pattern is the same when an antenna is either transmitting or receiving and so the direction of the transmission does not affect the radiation pattern or gain. This means that when the radiation pattern of an antenna is measured it can be done so either by receiving or transmitting.

Ideally, the gain of each antenna in three dimensions is measured experimentally or simulated. The model written for this work incorporates the co-polarization and cross-

polarization gain of each antenna where θ is the angle of the ray in the vertical axis relative to the bore sight of the main beam. We use the terms co-pol and cross-pol in agreement with the definition giving by Ludwig (1973). This allows us to account for the orientation and alignment of the antennas in our model. The general form of this model input is,

$$Gain_{Effective}\ (\theta_{ant}) = Gain_{Bore-Sight} + Gain\ (\theta_{ant}). \quad (3.8.1)$$

Where the effective gain for each ray is the sum of the bore-sight gain in dB and the antennas radiation pattern. The model then requires the bore-sight gain and radiation or antenna pattern as inputs.

Here, we present several antenna patterns which are used in these simulations. The first is a Pasternack Enterprises PE9857/NF-15 standard gain horns with 37.8° half power beam width. This is a linearly polarized antenna with a bandwidth from 7 to 11 GHz and a bore-sight gain of 15 dB. To calculate the gain for a particular ray, we need to consider the polarization of the ray and the angle at which the ray is incident on the antenna. If the polarization is aligned (vertical to vertical or horizontal to horizontal) with the antenna, then we use the Co-Pol antenna pattern. If it is orthogonal to the antenna (vertical to horizontal or vice versa) then we use the Cross-Pol antenna pattern. Both inputs for the Pasternack PE9857/NF-15 are shown in Figure 8 with the magnitude normalized to the bore-sight gain of the respective radiation pattern.

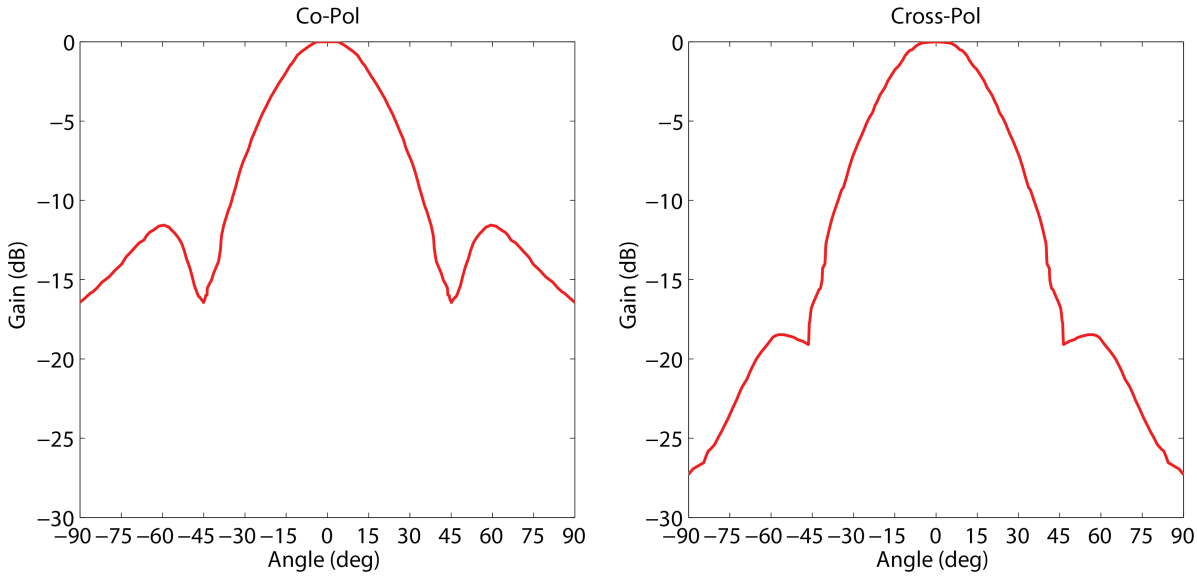

Figure 8. Pasternack PE9857/NF-15 Radiation Pattern.

The second antenna pattern we consider is the high gain antenna mounted on the Mars Science Laboratory Rover "Curiosity" which is expected to fly again on the future Mars 2020 Rover. This RHCP antenna features a 10.6° half power beam width and a bore-sight gain of 25.5 dB for uplink Earth-to-Space (7.145 GHz) and 20.2 dB for downlink (8.395 GHz). If the polarization is aligned (RHCP to RHCP) with the antenna, then we use the Co-Pol antenna pattern if it is inverted relative to the antenna (RHCP to LHCP) then we use the Cross-Pol antenna pattern. The Co-Pol and Cross-Pol antenna patterns for the MSL High Gain Antenna (HGA) were captured from Makovsky et al. (2009). Figure 9 shows both the uplink and downlink radiation pattern for the MSL HGA. All plots are normalized to the bore-sight gain of the Co-Pol radiation pattern at the specified frequency.

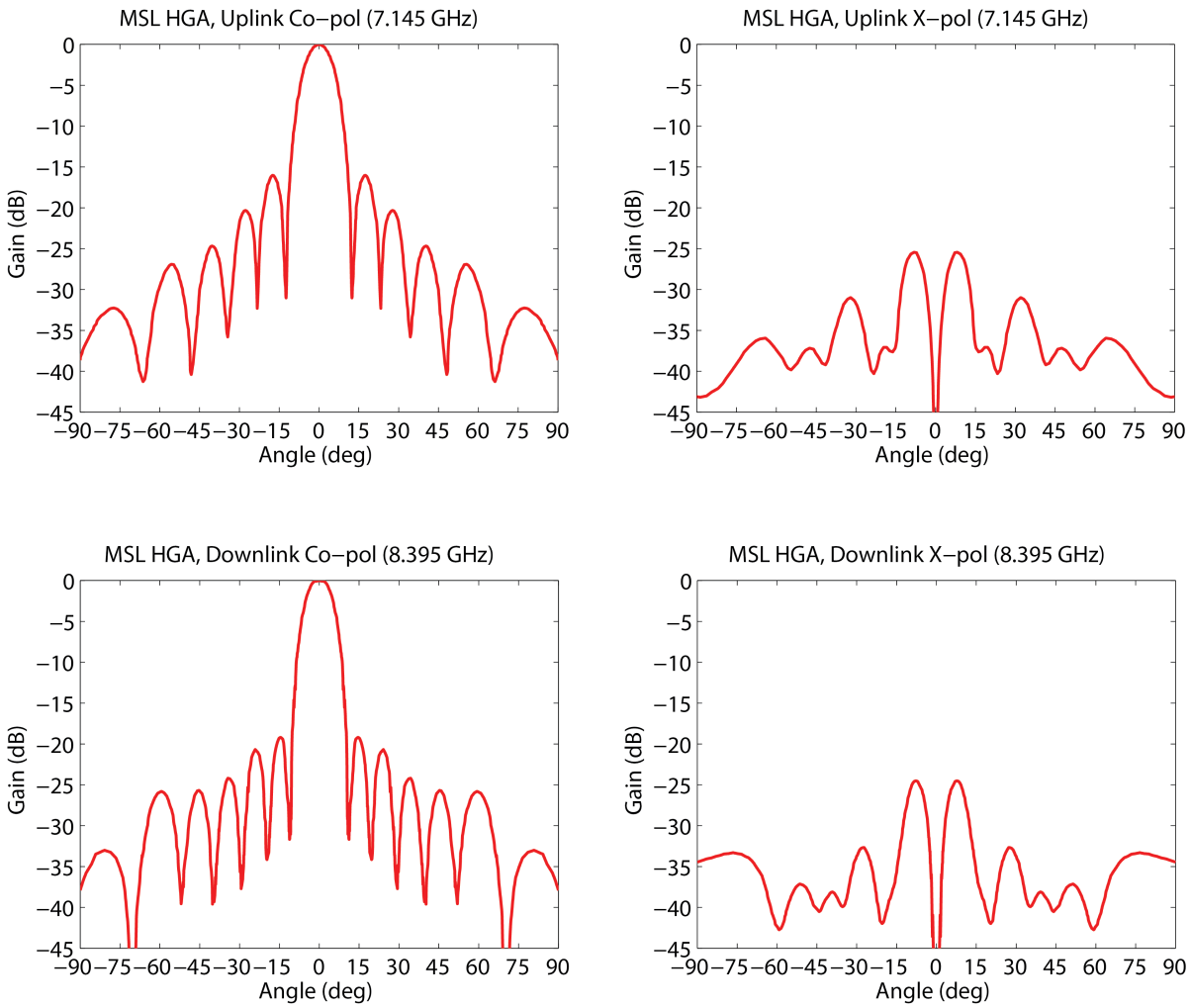

Figure 9. Radiation pattern of the High Gain Antenna on the MSL spacecraft.

In addition to the Mars Science Lab, we will also analyze the Mars Exploration Rovers "Spirit" and "Opportunity." Like MSL, the MER rovers utilize several different antennas during different mission stages. In this case, we are interested in the radiation patterns of High Gain Antenna (HGA), Rover Low Gain Antenna (RLGA), and Petal Low Gain Antenna (PLGA) as reported by Vacchione et al. (2014). The MER HGA shown in Figure 10 features a bore-sight gain of 24.8 dB for uplink Earth-to-Space (7.175 GHz) and 20.5 dB for downlink (8.425 GHz) with a half power beam width of 9.8° (Taylor et al. 2005).

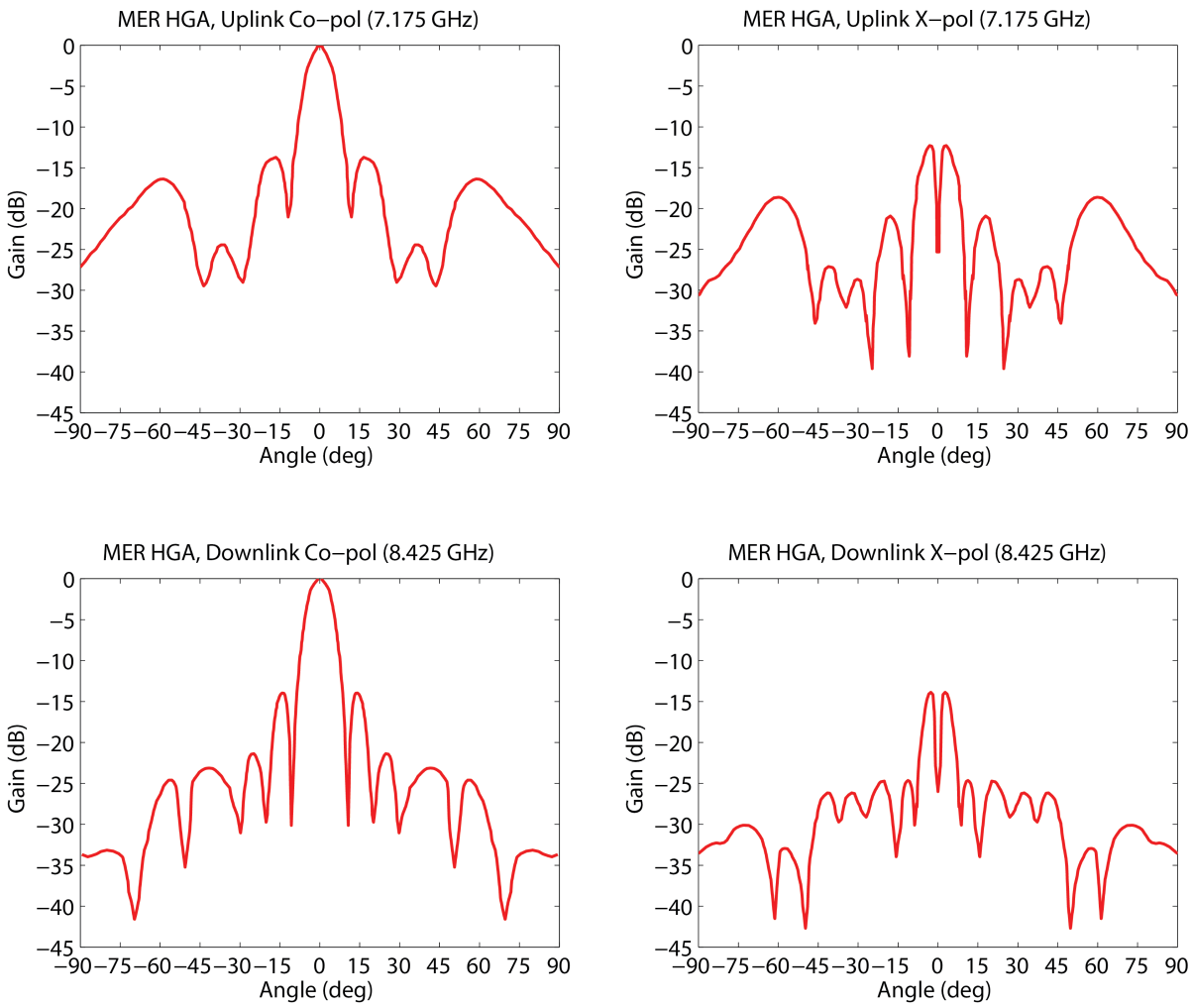

Figure 10. Radiation pattern of the High Gain Antenna on the MER spacecraft.

The two low gain antennas shown in Figure 11 feature a bore-sight gain of 6.89 dB from the rover and 6.0 dB from the landing petal (Taylor et al. 2005). Both antennas operate at 8.425 GHz with a half power beam width of 76.2° and 90.0° respectively, for downlink to Earth.

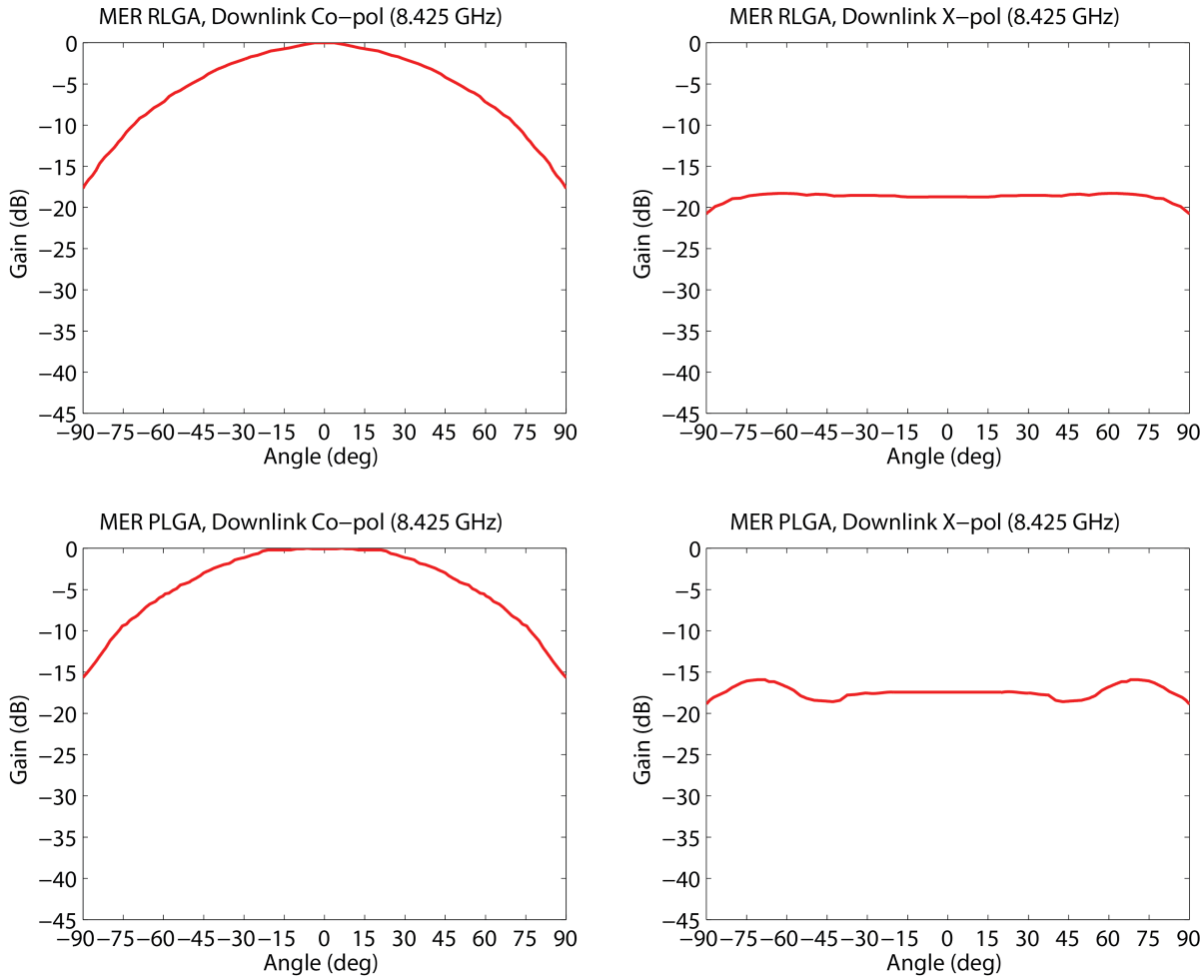

Figure 11. Radiation pattern of the Rover Low Gain Antenna (RLGA) and Petal Low Gain Antenna (PLGA) on the MER spacecraft.

3.9 Doppler Effect Due to Relative Motion

We now have a general form of the Friis Transmission Equation to calculate the power of the received signal as a function of the transmitted power, the distance between the two antennas, the frequency of the signal, and the radiation pattern of the antennas. As a final note on the application of this model, the distance between the transmitter and the receiver is not constant when this technique is applied to transmissions to spacecraft or other planetary bodies. The distance will vary in time due to orbital motions and so we recommend doing a link budget for

the target's perihelion and aphelion. We also note that these equations must also consider the potential for a *Doppler shift* in the frequency due to the relative motion of the planets and spacecraft,

$$f_r = f_t \left(1 + \frac{\Delta v_r}{v_p}\right), \tag{3.9.1}$$

where f_r is the frequency received, v_p the phase velocity of the wave, Δv_r the radial velocity of the receiver relative to the transmitter, and f_t the initial frequency of transmission (Pozar, 1998). This must be accounted for whenever we are simulating the ray path between two objects with a relative motion. For instance, this Doppler shift applies both to a ray path from the DSN transmitter on Earth and a landed spacecraft on Mars and to a ray path between the surface of Mars and a spacecraft orbiting above. We must take care to calculate this frequency shift due to any relative motion along the ray path, however, we can neglect it in the case of our stationary experiments in the lab.

Chapter 4. Model Applications

4.1 The Link Budget for the Path

In this chapter, we will work through an application of the model for two fixed antennas in relatively close proximity and examine what we can learn about the subsurface based on the constructive and destructive interference of two or more waves. Starting with the direct signal in air between two antennas with a line of sight and separated by a distance, b, we sketch the geometry of this scenario in Figure 12.

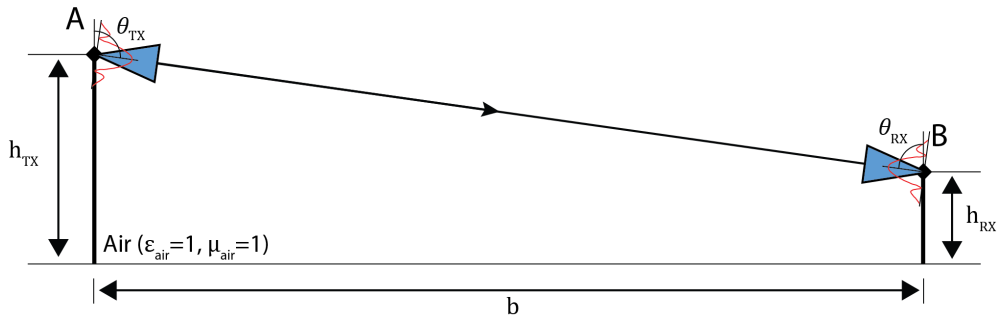

Figure 12. The direct signal between two standard gain horn antennas.

The transmitter is connected to Antenna A which is mounted on a mast of height, h_{TX}, and oriented such that the bore-sight of the antenna is focused at Antenna B. We define the angle between the bore-sight of Antenna A and the vertical plane of its mast as θ_{TX}. The receiver is connected to Antenna B which is mounted on a second mast with height, h_{RX}. This antenna is

pointed directly at Antenna A so that the bore-sight aligns with the ray path, this angle is defined from the vertical plane of the mast as θ_{RX}. We define a third angle,

$$\theta_D = \tan^{-1}\left(\frac{b}{h_{TX} - h_{RX}}\right), \tag{4.1.1}$$

to describe the incidence angle of the direct ray with respect to the vertical plane. Now, we can calculate the path loss (3.4.3) and including the gain of each antenna (3.8.1)

$$L_{path\,1} = -20 \cdot \log_{10}\left(\frac{4\pi \cdot f \cdot r_{A\to B}}{v_p}\right) + G_{Ant\,A}(\pi - \theta_{TX} - \theta_D) + G_{Ant\,B}(\theta_{RX} - \theta_D). \tag{4.1.2}$$

Recall that the phase velocity, $v_p = \text{c} = \frac{1}{\sqrt{\mu_0 \epsilon_0}} = 2.998 \times 10^8\ m/s$, f is the frequency of the transmission, and the path length,

$$r_{A\to B} = \frac{b}{\sin\theta_D}. \tag{4.1.3}$$

Doing some additional manipulations to find the E-Field at B we can show that 4.1.2 becomes,

$$E_B = E_{path\,1} = \sqrt{2 \cdot \eta_0 \cdot P_A \cdot 10^{\frac{L_{path\,1}}{10}}}, \tag{4.1.4}$$

where P_A is the transmitter power (in Watts) and η_0 is the intrinsic impedance of free space.

4.2 A Surface Reflection and the Resulting Interference Pattern

In this section, we make a small modification to the application described in 4.1 to add a surface reflection. Assuming we have the same basic geometry as in Figure 12, but now the antenna masts are sitting on a semi-infinite dielectric slab with some properties defined by its relative permittivity, ε_1, and relative permeability, μ_1. Now, let us change the angle of the antennas so that they track the specular reflection point on the surface. A sketch of this new geometry is shown in Figure 13.

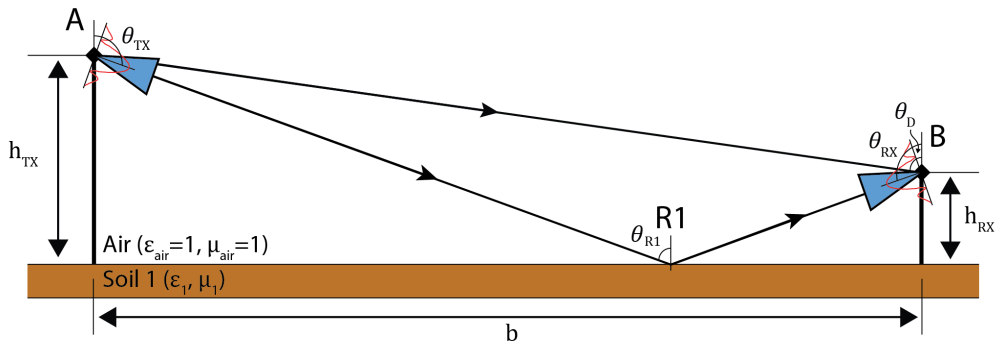

Figure 13. Geometry of a two-ray model with a reflection off the ground.

The total power received by Antenna B is now a combination of the direct path we calculated in 4.1.4 and the reflected ray. Defining a new incidence angle for this new ray path,

$$\theta_{R1} = \tan^{-1}\left(\frac{b}{h_{TX} + h_{RX}}\right), \tag{4.2.1}$$

we can now calculate the path loss of this second ray,

$$L_{Path\ 2} = -20 \cdot \log_{10}\left(\frac{4\pi \cdot f \cdot (r_{A\to R1} + r_{R1\to B})}{v_p}\right) + \cdots$$
$$G_{Ant\ A}(\pi - \theta_{TX} - \theta_{R1}) + G_{Ant\ B}(\theta_{RX} + \theta_{R1} - \pi). \quad (4.2.2)$$

To find the magnitude of this reflected path, we will also need to use the reflection coefficients calculated from 3.5.15 for the V-pol and 3.5.16 for the H-pol signal. Remember that a circular or elliptically polarized signal can always be split into its constituent V-pol and H-pol parts for this calculation. The calculation of $E_{path\ 2}$ follows the form of 3.5.20 where,

$$E_{Path\ 2} = R_{\text{air}\to\text{soil}\ 1} \cdot \sqrt{2 \cdot \eta_0 \cdot P_A \cdot 10^{\frac{L_{path\ 2}}{10}}} \quad (4.2.3)$$

Such that the magnitude of the reflected field is with:

$$r_{A\to R1} = \sqrt{(h_{TX})^2 + (h_{TX} \cdot \tan\theta_{R1})^2}, \quad (4.2.4)$$

$$r_{R1\to \text{B}} = \sqrt{(h_{RX})^2 + (h_{RX} \cdot \tan\theta_{R1})^2}. \quad (4.2.5)$$

Keeping track of the phase for each ray we know there is a phase shift of 180° due to the reflection,

$$\phi_{R1} = e^{i\pi}, \quad (4.2.6)$$

and another shift due to the difference in the path length between the direct ray and reflected ray,

$$\phi_{path\ 1} = e^{i\beta_1\,(r_{A\to \text{B}})}. \quad (4.2.7)$$

$$\phi_{path\ 2} = e^{i\beta_1\,(r_{A\to R1} + r_{R1\to \text{B}})}. \quad (4.2.8)$$

The resulting electric field due to the two ray paths will then have a total magnitude of,

$$E_B = E_{path\ 1} \cdot \phi_{path\ 1} + E_{path\ 2} \cdot \phi_{R1} \cdot \phi_{path\ 2}, \tag{4.2.9}$$

and a power of,

$$P_B = \frac{1}{2\eta_0}(E_B)^2. \tag{4.2.10}$$

4.3 Adding a Second Soil Layer

Using the methods described in Sections 4.1 and 4.2 we perform an analysis for a two-layer dielectric slab. For the second layer we will need to define a relative permittivity, ε_2, relative permeability, μ_2, and depth or thickness of the top layer, d_1. The addition of a second layer will result in a third ray path as shown in Figure 14.

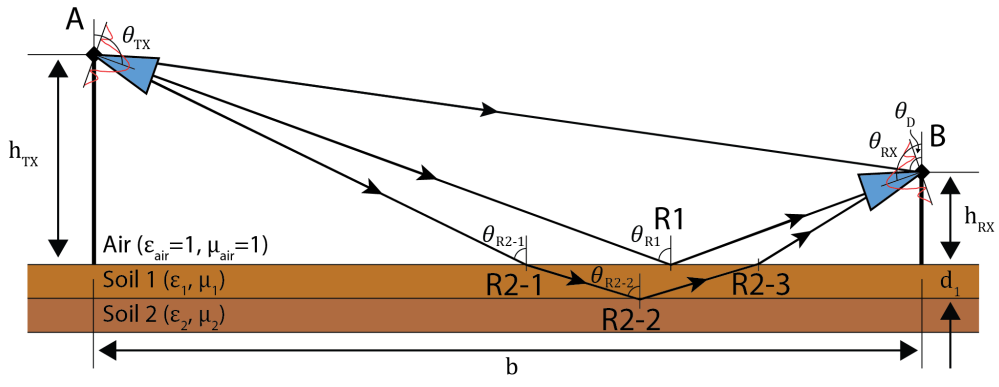

Figure 14. Geometry of a three-ray model with a second interface in the subsurface.

To calculate the location of the specular reflection point on of soil 2 we use the height of each antenna (h_{TX}, h_{RX}), the distance between the antenna masts (b), and the depth of the first soil layer (d_1). This gives us the location of point R2-2 which we can then use to find the angles θ_{R2-1} and θ_{R2-2}. Then we track the E-field magnitude as we traverse from A to R2-1, the transmission through and loss within Soil1 as the ray progresses to R2-2, the reflection off the interface with Soil 2 and loss traveling back up through Soil 1 to R2-3, and finally the transmission through the interface of Soil 1 back into the air as the ray travels back up to B. Now that we have the magnitude we need to keep track of the phase shifts due to the reflection at R2-2 and the difference in the path length of the third ray and once that is accounted for then we can compute the total E-field at B due to the three rays,

$$E_B = E_{path\ 1} \cdot \phi_{path\ 1} + E_{path\ 2} \cdot \phi_{R1} \cdot \phi_{path\ 2} + E_{path\ 3} \cdot \phi_{R2-2} \cdot \phi_{path\ 3}, \qquad (4.3.1)$$

So, now that we have the simple two-layer solution let's consider the potential for internal reflections within the soil layers. Plotting a fourth path from the air into Soil 1, the reflection off of Soil 2 back up towards the surface, a second reflection off of the interface of Soil 1 and the air down to Soil 2, a third reflection off of Soil 2 back up and out to the receiving antenna. This geometry is shown in Figure 15.

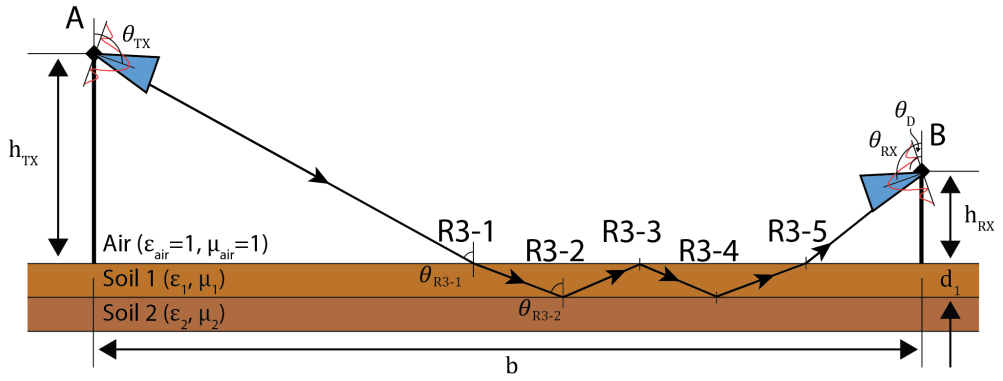

Figure 15. Example of an internal reflection within the soil layers.

In this example the ray bounces around inside the soil layer three times, but it's conceivable to imagine a scenario where another ray bounces five times, seven times or more. Computing the path lengths and angles for all these cases can be tedious, but we notice that the equations all take the same form and so we can do a Taylor Series to estimate the contribution of these internal reflections.

This is the theoretical basis for how our ray tracing model works. We can use the same methods to calculate the ray paths through an arbitrarily large number of different layering schemes so long as we know the relative permittivity, relative permeability, and thickness of each layer. We can use this model to look at the impacts of different geometries such as receiver height, incidence angle, polarization, and even consider the potential of a mobile platform such as an aircraft or spacecraft. We can explore the impacts and effects of different transmission power levels or making measurements at multiple frequencies and we can use it to conduct trade studies on antenna designs or even determine the sensitivity requirements of our receiver. In the

following sections, we will examine the different types of interference patterns that result from a bistatic radar which measures the received power of a signal as we change the incidence angle or frequency.

4.4 Measuring the Properties of a Soil Layer Through Use of the Reflectivity and Interference Pattern at Various Incidence Angles

In this section, we will use our basic two-layer model described in section 4.3 to examine the basic features of the interference pattern and how it changes as we change the dielectric content of the top layer or its thickness. These results were first reported by Elliott *et al.* (2014), but we will reproduce them here. Beginning with the assumption that Antenna A and Antenna B are two perfect isotropic radiators. Antenna A is located some semi-infinite distance away from the receiver such that we are neither concerned with its height nor its distance, but merely its incidence angle with respect to the surface. Antenna B is fixed at height of 1 m. We will use a frequency of 7.2 GHz which correspond to the uplink frequency of the Deep Space Network and Curiosity Rover's High Gain Antenna (Makovsky, *et al.* 2009). For the dielectric properties of each layer we will use 11 different soils with moisture contents from 0% to 10% water by mass (Hallikainen, *et al*. 1985) as an input for the top layer and a dry concrete or bedrock slab (Xu, *et al.* 2008) as the bottom layer. Finally, we will apply a filter to the signal to eliminate the direct path between the antennas and instead look solely at the interference pattern resulting from the reflections. For reference, an updated geometry sketch showing the first three rays is provided in Figure 16.

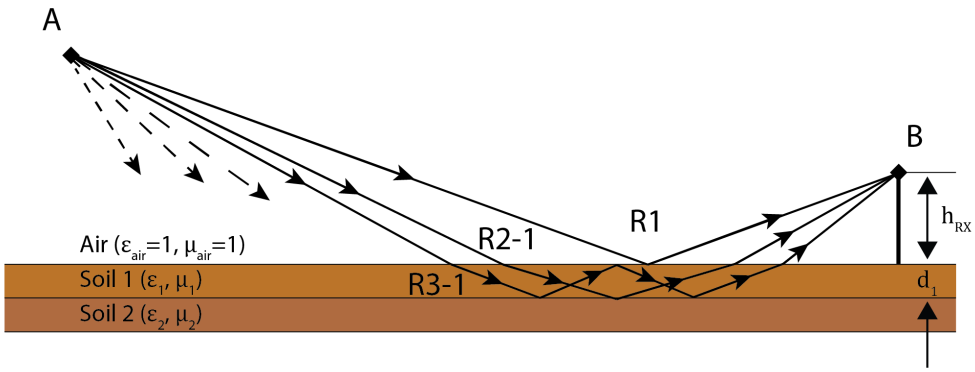

Figure 16. Model geometry used to generate the interference patterns seen throughout sections 4.4 and 4.5.

As a first check, we will use a one-layer soil model with an arbitrarily deep first layer ($d_1 = 10\ meters$) to reduce the potential influence of R2, R3, and other internal reflections. The solution should behave in a manner similar to Figure 5 with the Brewster angle changing in relation to the relative permittivity of the top layer. We chose the relative permittivities of $\varepsilon_1 = [2.34 - 0.01i, 2.54 - 0.05i, 2.76 - 0.11i, 3.00 - 0.17i, 3.25 - 0.25i, 3.52 - 0.33i, 3.81 - 0.42i, 4.12 - 0.52i, 4.45 - 0.62i, 4.79 - 0.73i, 5.15 - 0.85i]$ which correspond to a sandy soil with between 0% and 10% water in 1% increments. Figure 17 shows the model results for this soil model with incidence angle (θ_{R1}) spanning the range from 0 to 90 degrees, a frequency (f) of 7.2 GHz, and an antenna height (h_{TX}) of 1.0 meter.

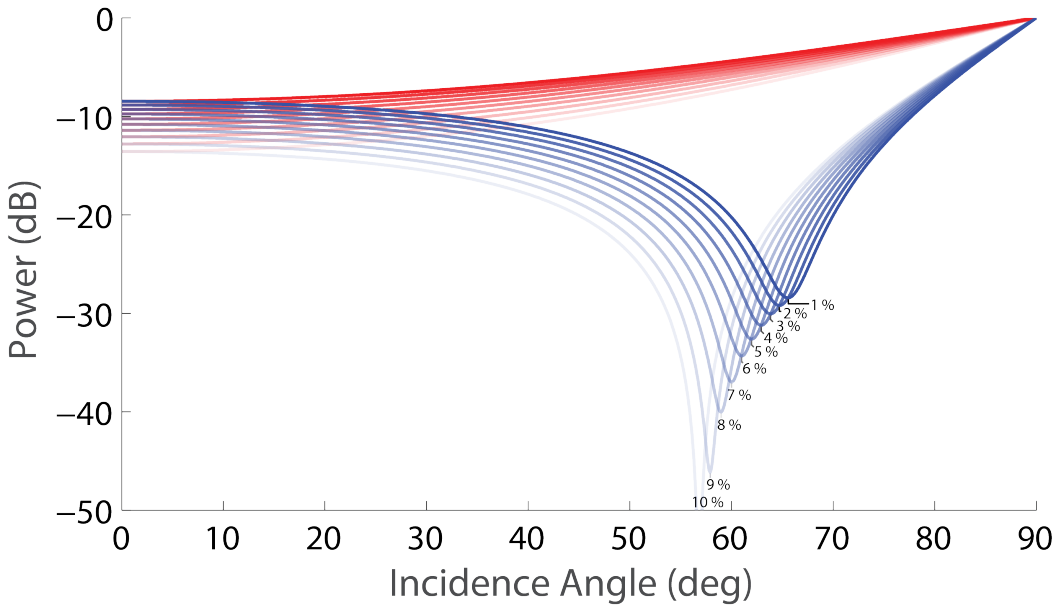

Figure 17. Reflected power V-pol (blue) and H-pol (red) as a function of incidence angle from a one-layer soil model.

In Figure 17, we see two types of solutions: in blue we have the received power in the vertical polarization and in red we see the horizontal polarization. Here we also use a shading profile which fades from dry sand ($\varepsilon_1 = 2.34 - 0.01i$, 0% water, lightest color) to wet sand ($\varepsilon_1 = 5.15 - 0.85i$, 10% water, darkest color) to aid in our interpretation. For both polarizations an increase in the water content of the top layer leads to a stronger reflection of the incoming radiation and a higher received power. We can also note that at incidence angles of 0 degrees and 90 degrees the strength of the reflected signal from both polarizations is equivalent but that they diverge between those two extremes due to the impact of the Brewster angle in the vertical polarization. The Brewster angle causes a single null or minimum in the vertical polarization which shifts to higher incidence angles as the relative permittivity increases. In a case like this

where we effectively have one soil layer which is visible to the receiver, the depth and location of that null can be used to retrieve the relative permittivity of that soil layer.

Now, let's look at a two-layer model with a fixed relative permittivity of $\varepsilon_1 = 2.34 - 0.01i$ (dry sand, 0% water) for the top layer and $\varepsilon_2 = 4.95 - 0.69i$ (concrete) for the bottom. When we have two layers of soil reflecting the incoming wave it is now possible to have interference nulls in addition to Brewster angle. In this batch of model runs we will change the thickness of the top layer (dry sand) to understand how the location and magnitude of an interference null changes as a function of depth. The depths of the top layer selected here were chosen arbitrarily to show a progression from thin (5 cm) to thick (250 cm). Also, we will continue to use the color convention where blue represents the received power in the vertical polarization and red represents the horizontal polarization.

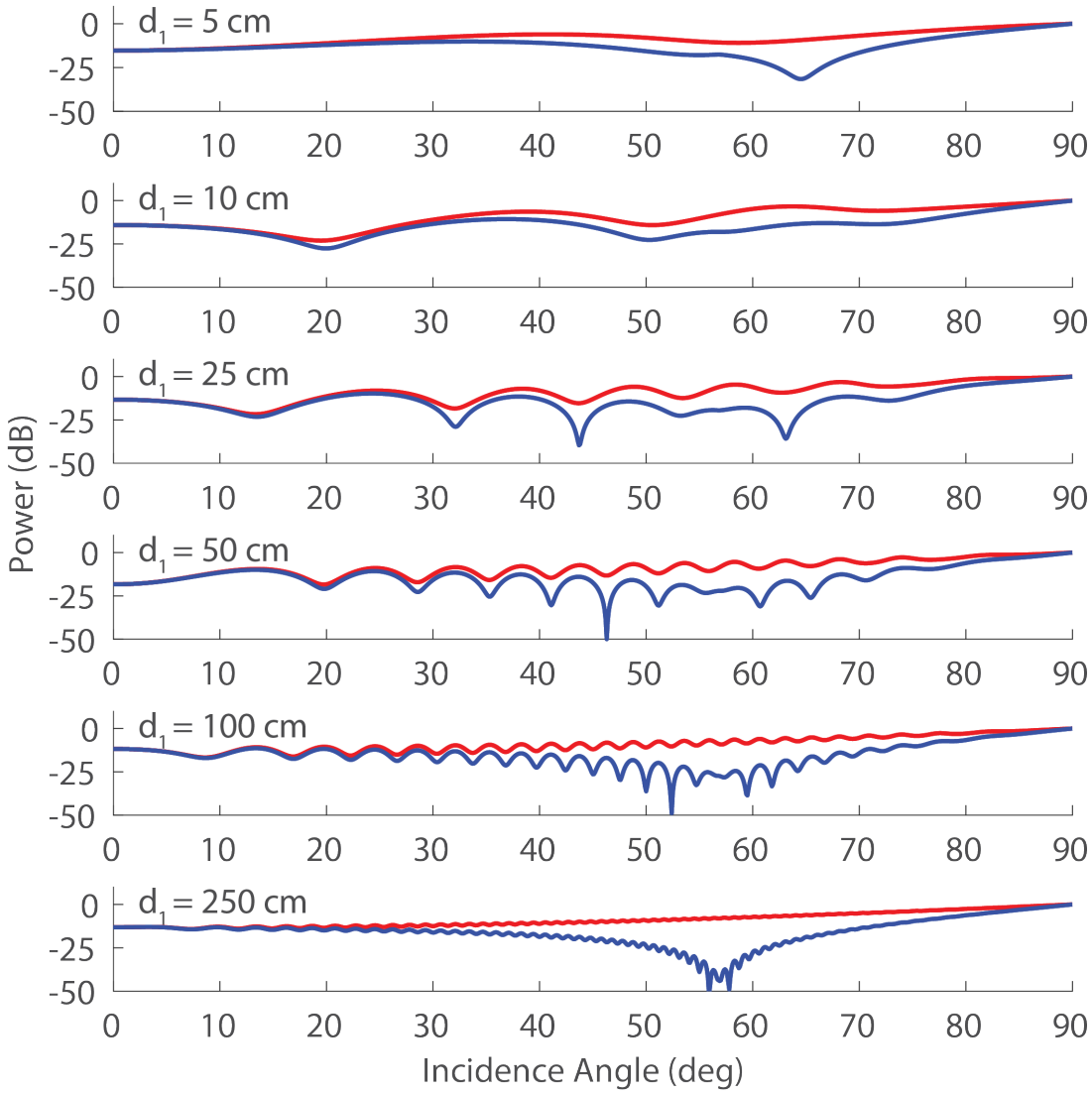

Figure 18. Reflected power V-pol (blue) and H-pol (red) as a function of incidence angle from two-layer soil model with various depths of dry sand on top of concrete.

In Figure 18 we begin to see the effects of multipath interference in the form of additional minima in both polarizations. These nulls or "fading" in the signal's received power are a result of the additive and destructive properties of combining two or more EM waves propagating along separate paths to the same receiver, i.e. multipath interference. Because this type of

interference is highly dependent on the path of EM waves, changing either the incidence angle or the thickness (i.e. depth of the second dielectric layer) can dramatically change the received power. Here we see that the greater the depth of the second layer the more minima or nulls will be present in the received signal. Also, we can observe that as the number of nulls increases the mean magnitude or depth of the nulls will diminish implying that at greater depths the interference pattern will disappear, and the reflected power once again resembles the semi-infinite single layer case in Figure 17.

In Figure 19, on the left we have re-drawn the top and bottom panel shown above with the two-layer interference pattern for dry sand ($\varepsilon_1 = 2.34 - 0.01i$) on top of concrete ($\varepsilon_2 = 4.95 - 0.69i$) where the thickness of the dry sand layer is 5 cm and 250 cm respectively. On the right of Figure 19 we have the one-layer reflection profile for the concrete ($\varepsilon_1 = 4.95 - 0.69i$) and dry sand ($\varepsilon_1 = 2.34 - 0.01i$). Here we can see that for a thin layer of sand ($d_1 = 5\ cm$, top left) on top of concrete the reflected signal remains similar to that of a single layer the concrete (top right). Similarly, for a thick layer of sand ($d_1 = 250\ cm$, bottom left) the reflected signal closely resembles that of a single layer of sand (bottom right) and the effect of the concrete layer is diminished. This result matches our intuition of the underlying process where the interference pattern is simply the combination of the reflection profile of two separate layers. It may seem complex, but the underlying signals can still be teased out.

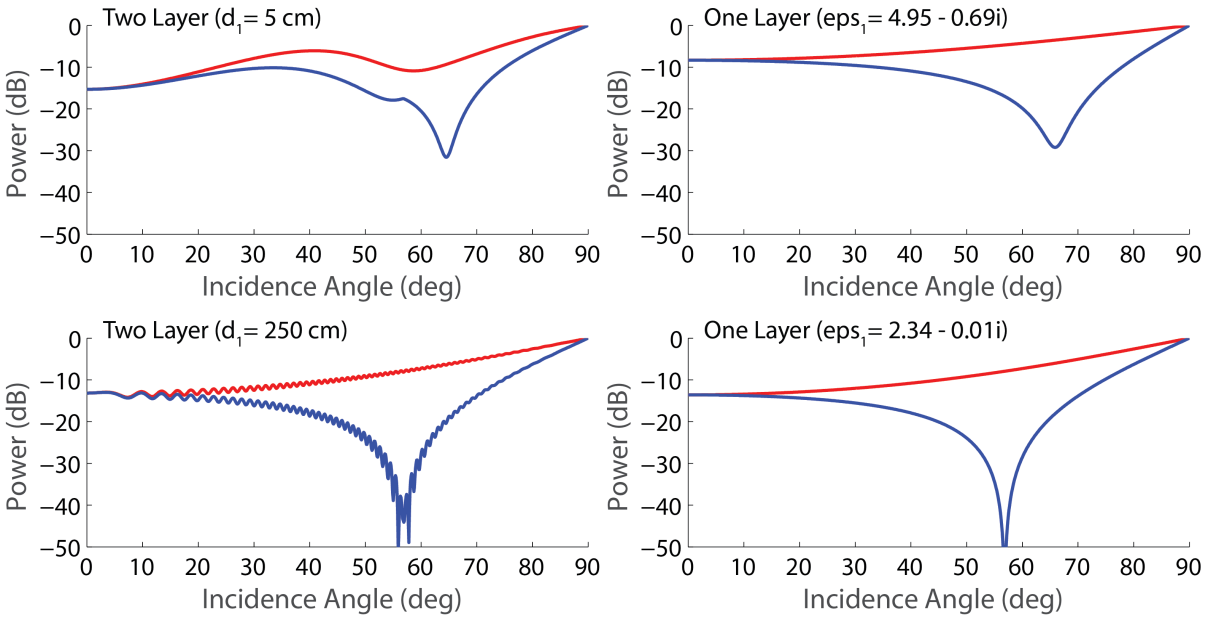

Figure 19. Comparing the two-layer interference pattern to the one-layer reflection profile of dry soil (eps = 2.34 – 0.01i) and concrete (eps = 4.95 – 0.69i).

The final observation we should make from Figures Figure 18 and Figure 19 is that the location of these nulls is highly correlated between the vertical and horizontal polarization. With the exception of the null at Brewster angle; any time we observe the presence of a null in vertical polarization we see a corresponding null in the horizontal polarization and vice versa. This implies that any trends observed in the interference pattern will apply to both linear signal polarizations as well as the circular polarizations. In Figure 20, we have the same model outputs as above, but for a right-hand circularly polarized (RHCP) signal. Since this polarization is simply a combination of the two linear polarizations shown earlier we see a very similar output with the nulls in the same position as in Figure 18. Indeed, the RHCP signal in Figure 20 could be described as resembling that of the H-pol in Figure 18, but with the addition of a notch or ramp at higher incidence angles due to the Brewster angle.

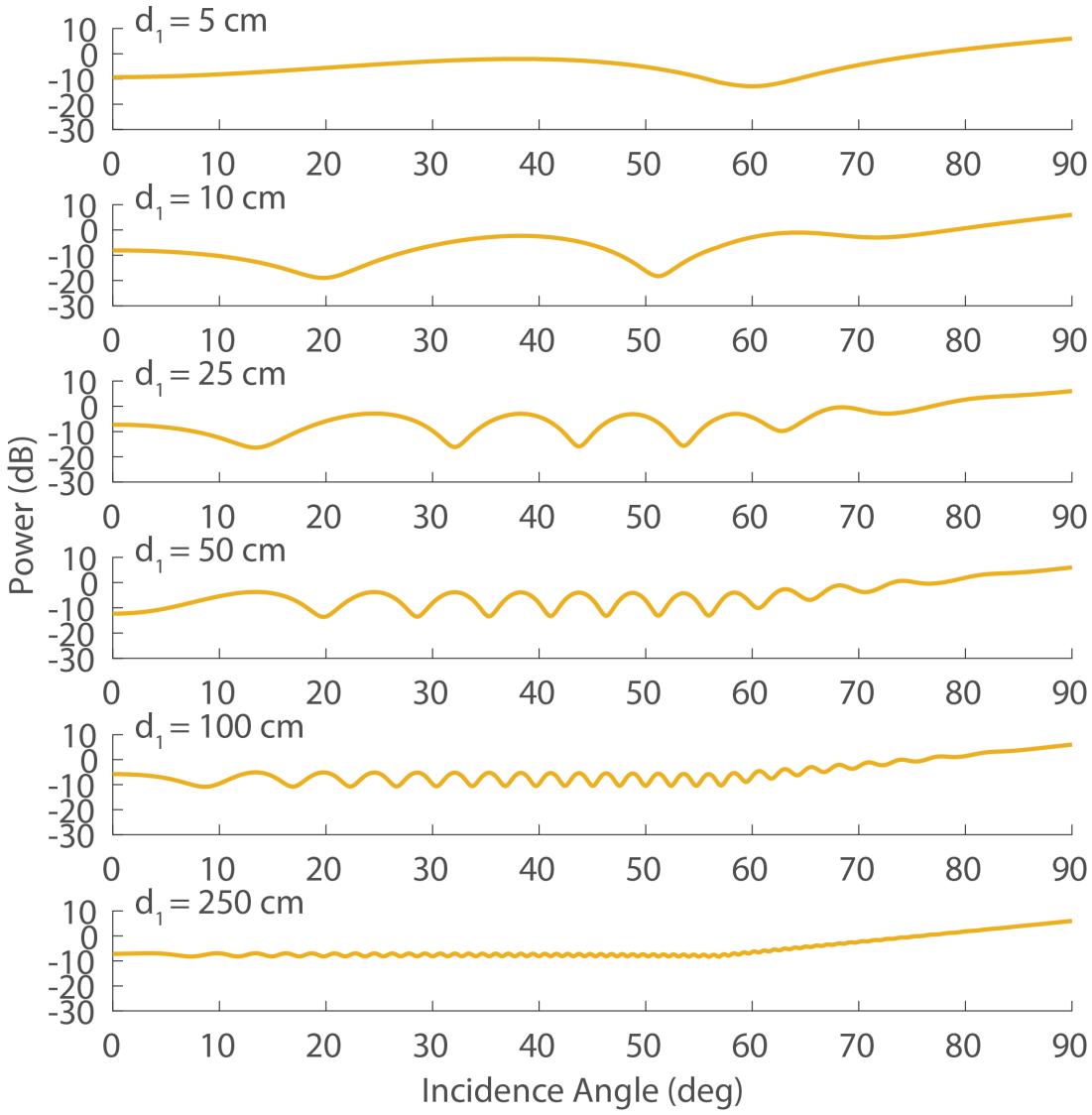

Figure 20. Reflected power RHCP (yellow) as a function of incidence angle from two-layer soil model with various depths of dry sand on top of concrete.

Switching back to the two linear polarizations and looking more closely at the behavior of the interference pattern as we reduce the incremental step size in depth we can make some additional observations. In Figure 21, we start at a depth of 9 cm (lightest color) and step up to a depth of 10 cm (darkest color) in 1 mm increments. At this resolution we can track the

progression of each null as a function of the layer depth and see that any individual null will shift to left (lower incidence angle) and get slightly closer to its neighbors as the depth increases. One exception to this rule is in the V-pol (blue) where we notice the presence of a fixed inflection point through which all the interference pattterns travel. This is due to the Brewster angle and if it can be identified, it can be used to find the dielectric constant of the top layer.

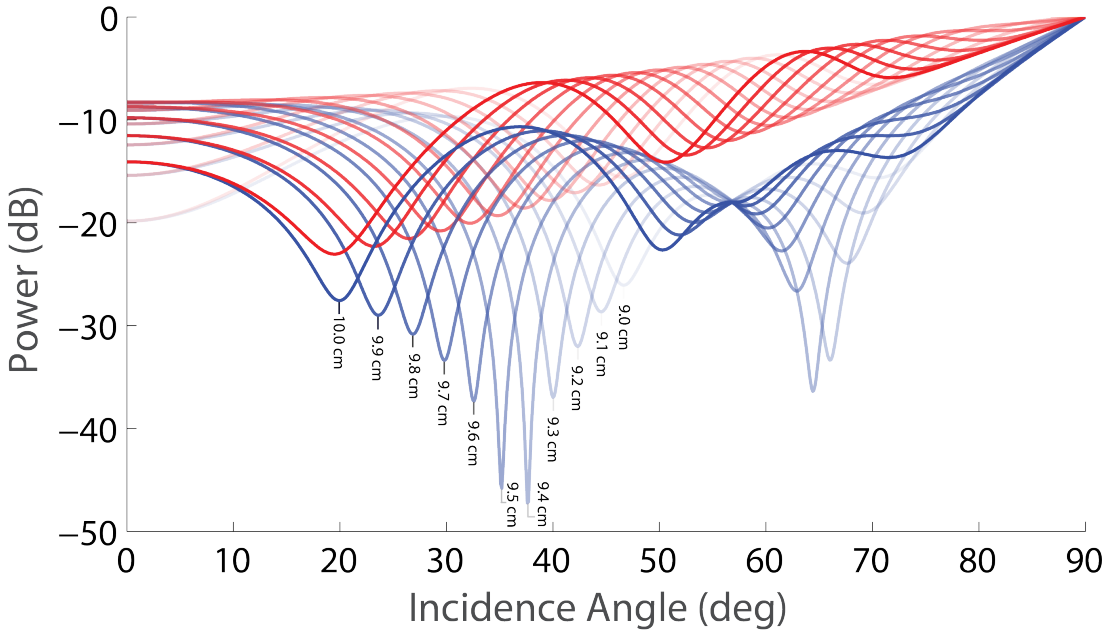

Figure 21. Procession of the interference pattern as a function of incidence angle in 1 mm depth increments from 9 cm to 10 cm, V-pol (blue) and H-pol (red), for a two-layer soil model of dry sand on top of concrete.

If we take this a step further and plot the interference pattern with a 0.1 mm step in depth we can very clearly see the inflection point in the V-pol signal and these figures begin to look like an inverted plot of the reflection coefficients. Three plots are included in Figure 22 for three different dielectric constants with a 0.1 mm step in depth. For $\varepsilon_1 = 2.34 - 0.01i$ (top) the inflection point is at $\theta_i = 56.8°$, $\varepsilon_1 = 2.76 - 0.10i$ (middle) the inflection point is at $\theta_i =$

59.1°, and $\varepsilon_1 = 3.25 - 0.25i$ (bottom) the inflection point is at $\theta_i = 61.0°$. This corresponds to the Brewster angle (3.5.17) and can therefore be used to determine ε_1 for the top layer.

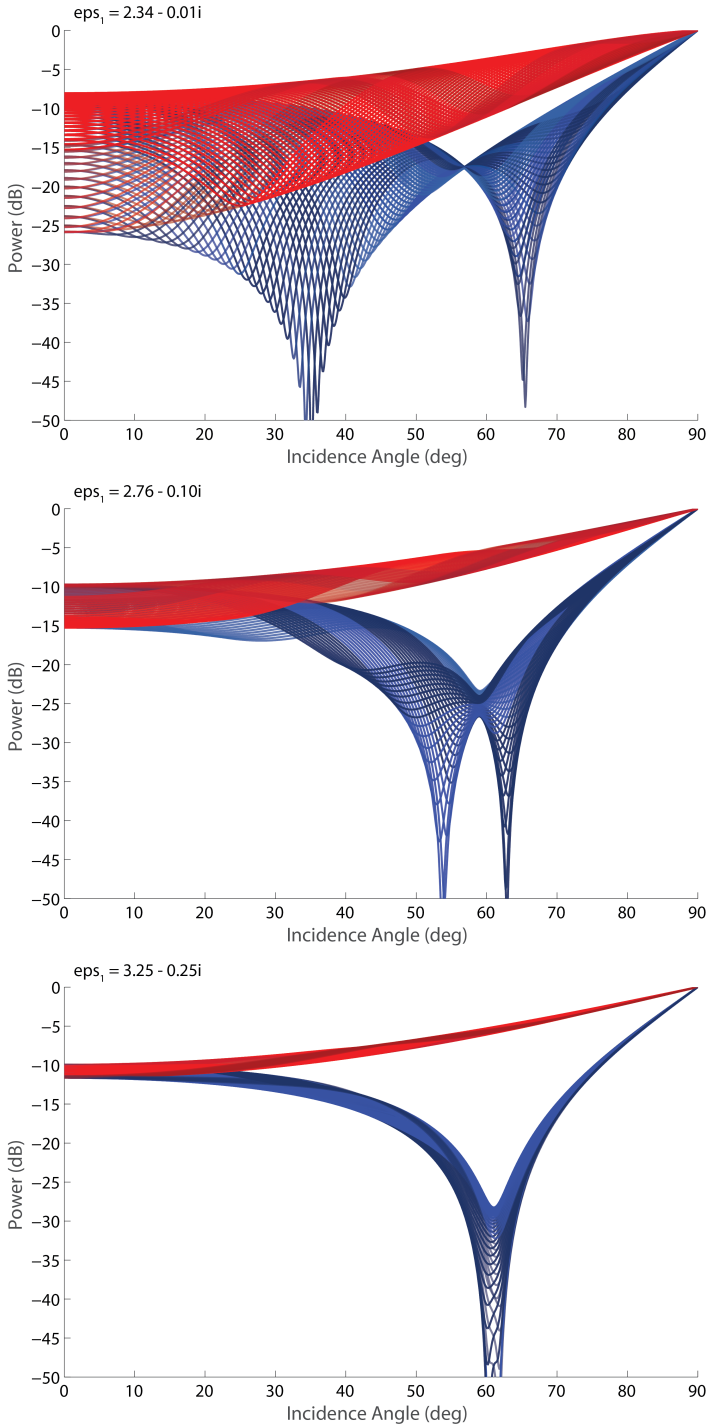

Figure 22. Procession of the interference pattern in 0.1 mm depth increments for $\varepsilon_1 = 2.34 - 0.01i$ *(top),* $\varepsilon_1 = 2.76 - 0.10i$ *(middle), and* $\varepsilon_1 = 3.25 - 0.25i$ *(bottom).*

To perform an inversion on one of these interference patterns and solve for the relative permittivities of each layer and their depths we propose an iterative approach starting with an estimate of the V-pol inflection point or RHCP ramp. Finding this value gives us the Brewster angle and a first guess for the relative permittivity for the top layer of soil (ε_1). Using the model inputs of $\varepsilon_1 = 2.34 - 0.01i$, $\varepsilon_2 = 4.95 - 0.69i$, and $d_1 = 10.5\ cm$ we can see in Figure 23 that there is an inflection point at $\theta_i \cong 56.9°$ and two nulls with a spacing of $\Delta\theta_i \cong 23.5°$.

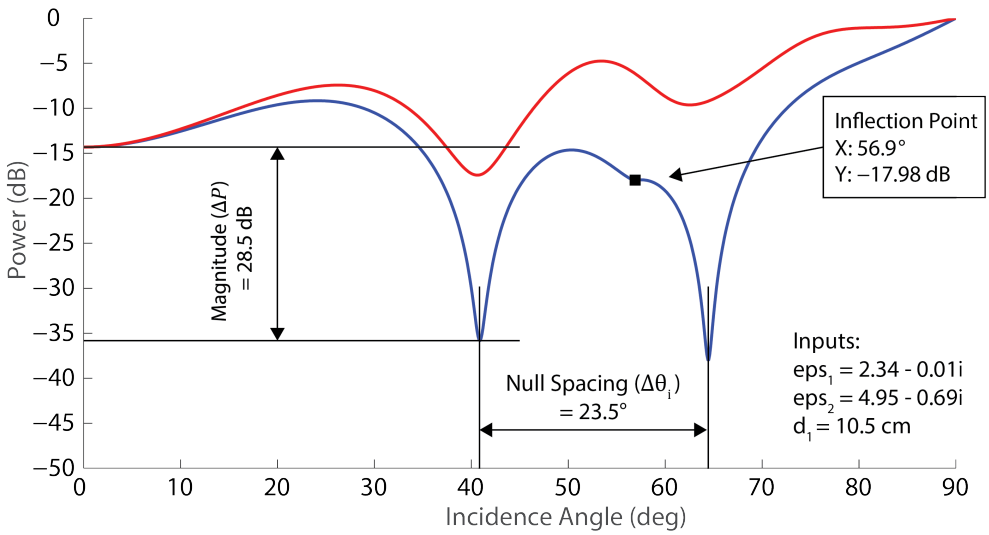

Figure 23. An interference pattern from a two-layer model showing the null spacing ($\Delta\theta_i$), magnitude (ΔP), and inflection point.

Figure 24 shows the relationship between the Brewster angle (θ_b) and the relative permittivity of the top layer (ε_1). Using the inflection point of 56.9° as the Brewster angle (θ_b) we can find $\epsilon_1 \cong (\tan\theta_b)^2 = 2.35$ from Equation 3.5.17. If you only have the H-pol data available or if you do not have enough angular data to capture the Brewster angle then you must either use a priori data or make a best guess of the relative permittivity of the top layer in order to do an inversion.

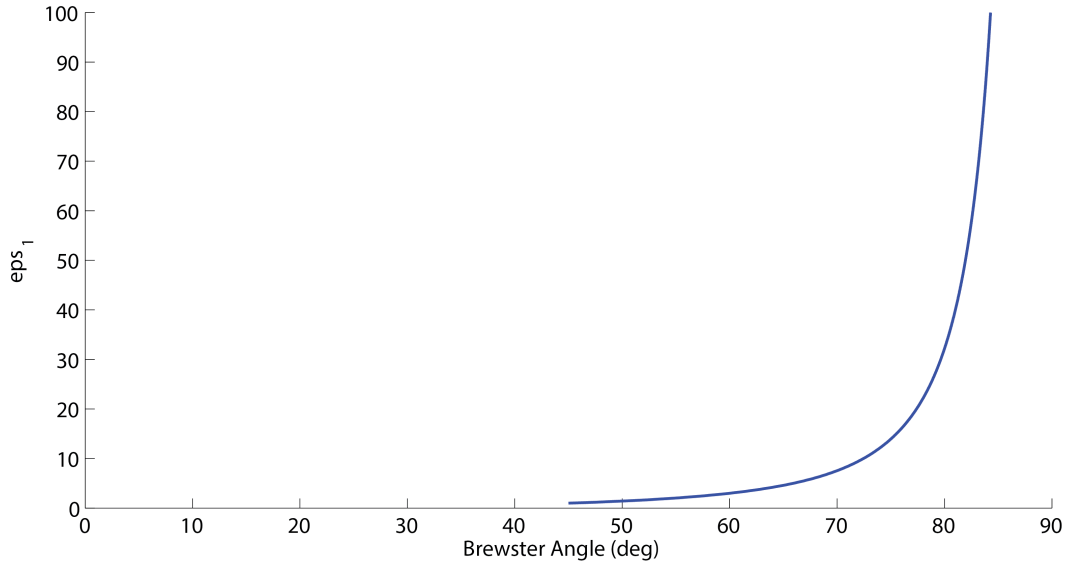

Figure 24. The Brewster angle for an interface between air and the top layer of soil.

The next step is to count the number of nulls or measure the null spacing ($\Delta\theta_i$). Given this spacing and a reasonable value of ε_1 we can use our model results to constrain the solution to some range of depths. Figure 25 and Figure 26 show how the number of nulls correlates to the depth for different initial values of $\varepsilon_1$and ε_2. Using the bottom plot in Figure 25 for $\varepsilon_1 = 2.5$, we can see that the median depth for two nulls is 13.0 cm with a maximum of 23.0 cm and minimum of 7.0 cm.

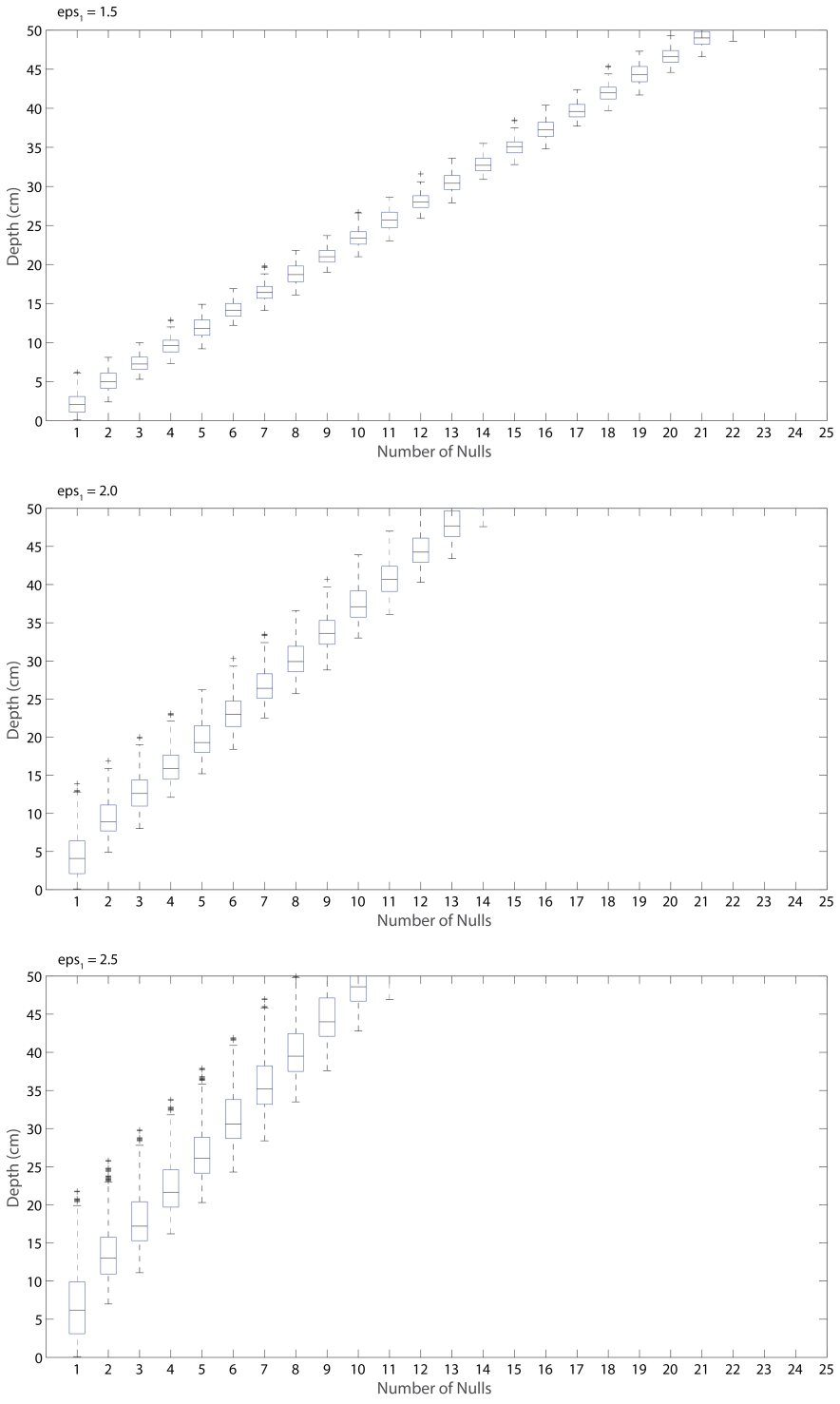

Figure 25. Relationship between the depth of the first layer (d_1) and the number of nulls for $\varepsilon_1 = 1.5$ (top), for $\varepsilon_1 = 2.0$ (middle) and for $\varepsilon_1 = 2.5$ (bottom).

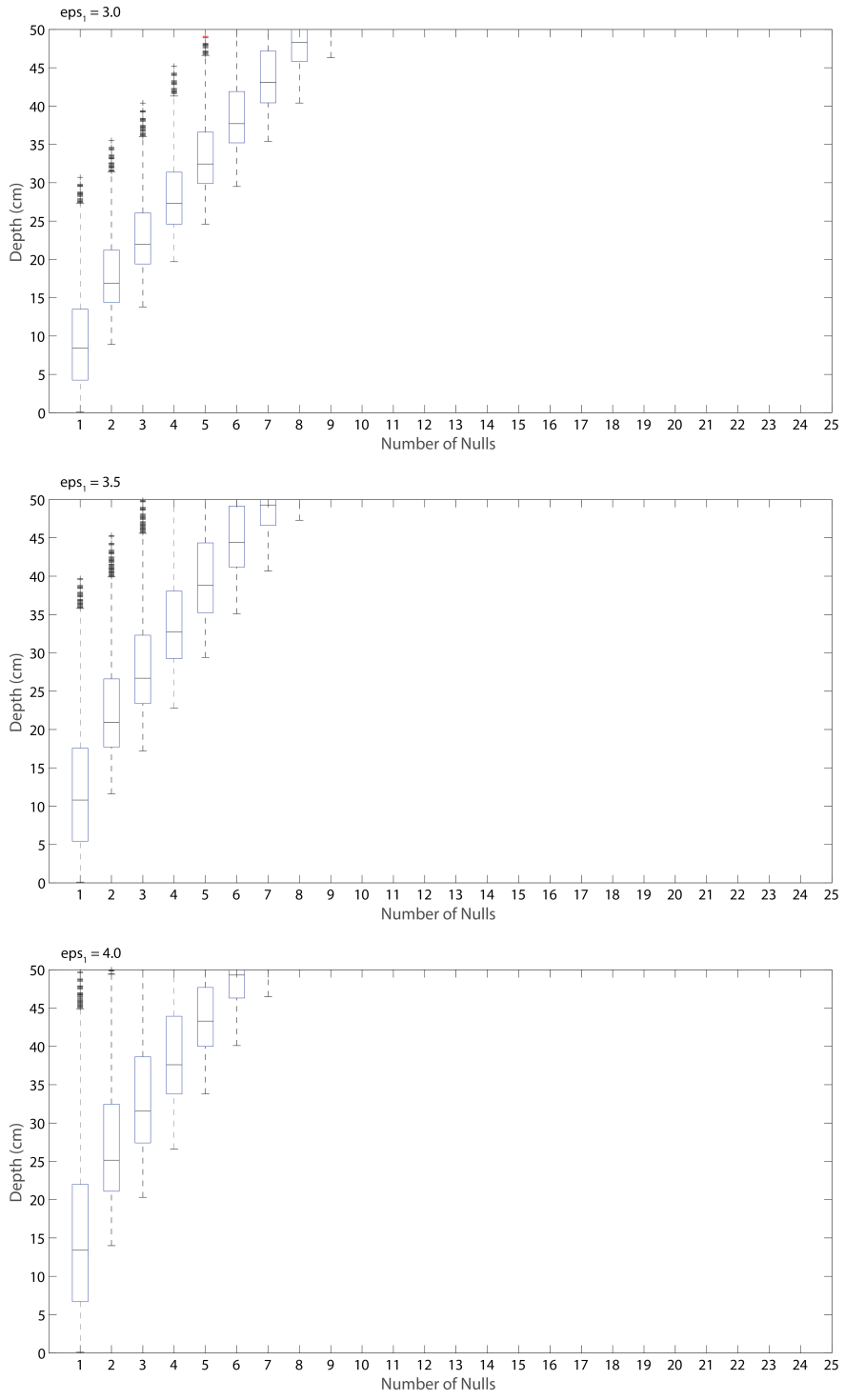

Figure 26. Relationship between the depth of the first layer (d_1) and the number of nulls for $\varepsilon_1 = 3.0$ (top), for $\varepsilon_1 = 3.5$ (middle) and for $\varepsilon_1 = 4.0$ (bottom).

We can also perform an inversion using a smaller subset of incidence angles or simply the null spacing ($\Delta\theta_i$) between two nulls. This process is a little more involved and tends to overestimate the range of potential depths than say counting the number of nulls because the spacing between nulls is wider at incidence angles near 0° then it is near 90°. This leads to a wider range of potential depths for a given null spacing. However, while it may not constrain the depth as much as counting the number of nulls did, this method offers a significant advantage in that we no longer need to make observations over the entire range of incidence angles. This simplification makes measuring the null spacing the preferred method of inversion in many cases. Figures Figure 27 and Figure 28 show the range of depths which may correspond to the null spacing ($\Delta\theta_i$) in degrees. Each of these figures is drawn using a different value for the relative permittivity of the top layer (ε_1) from 1.5 to 4.0. The shaded region represents a conservative range of potential depth values and the solid line represents an exponential curve fit to the median depth. Using a null spacing of $\Delta\theta_i \cong 23.5°$ from Figure 23 and the lowest plot from Figure 27 ($\varepsilon_1 = 2.5$) we can conclude that the median depth is 10.2 cm with a maximum of 34.0 cm and minimum of 7.0 cm.

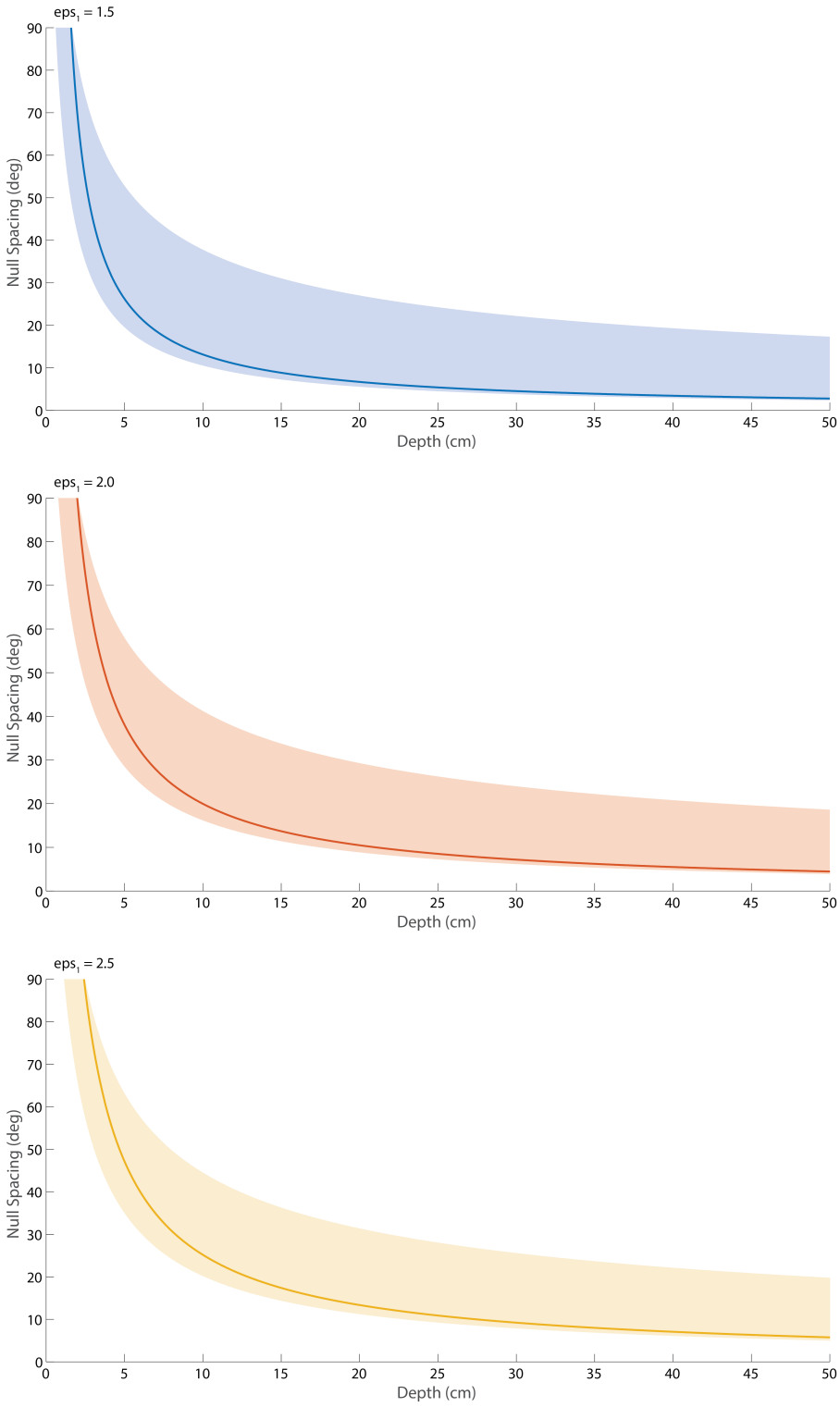

Figure 27. Relationship between the depth of the first layer (d_1) and the null spacing ($\Delta\theta_i$) for $\varepsilon_1 = 1.5$ (top), for $\varepsilon_1 = 2.0$ (middle) and for $\varepsilon_1 = 2.5$ (bottom).

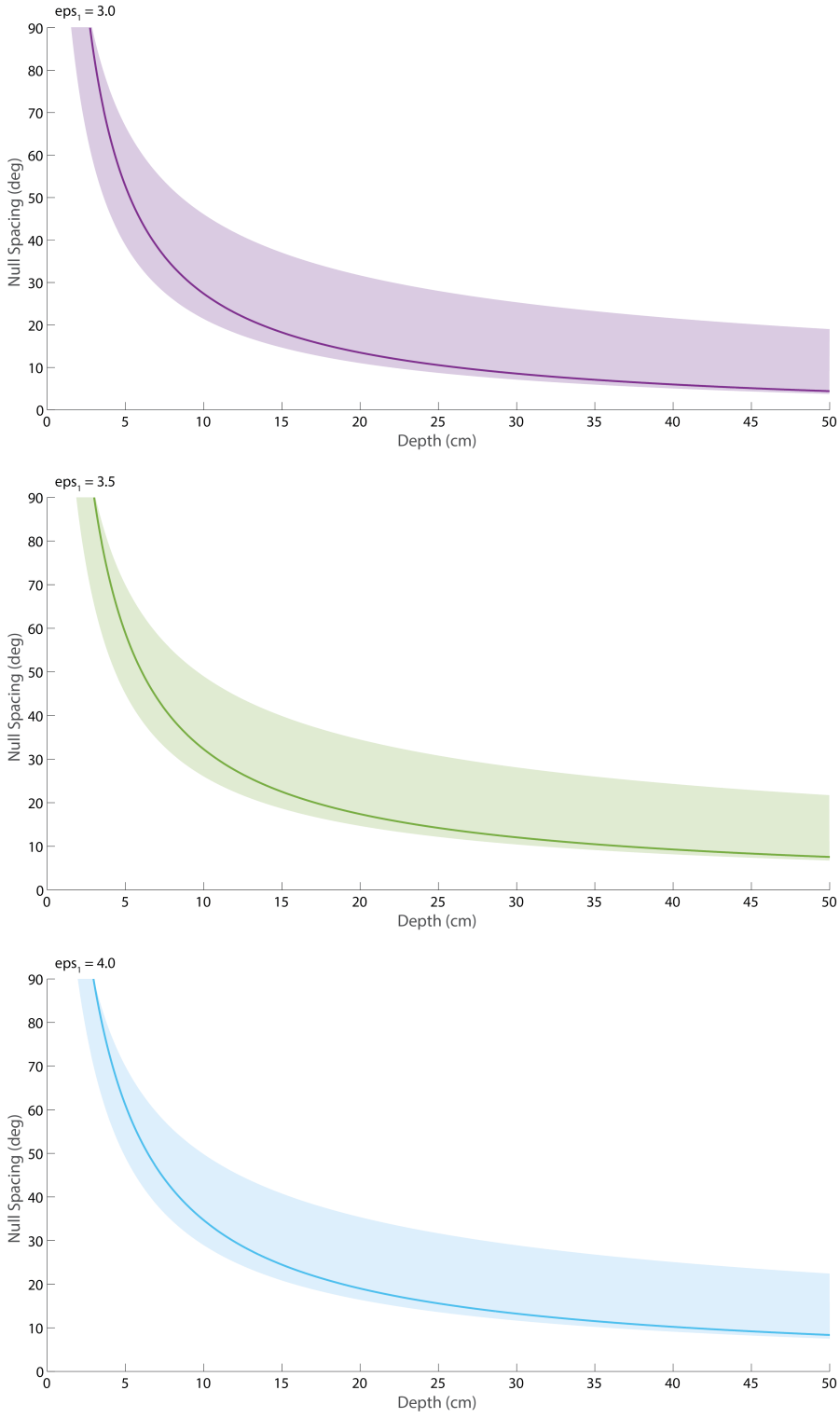

Figure 28. Relationship between the depth of the first layer (d_1) and the null spacing ($\Delta\theta_i$) for $\varepsilon_1 = 3.0$ (top), for $\varepsilon_1 = 3.5$ (middle) and for $\varepsilon_1 = 4.0$ (bottom).

The third step in this process is to measure the magnitude of the null (ΔP). The magnitude is a function of both the depth of the top layer and the ratio of the relative permittivities ($\varepsilon_2/\varepsilon_1$). If we get a good estimate of the top layer's relative permittivity (ε_1) and the depth (d_1), we can adjust the amplitude of the nulls using ε_2. Once we have a first estimate for each of the three parameters we recommend iterating on this solution using a similar range of depths and relative permittivities in the model and minimizing the root mean squared error between the model output and the measurement data. This methodology has worked well in the inversion of our laboratory data.

4.5 Measuring the Properties of a Soil Layer Through Use of the Reflectivity and Interference Pattern at Various Frequencies

Now we ask the question, what if instead of changing the incidence angle we changed the frequency of the source signal. Repeating the process described in section 4.4 we change the model inputs to fix the angle (θ_{R1}) at 0° and vary the frequency (f) from 7 to 11 GHz. This corresponds to the bandwidth of the Pasternack PE9857 standard gain horn available in our lab. As we are using a fixed incidence angle, we no longer need to consider the polarization of the signal. The reflected power in the vertical, horizontal, and circular polarizations is equivalent and so a single line will be used for all three polarizations throughout this chapter. As we did in Figure 17, we will begin by considering a semi-infinite one-layer model with different relative permittivities calculated by changing the water content of a sand in the Hallikainen soil moisture model (Hallikainen, et al. 1985). In Figure 29 we use a shading profile which darkens from dry sand ($\varepsilon_1 = 2.34 - 0.01i$, 0% water, lightest color) to wet sand ($\varepsilon_1 = 5.15 - 0.85i$, 10% water, darkest color) to aid in our interpretation. For a one-layer model like this we don't see any

variation in frequency, but we do observe that an increase in the water content of the soil leads to a stronger reflection of the incoming radiation and a higher received power.

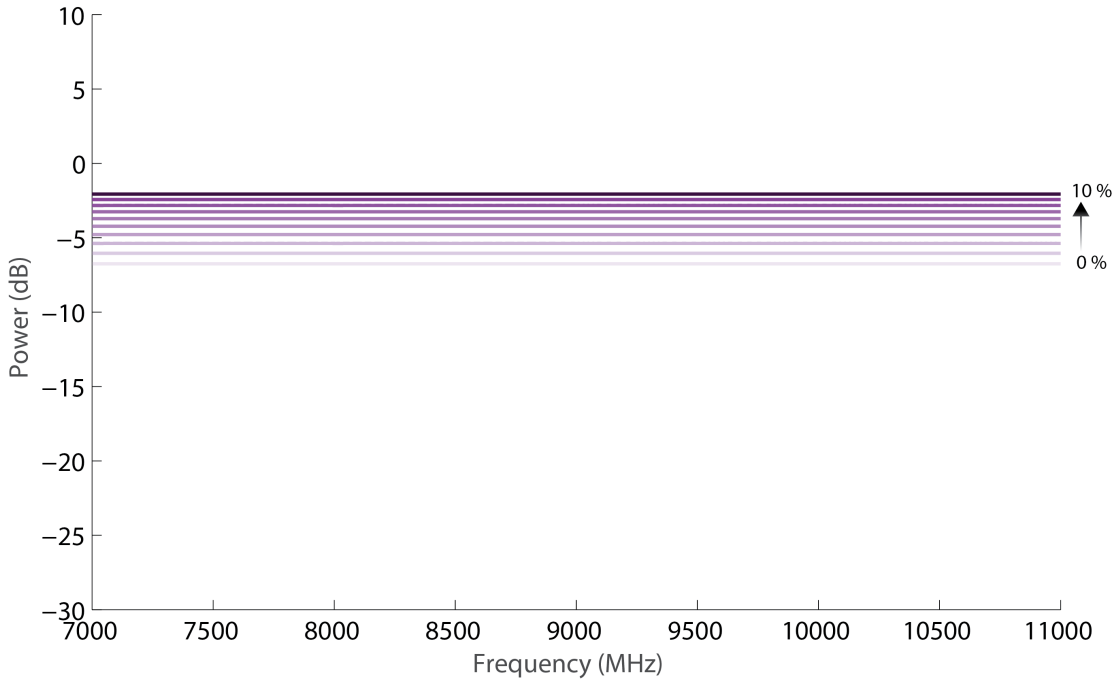

Figure 29. Reflected power as a function of frequency for a one-layer soil model.

Now, consider a similar experiment but with a two-layer model where a 5 cm layer of sand is covering concrete ($\varepsilon_2 = 4.95 - 0.69i$). In this case we use a shading profile which fades from $\varepsilon_1 = 2.34 - 0.01i$ (0% water, lightest color) to $\varepsilon_1 = 3.00 - 0.18i$ (3% water, darkest color) in 0.25% water increments. The resulting interference pattern is shown in Figure 30. Here we see an interference pattern as a function of frequency. The resulting interference pattern has a sinusoidal quality where the amplitude of the peaks and troughs is driven by the water content of the top layer. As the dielectric constant of the top layer increases, the depth of the nulls is reduced.

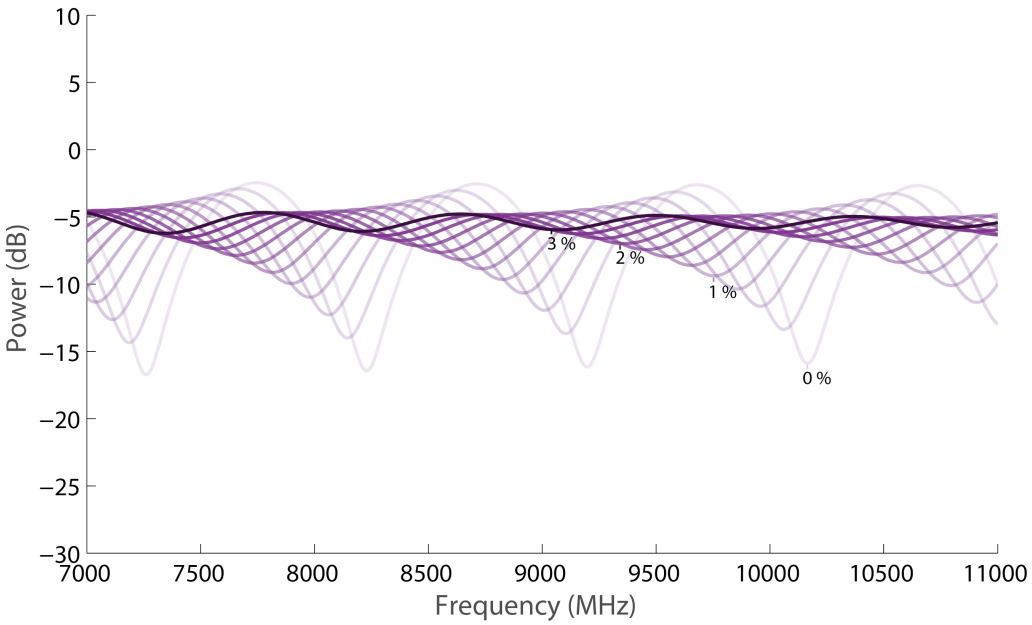

Figure 30. Interference pattern from a two-layer soil model where the thickness of the top layer is fixed at 5 cm, but the relative permittivity is allowed to change.

Making a few changes to the inputs once more we can examine the effects of changes in the layer thickness. Holding the relative permittivity of the top layer fixed at $\varepsilon_1 = 2.34 - 0.01i$, we now change the depth of the interface with the second layer (d_1) = 0.05, 0.10, 0.25, 0.50, 1.00, and 2.50 meters. These depths were selected to show a broad range similar to what was done for Figure 18 when we were looking at the interference pattern as a function of the incidence angle. Now in Figure 31 we see that as the thickness of the top layer increases so does the number of nulls. This behavior is very similar to what we observed when changing the incidence angle. Recalling Section 4.4 we note that the inversion of the interference patterns was complicated in some ways by the presence of the Brewster angle. Making observations in the frequency regime at a fixed angle simplifies the analysis and make autonomous classification and analysis of the results simpler. This is a fact we will exploit for our analysis in Section 5.5.

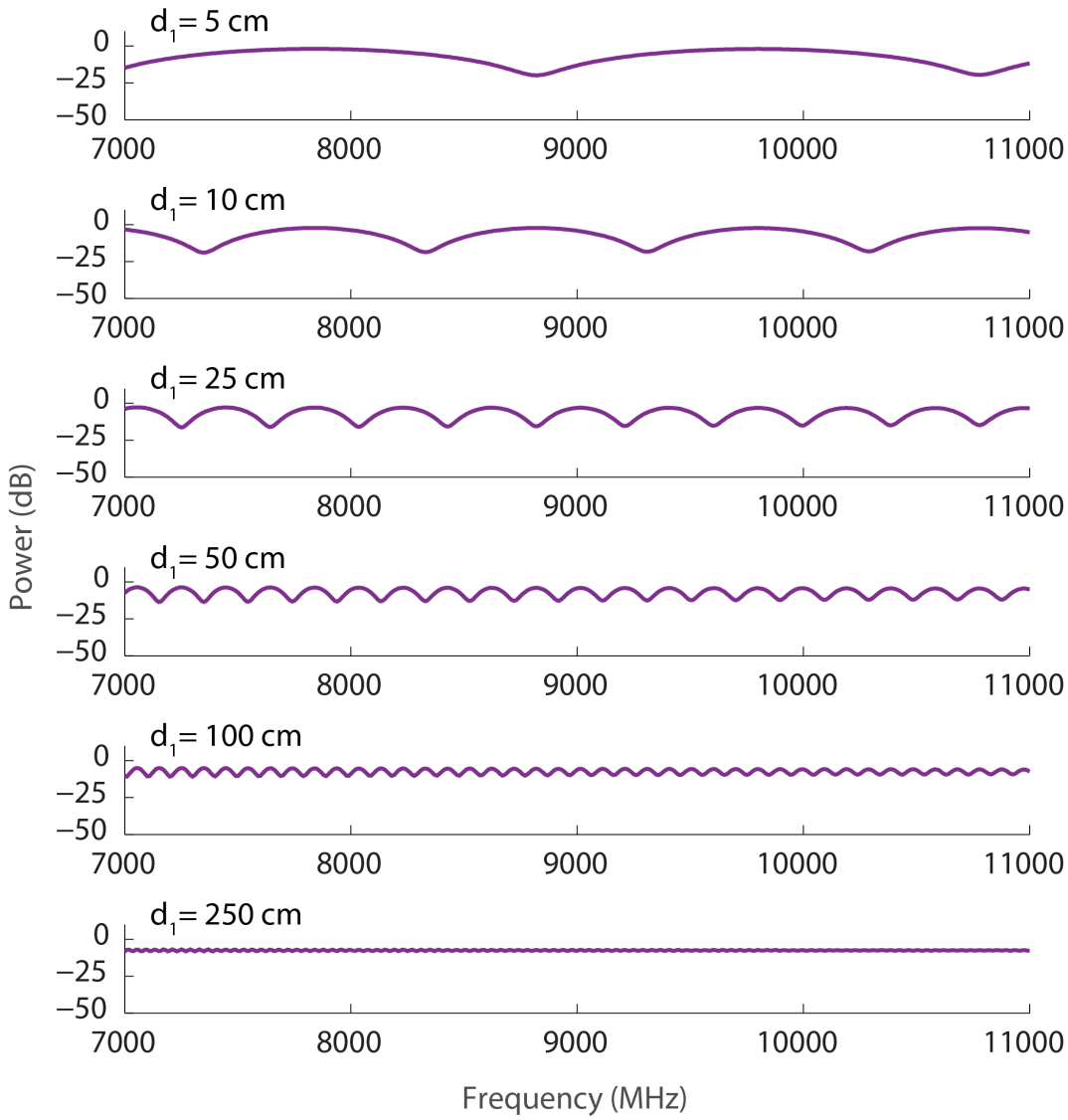

Figure 31. Interference pattern as a function of frequency from a two-layer soil profile with dry soil on top of concrete.

In Figure 32, we take a closer look and reduce the step size in layer depth to 1 mm, from 9.0 cm to 10.0 cm. This time we see that as the depth increases the nulls shift to the left (lower frequencies) and the null spacing (Δf) is reduced.

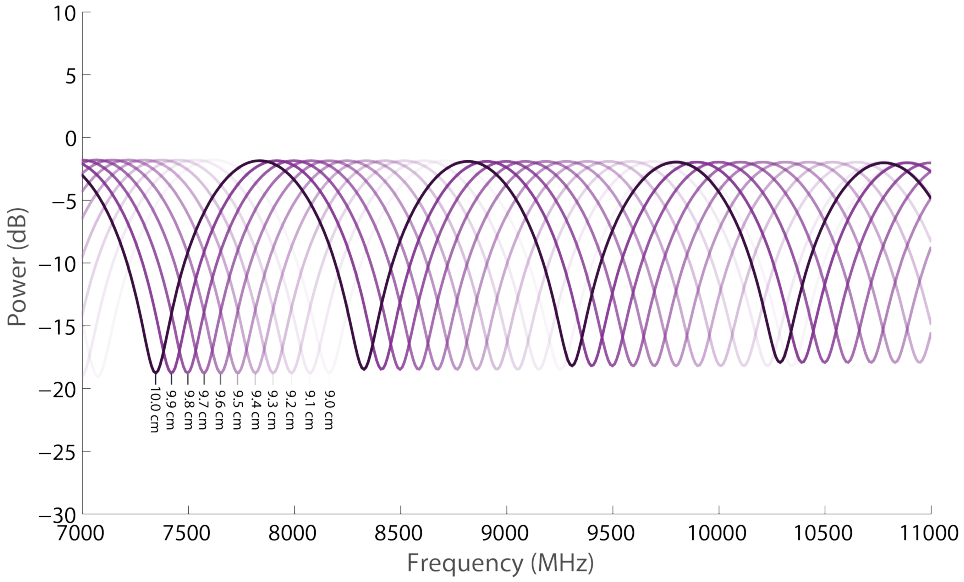

Figure 32. Procession of the interference pattern in 1 mm depth increments from $d_1 = 9$ cm to 10 cm.

To perform an inversion of this data, we can once again use the null spacing (Δf) and the magnitude (ΔP). Figure 33 shows both values for a two-layer model with 10.0 cm of sand.

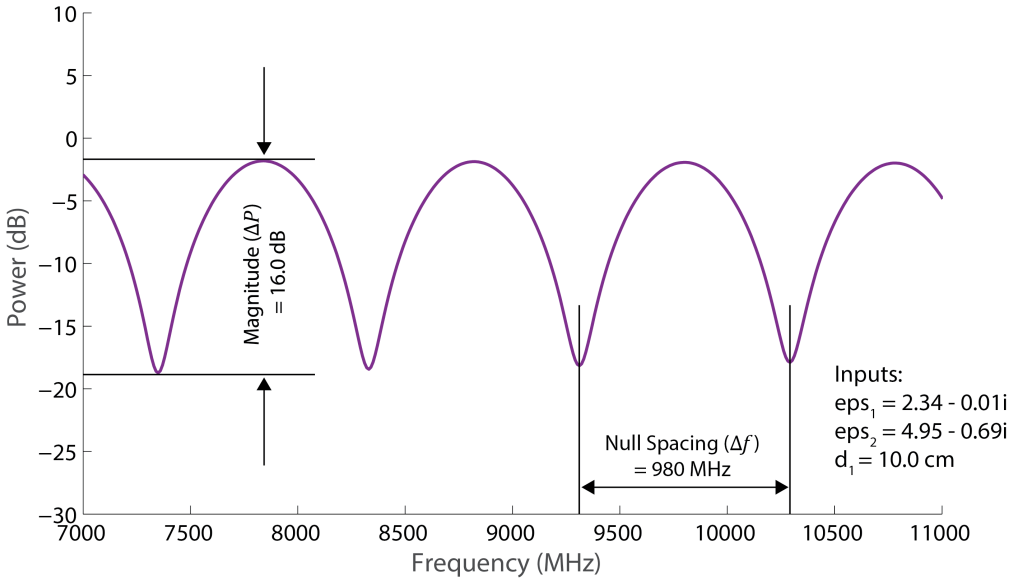

Figure 33. An interference pattern from a two-layer model showing the null spacing (Δf) and magnitude (ΔP).

We begin the inversion using the null spacing (Δf) and some assumed or a priori knowledge of the relative permittivity of each layer. Figure 34 shows an exponential fit for six different soils with relative permittivities (ε_1) ranging from 1.5 to 4.0 assuming a bottom layer (ε_2) of dry concrete. Comparing this to Figure 27 and Figure 28 we see there is a much smaller range in the potential depth solutions for any given null spacing and so any value of ε_1 should get us fairly close to correct depth. If we make our standard assumption of $\varepsilon_1 \cong 2.5$ and measure a null spacing of $\Delta f \cong 980\ MHz$ then we would find a layer depth $d_1 \cong 10.4\ cm$.

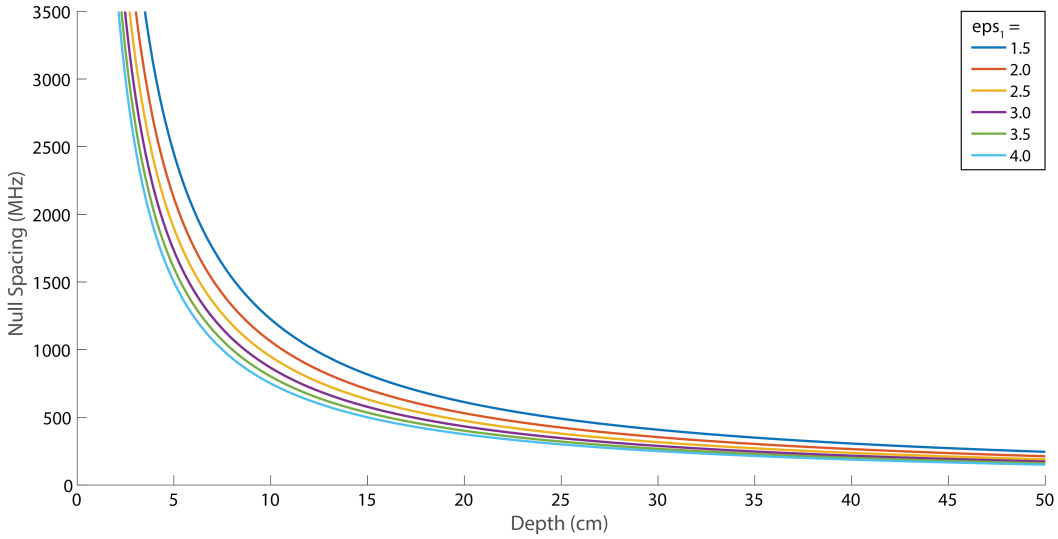

Figure 34. Relationship between the depth of the first layer (d_1) and the null spacing (Δf) for $\varepsilon_1 = 1.5, 2.0, 2.5, 3.0, 3.5,$ and 4.0.

Like we did with the incidence angle, the next step is to measure the magnitude of the null (ΔP). Now, the magnitude of the null (ΔP) is a function of both the depth of the top layer and the ratio of the relative permittivities ($\varepsilon_2/\varepsilon_1$), but it is most sensitive to the relative permittivity of the top layer (ε_1). If we assume that the bottom layer (ε_2) is made of something similar to concrete or bedrock we can use this assumption to check and improve our initial guess

of (ε_1). Figure 35 shows the null magnitude for six different soils with relative permittivities (ε_1) ranging from 1.5 to 4.0 and depths (d_1) up to 50 cm. From this figure, we can see that $\varepsilon_1 \cong 2.5$ should give us a null magnitude of $\Delta P \cong 15\ dB$ which is close to our measured value of 16.0 dB. To improve on our results, we would then iterate over a range of similar depths and relative permittivities until we found the best fit to our measured data.

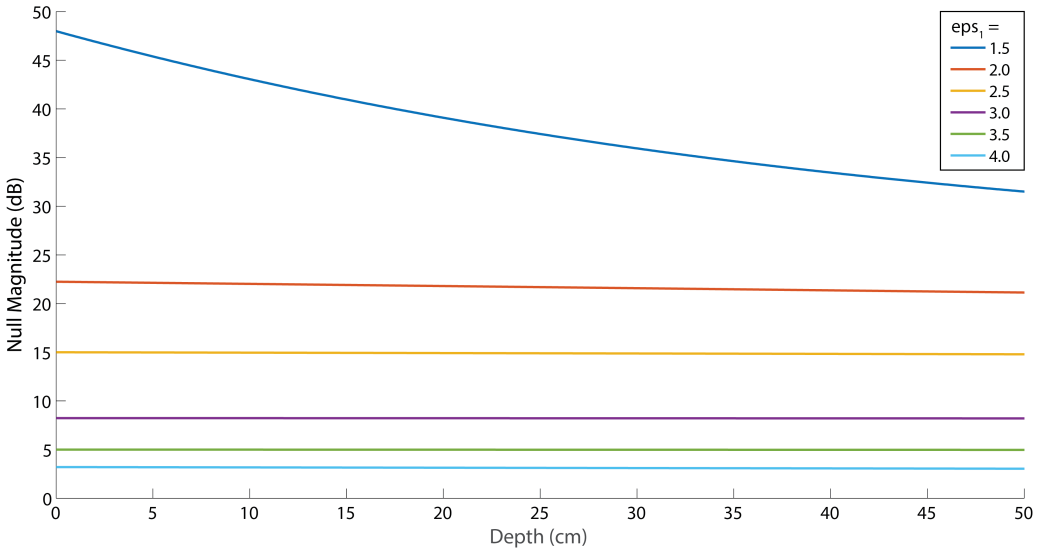

Figure 35. Relationship between the depth of the first layer (d_1) and the null magnitude (ΔP) for $\varepsilon_1 = 1.5, 2.0, 2.5, 3.0, 3.5,$ and 4.0.

Now, if we have the ability to change both the frequency and the incidence angle this becomes and even more powerful tool to investigate the subsurface soil properties. Figure 36 and Figure 37 show depth contours resulting from a combination of the frequency derived null spacing (Δf) and the incidence angle (θ_i). This additional data can be used to increase our confidence in the relative permittivity and depth measurements derived from an inversion.

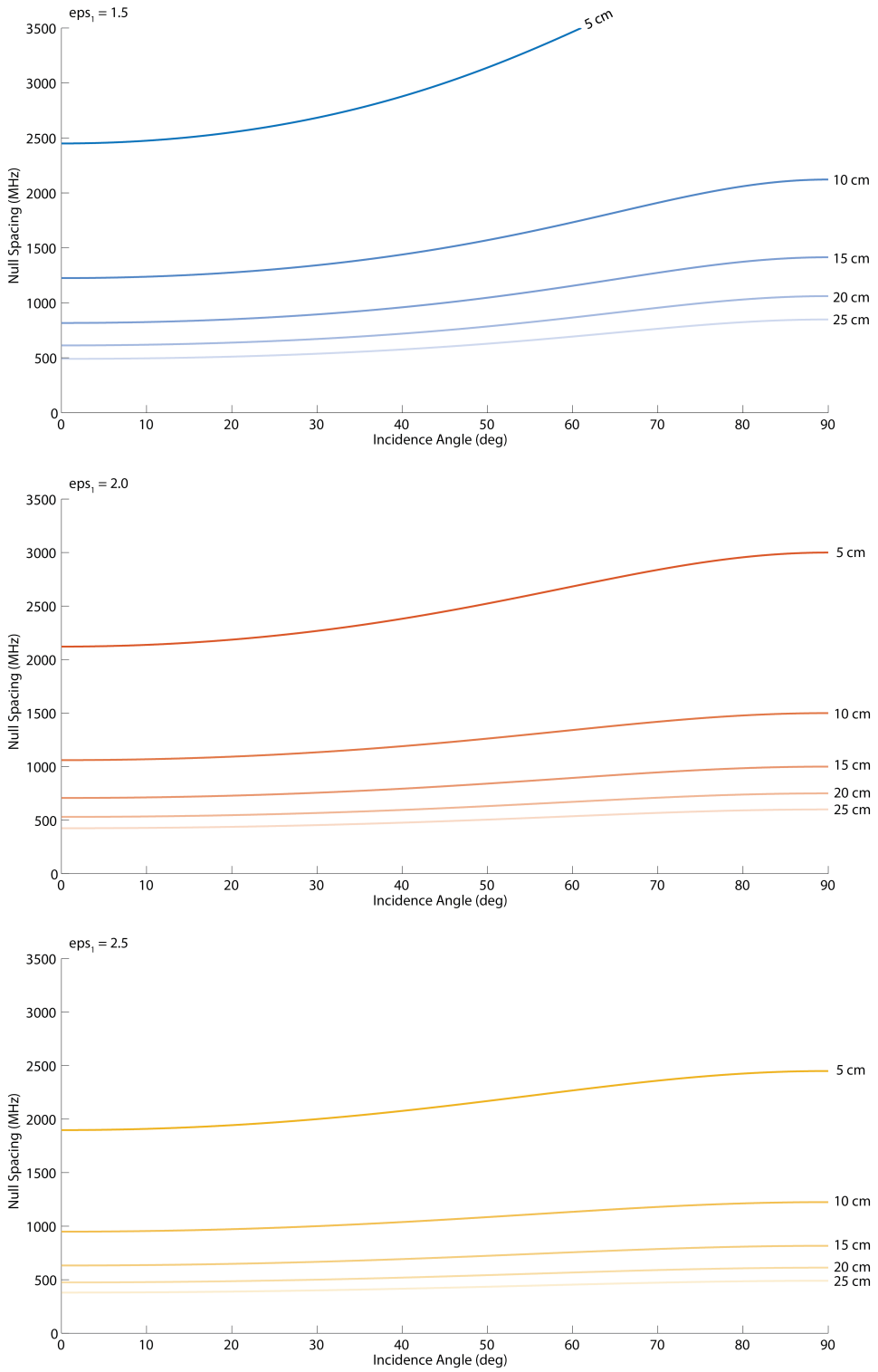

Figure 36. Relationship between the incidence angle (θ_i) and the null spacing (Δf) for $\varepsilon_1 = 1.5$ (top), for $\varepsilon_1 = 2.0$ (middle) and for $\varepsilon_1 = 2.5$ (bottom).

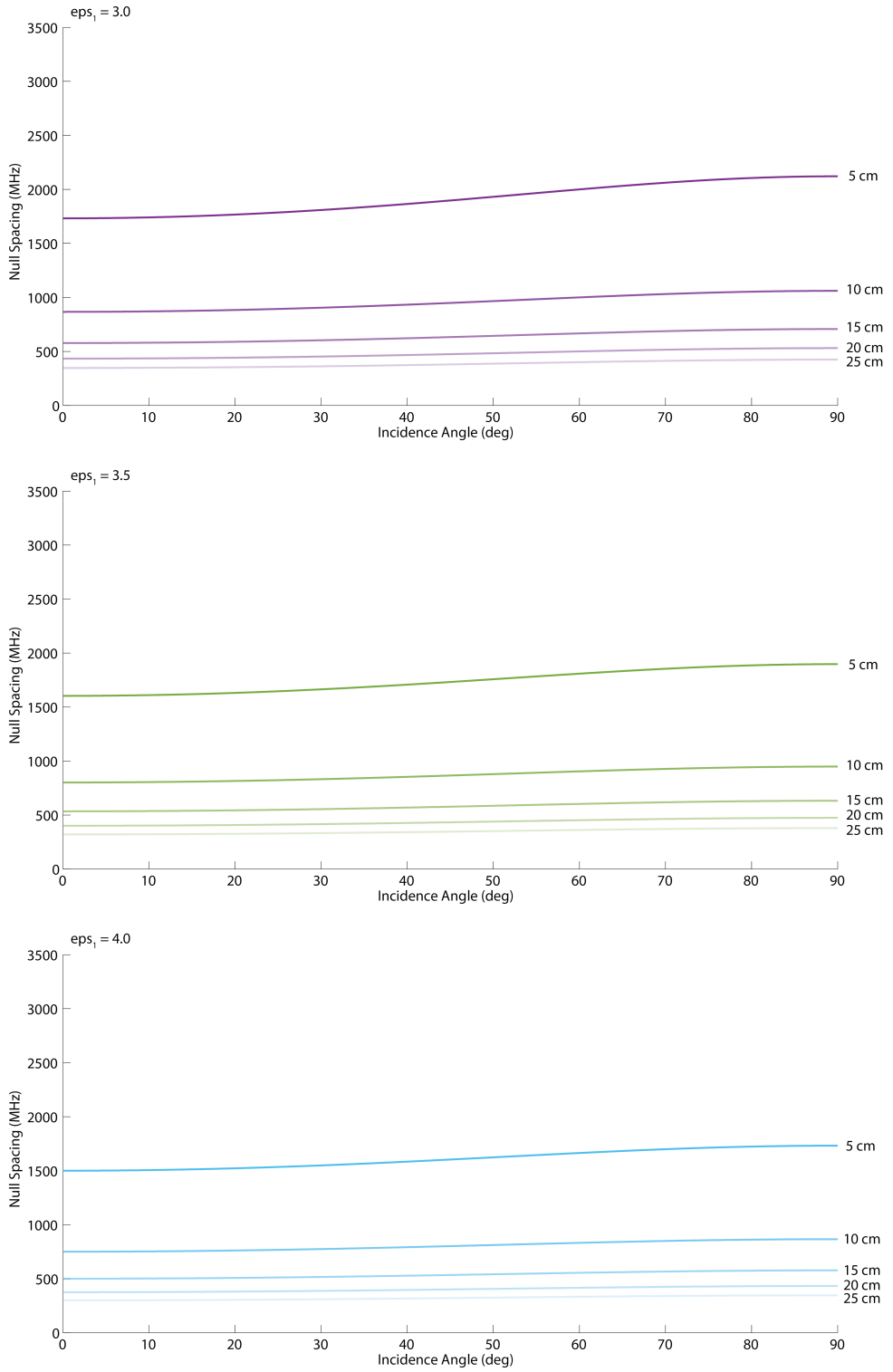

Figure 37. Relationship between the incidence angle (θ_i) and the null spacing (Δf) for $\varepsilon_1 = 3.0$ (top), for $\varepsilon_1 = 3.5$ (middle) and for $\varepsilon_1 = 4.0$ (bottom).

Chapter 5. Laboratory Experiments

5.1 Sandbox Setup and Geometry

To verify that the ray tracing model correctly predicts the behavior and interference patterns resulting from a multi-layer bistatic radar reflections we created a laboratory apparatus to experimentally simulate this geometry. We started by building a large aluminum sandbox frame measuring 3.65 m (length) x 1.88 m (width) x 0.50 m (height). Mounted on top of this structure we created a linear bearing system and pivot system to support and manipulate two linearly polarized horn antennas. A CAD model of the structure is shown in Figure 38. Note that in this figure, the fixed geometric quantities are shown in upper case and the variables we can change are shown in lower case. To minimize extraneous radar reflections off this supporting structure we covered all conductive surfaces with Emerson & Cuming Eccosorb ANW-77 microwave absorber and built the antenna arms out of Garolite G-10 fiberglass. Underlying this structure, we laid out a Mylar sheet and covered it with 4.5 cm thick uniform concrete tiles. We also had the option to add or remove an aluminum plate measuring 305 cm x 182 cm for testing or calibration purposes on top of the concrete tile.

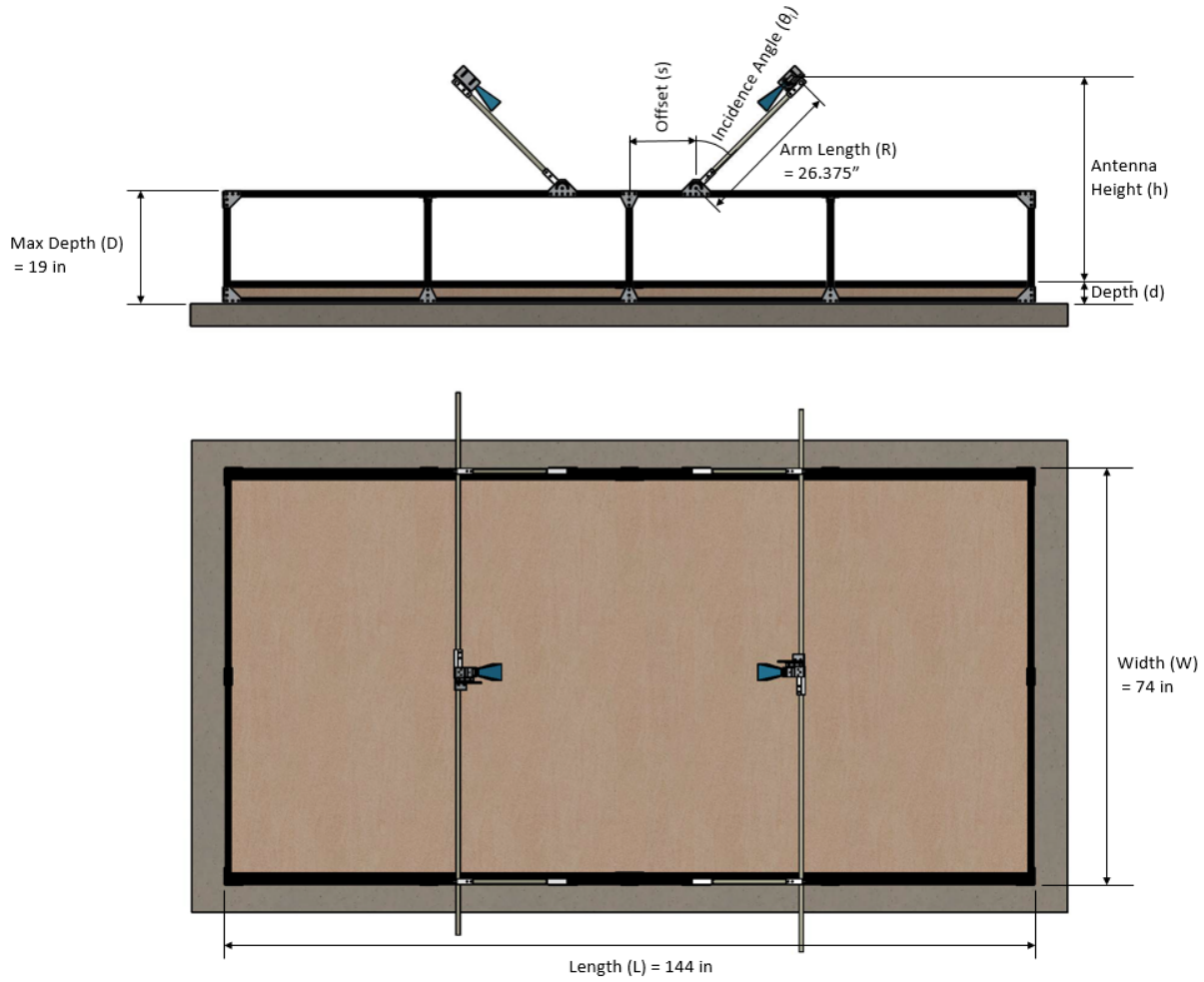

Figure 38. The bistatic radar test setup with two linearly polarized antennas suspended over a dry sandbox.

The two antennas selected for our experiments were Pasternak Enterprises PE9857/NF-15 standard gain horns with 30° beam width. Since we were primarily interested in understanding the potential to use an X-band uplink as a signal of opportunity, the PE9857 offered nice coverage of this range with a bandwidth from 7 to 11 GHz and a gain of 15 dB. These were connected to an Agilent 8722ES Network Analyzer which was used to collect and log the data. The network analyzer served another important role in that it allowed us to apply a

time gate and thereby eliminate the direct path between the antennas and any extraneous reflections from the room. This time gate helped to isolate the reflected signals from the soil and subsurface layers, but it was limited by the fact that as the incidence angle increases the path length between the direct and reflected signals becomes closer. This meant it was harder to apply the time gate and so measurements at incidence angles above ~55° became less reliable. The nominal orientation of the antennas was set to measure the vertical polarization (V-pol), but these can also be rotated in their mounts to capture the horizontal polarization (H-pol). All of the results reported in this chapter are in fact in the V-pol. To simulate a circularly polarized signal, measurements would need to be taken at both orientations and then combined in post-processing. The incidence angle and height of the surface were measured using a Bosch GLM 80 Laser Distance and Angle Measurer which was fixed to the antenna mounts (see Figure 41). This system has a stated accuracy of ± 0.15 cm and ±0.2°. A CAD model of the antenna mount is provided in Figure 39.

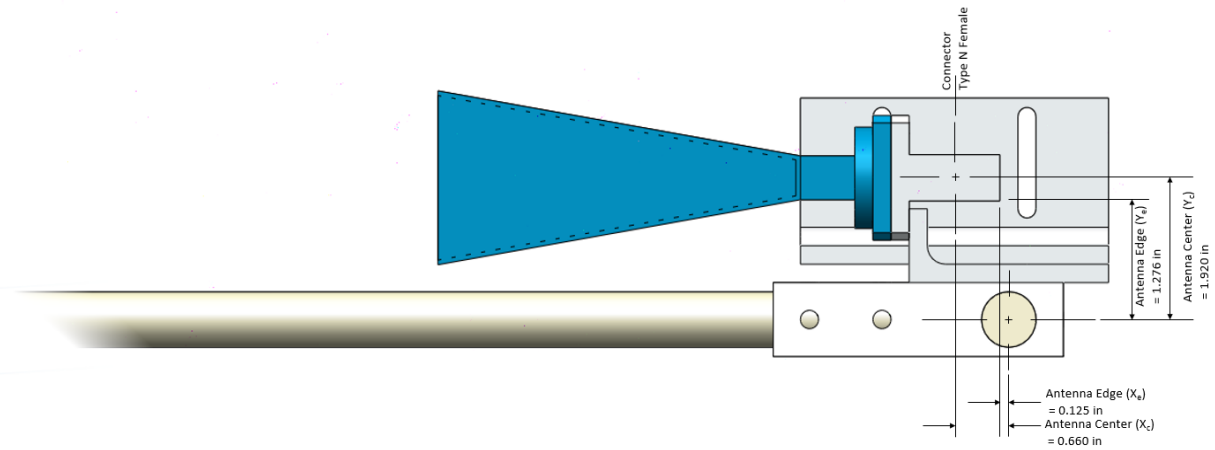

Figure 39. Details on the geometry and design of the antenna mount.

In the numerical model, one of the important inputs is the height of the two antennas relative to the soil surface. Based on the CAD models and measurements taken in the lab, we calculated the antenna height, h for this geometry using the equation:

$$h = (D - d) + (R - X_C)\cos\theta_i + Y_C \sin\theta_i \,. \tag{5.1.1}$$

Here D is the maximum depth of the sandbox, d is the measured depth of the top soil layer, R is the arm length above the pivot point, X_C is the radial distance between the antenna mount and the Type-N connector on the antenna, Y_C is similarly the distance between the antenna mount and the Type-N connector normal to the arm, and θ_i is the incidence angle of the antenna. Table 5.1 provides a reference for the antenna height corresponding to several incidence angles.

Incidence Angle (deg)	Antenna Height (cm)
0	113.5
5	113.8
10	113.5
15	112.5
20	111.3
25	109.5
30	107.2
35	104.6
40	101.3
45	97.8
50	94.0
55	89.7
60	85.1
65	80.3
70	75.2
75	69.9
80	64.5
85	58.9
90	53.1

Table 5.1. Antenna height corresponding to each incidence angle for the case when $d_1 = 0$ cm.

We tested fifteen different soil simulants which could be purchased from a local home improvement store and ultimately chose three for further testing. The first was a volcanic pumice with a specific density of 1.49 g/cm^3, the second was a dry sand with a specific density of 1.78 g/cm^3, and the third was a solid concrete brick with a specific density of 1.97 g/cm^3. These three were selected due to their relatively low water content and unique densities which, as we know, relates to the relative permittivity as well (Ulaby et al., 1990). In modelling these materials, we will use the relative permittivity values of 2.72 for pumice (Rust et al. 1999; Ulaby et al. 1990), 2.89 for sand which was measured directly (See Section 2.1), and a value 4.95 for dry concrete (Soutsas et al., 2001).

The moisture content of the three samples was verified by measuring the sample mass before and after baking at 250 F for 72 hours and was found to be less than 0.1% water by mass in all three cases. We interpret this to mean that each sample is extremely dry and should serve as a good analog to the rocks present in the Martian regolith.

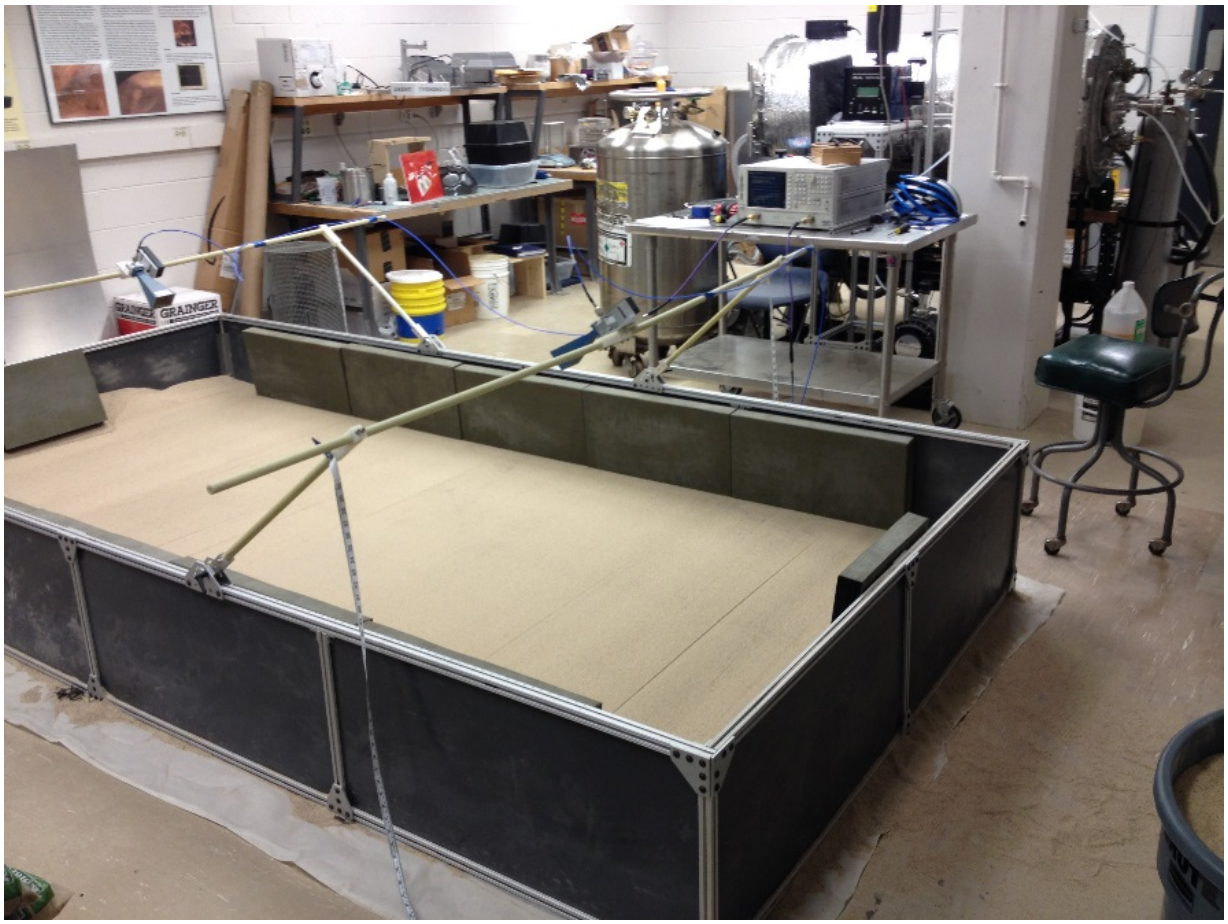

Figure 40. Side view of the laboratory apparatus with the sandbox.

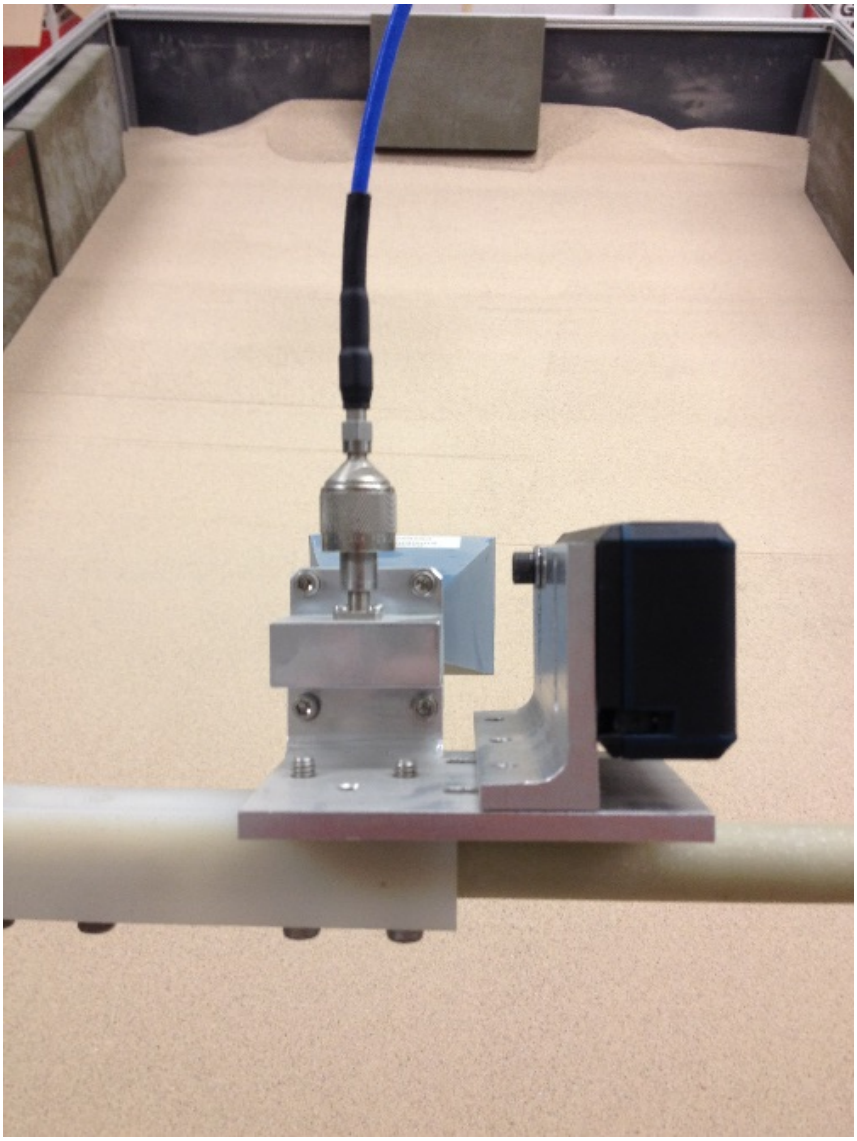

Figure 41. Close up of an antenna showing the mount and the placement of the Bosch GLM 80 Laser Distance and Angle Measurer.

5.2 Lab Results: Reflection off an Aluminum Plate

As a first test, we decided to look at the reflected power of the flat aluminum plate at the base of the sandbox. This simple case allowed a quick sanity check on our model and sandbox results. Since we expect the aluminum to act as a perfect reflector we expect a relatively flat line on this plot (See Figure 42). While this is true for the most part, we do see a departure from that at higher incidence angles. We think this is likely due to the increased mismatch between the footprint of the transmit and receive antennas as we increase the incidence angle. Recall that as the incidence angle changes so does the height of the antennas and so at higher incidence angles the antennas are also closer to the surface (Table 1). This data might be useful to implement as a calibration for the laboratory data at higher incidence angles, however, such a calibration has not been applied at this time.

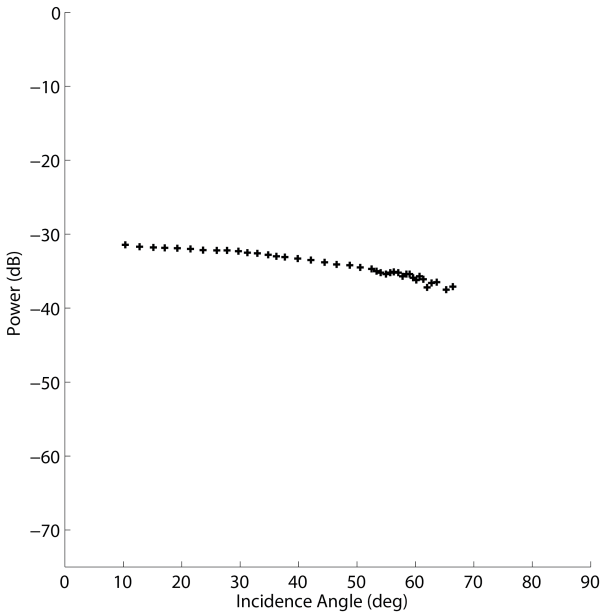

Figure 42. Reflected power with an aluminum plate located at the base of the sandbox.

5.3 Lab Results: Reflection off a Concrete Slab

Our second test was to look at the reflection off a dielectric slab. In this case we removed the metal plate and instead measured the reflection off a thin layer of concrete paving blocks. This is still a test with a single layer of material, but now we expect a lower reflected power as some of the EM wave will simply pass through the concrete instead of being reflected. In Figure 43 we see the reflected power drop about 6 dB when compared to Figure 42. We also see some interesting features worth noting.

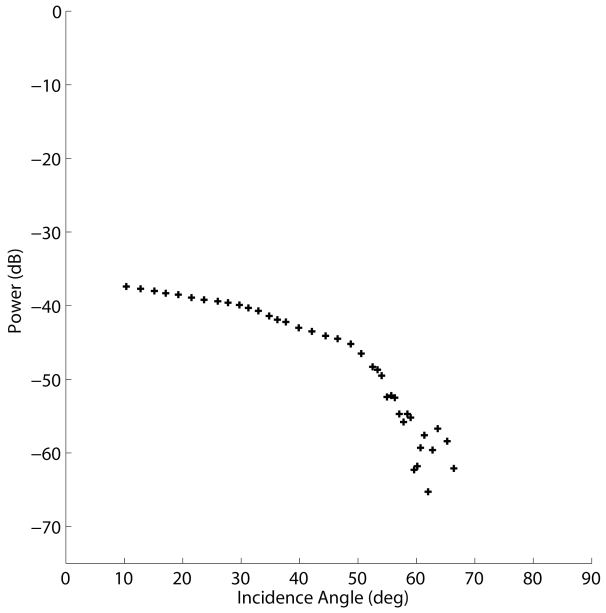

Figure 43. Reflected power with concrete paving blocks located at the base of the sandbox.

For one, if we assume that the dielectric constant of the concrete, $\varepsilon = 4.95 - 0.69i$ (Soutsas et al., 2001) then we would expect a Brewster angle around 65°. This could explain the minima we observe just over 60° with a subsequent rise in power at higher incidence angles. The second feature we notice is the slight waviness revealing two local maxima at around 30° and

50°, these features might by due to multipath interference between a reflected ray from the top of the concrete slab and a second ray path from the underlying concrete floor.

5.4 Lab Results: Interference Pattern Resulting from a Changing Incidence Angle

Our next step was to test a smooth layer of sand on top of the aluminum plate. For this experiment, we tried depths of 5.0 cm, 10.0 cm, 15.0 cm, and 20.0 cm of sand. In all cases the sand was carefully smoothed before measurements were taken at different incidence angles. For this first test, we really just wanted to verify that as the depth increased we would see more interference nulls in the signal. From bottom (5 cm) to top (20 cm) in Figure 44, we see the first indication of a null around 10 cm of depth and this becomes more pronounced at 15 cm and 20 cm. As the depth increases we are more likely to see a null in the signal and the interference pattern becomes more pronounced. This may seem contradictory to our model examples in Section 4.4, but it's important to remember that in this case the metal plate is far more reflective than the sand. As the sand increases in depth the power reflected off each interface air-sand and sand-aluminum becomes more closely matched and thereby leads to a deeper null in the interference pattern. Also, with a 5 cm step in depth it is hard to compare this data to the model which shows significant changes in the interference pattern with steps as small as 1 mm. This led us to rethink the experiments.

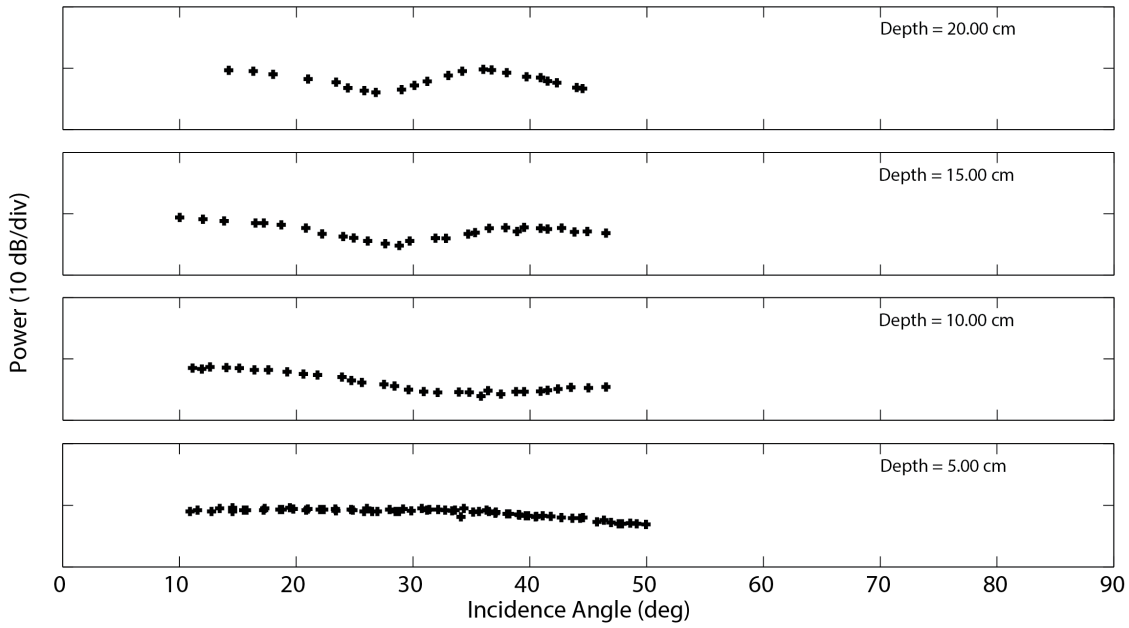

Figure 44. Laboratory measurements of the reflected power with $d_1 = 5$, 10, 15, and 20 cm of sand on top of an aluminum plate.

We made some improvements to the sandbox in order to reduce the step size to a minimum of 0.25 cm and repeated the tests near 10 cm. In Figure 45, we can see a slight shift in the peak power to lower incidence angles as we increase the depth. This gives us a little more confidence that our model is correctly simulating the behavior, but with the metal plate beneath the sand the nulls are still relatively shallow and hard to measure. By removing the aluminum plate and using the concrete tile as the second interface we should see better match in the reflected power from each layer and as a result develop a deeper null which is easier to identify and measure.

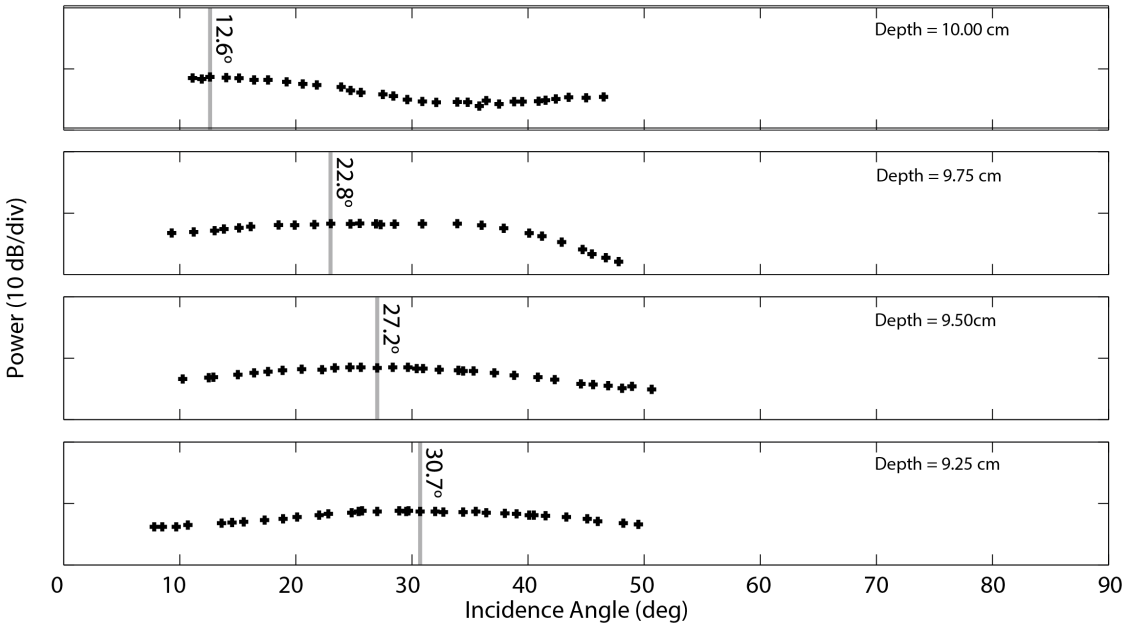

Figure 45. Laboratory measurements of the reflected power with $d_1 = 9.25, 9.50, 9.75$ and 10.00 cm of sand on top of an aluminum plate. The specific angles indicated denote the location of the measured maximum.

We removed the plate and repeated the measurements near 10 cm with a 0.25 cm step size in depth. A sample of these results is shown in Figure 46 along with model fits to the data. To do the fit we used $\varepsilon_1 = 2.89$ for the sand which was measured directly (See Section 2.1), and a value $\varepsilon_2 = 4.95$ for concrete (Soutsas et al., 2001) and then let the code find the depth at which the incidence angle of the nulls most closely matched what was observed. We generally see a good agreement between the model depth and the depth measured during the experiments, but there are a few cases such as 9.25 cm and 10.25 cm where there is more offset. We attribute this to uncertainty and variability in the actual measured depth of the sand during the experiments. Again, we see that as the depth increases the location of the null generally shifts to lower incidence angles, but this was not always the case – for example looking at the transition from 9.25 to 9.50 cm.

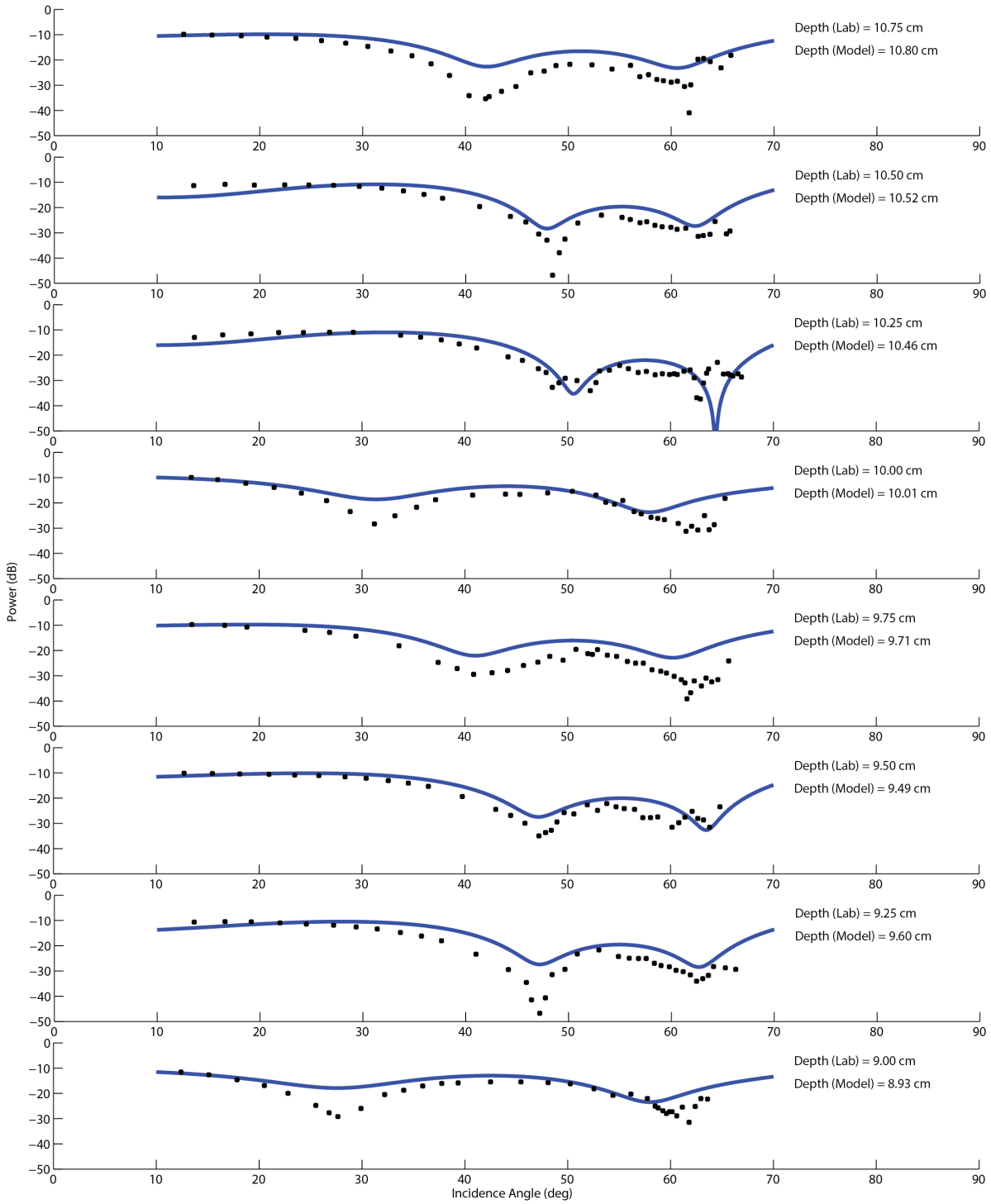

Figure 46. Laboratory measurements of the reflected power with d_1 = 9 to 10 cm, with a 0.25 cm step size, sand on top of an aluminum plate.

Another challenge we faced when conducting these experiments was the fact that the interference pattern would repeat. Consider for example the difference between 9 and 10 cm shown in Figure 47. If we did not have the labels on these two figures neither our eyes, nor the model would be able to tell them apart. A closer examination of the rate at which the location of the nulls changes reveals that the interference pattern repeats with as little as 1 cm change in depth and can move 10-20 degrees with each 0.25 cm step in depth. To really test the model we need more data and that leads us to study the interference pattern resulting from a changing frequency.

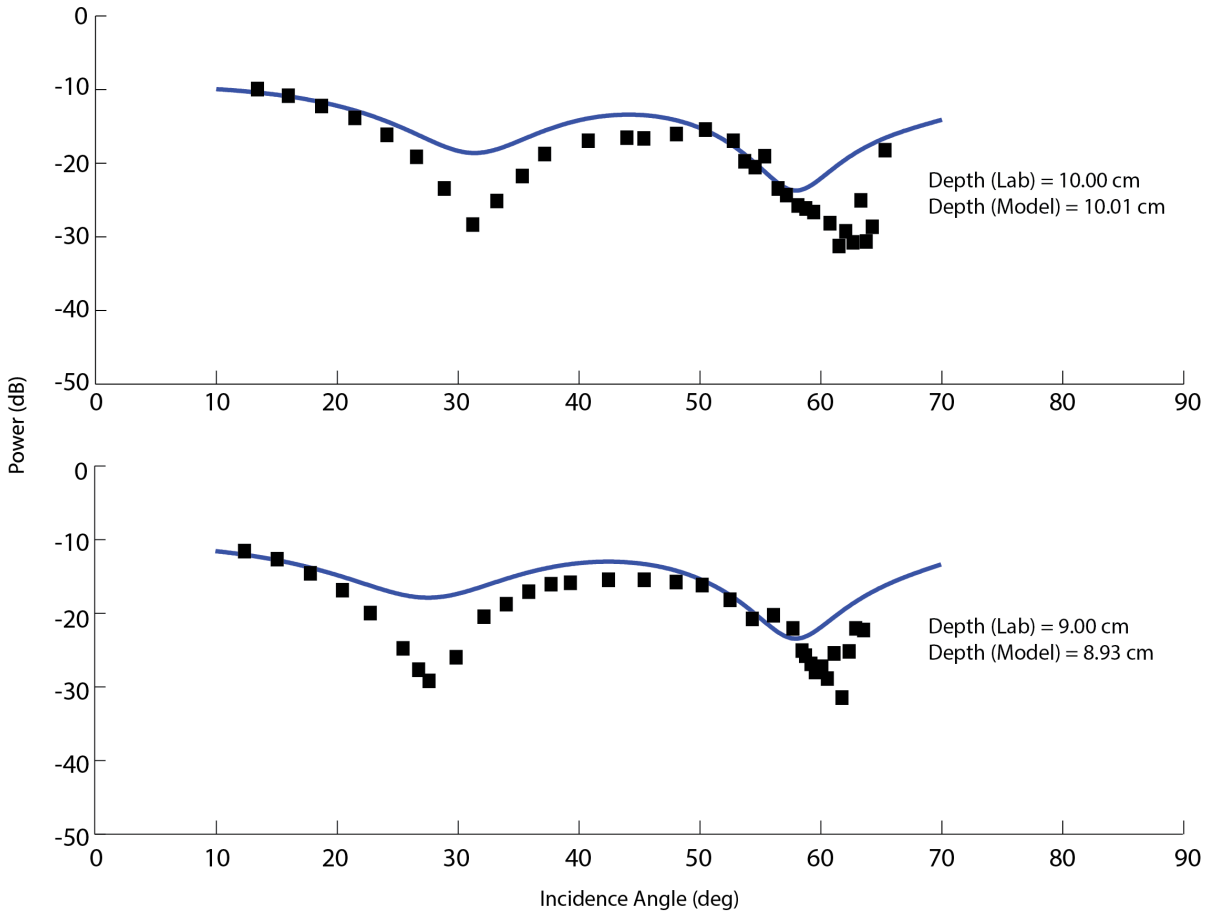

Figure 47. A close up of the differences between a sand depth of 9 and 10 cm.

5.5 Lab Results: Interference Pattern Resulting from a Changing Frequency

Using the same antennas and laboratory apparatus, we have the ability to get more data on the interference pattern by changing the frequency of the transmission. For these experiments we used a single antenna and held fixed at nadir ($\theta_i = 0°$) as we measured S11, the reflection coefficient, over the antenna's bandwidth from 7 to 11GHz. For these experiments we re-installed the metal plate and the sandbox was filled with dry sand. For each measurement the sand was smoothed and leveled at 0.25 cm thickness increments from 20 cm and sliced down to 6.5 cm. A small subset of this raw data is shown in Figure 48. Note that as the soil depth increases, the spacing between the nulls in the signal power decrease. That is to say the fading in the power signal becomes more frequent as the depth of the layer increases.

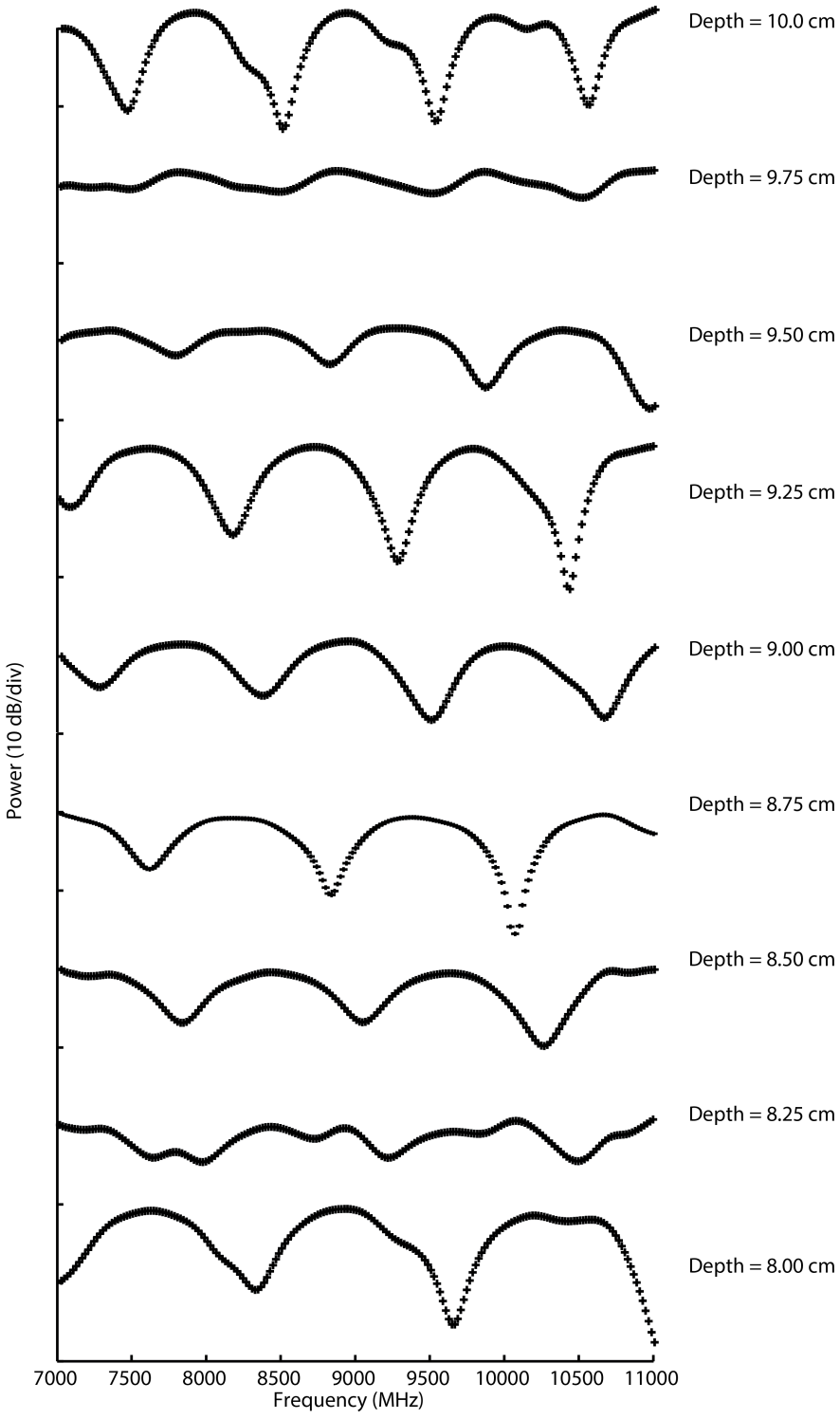

Figure 48. Interference pattern for 8-10 cm of sand above a metal plate, with the antenna pointing at nadir ($\theta_i = 0°$).

If we examine this data further and measure the frequency at which each local minima and maxima occurs, we see that the spacing between each of these frequencies is nearly equal. An example interference plot with each peak and null identified is shown in Figure 49. The spacing between these peaks and nulls is consistently ~1100 MHz for a measurement with 10 cm of sand over a metal plate.

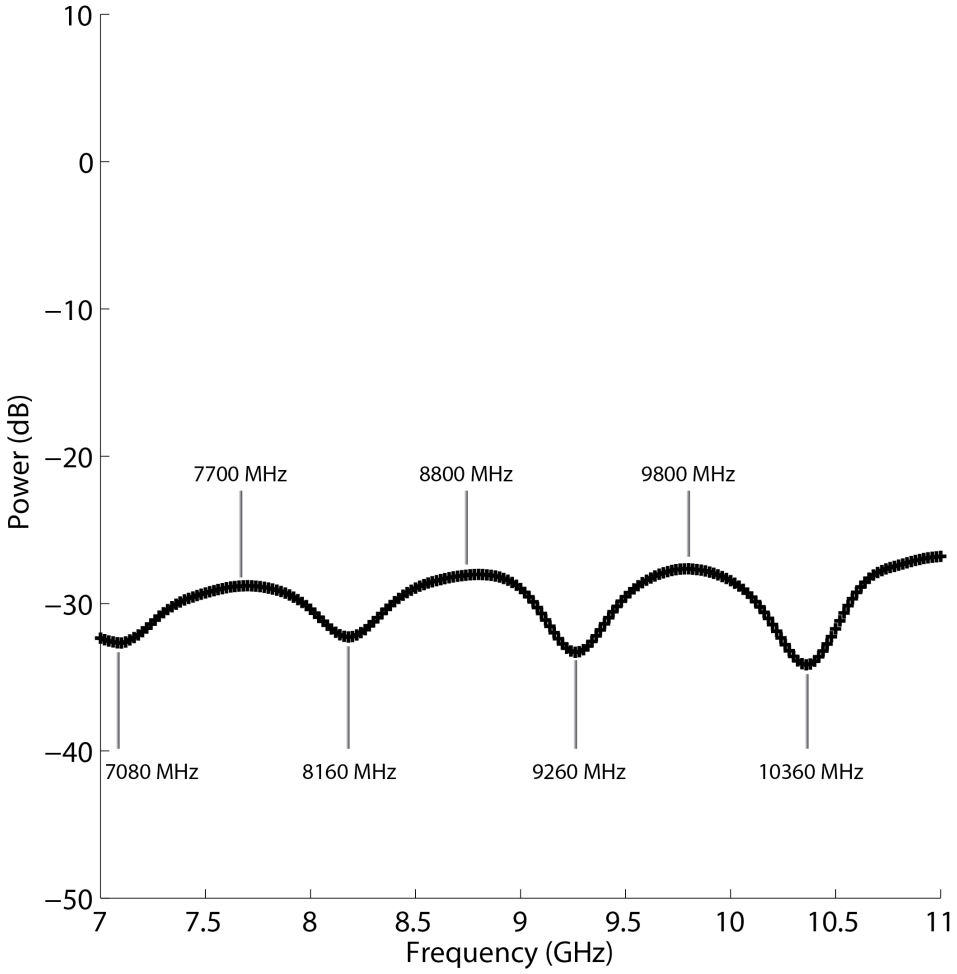

Figure 49. Interference pattern for 10 cm of sand above a metal plate, with the antenna pointing at nadir ($\theta_i = 0°$).

If we repeat this measurement for all of the depths from 6.25 to 20.00 cm then we can analyze the larger trend of how the depth influences the null spacing. The result can be seen in Figure 50 which shows that the relationship between the null spacing (Δf) and the sand depth (d_1) measured in the lab (black points) and compares it to the model output (blue line) assuming a two-layer model with $\varepsilon_1 = 2.89$ and $\varepsilon_2 = 4.95$.

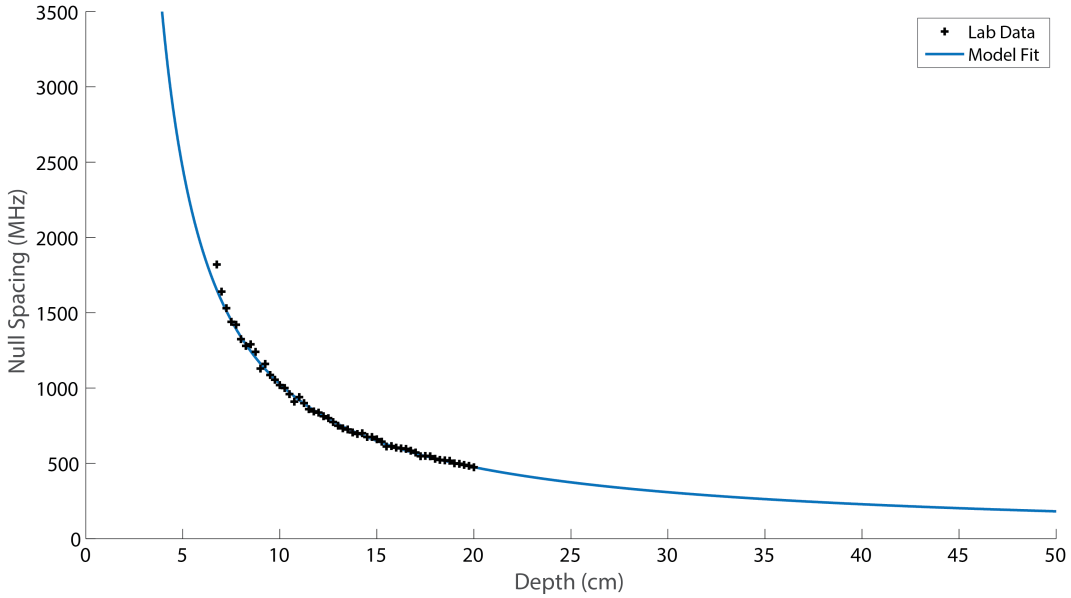

Figure 50. The null spacing (Δf) as a function of the sand depth (d_1) from 6.25 to 20 cm.

Finally, we wanted to look at the impact of the incidence angle on this retrieval. We chose three depths: 10, 15, and 20 cm for additional analysis. Then we went back to the earlier S21 measurements between antennas and swept the incidence angle from 10 to 50 degrees with a 2-degree step. As we increased the incidence angle we saw the interference pattern become stretched and distorted and also observed a slight increase in the spacing between the nulls. An example of the raw data is shown in Figure 51.

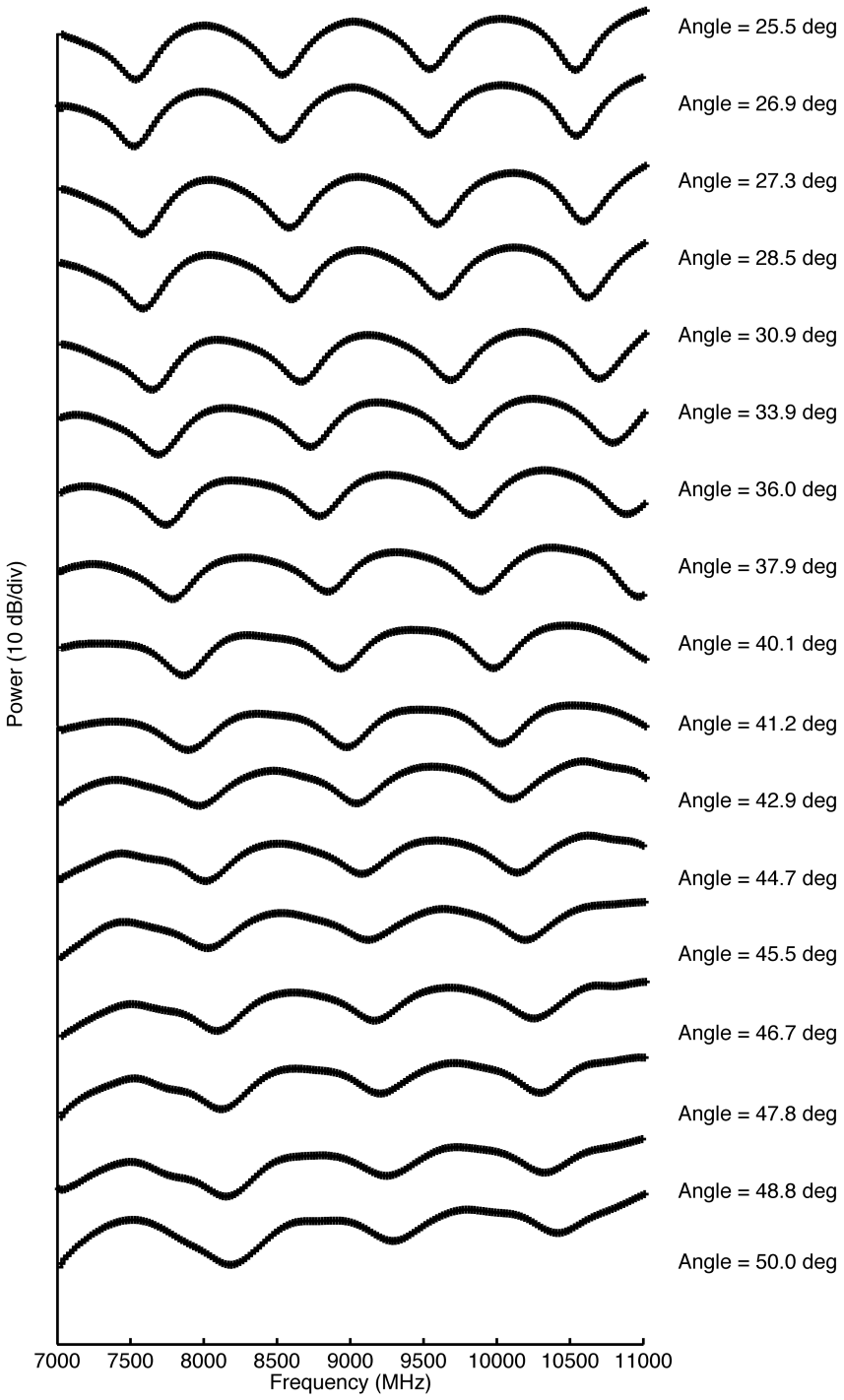

Figure 51. Interference pattern for 10 cm of sand above a metal plate, with the antennas pointing at various angles between 40° *and* 65°.

Taking the null spacing (Δf) for each angle measurement at the three depths we were able to create Figure 52. Here the trends look remarkably similar to the earlier model results in Figure 36 and Figure 37. While null spacing (Δf) is somewhat insensitive to the incidence angle of the antenna, the match between the laboratory results and the model here gives us more confidence in this method of analysis.

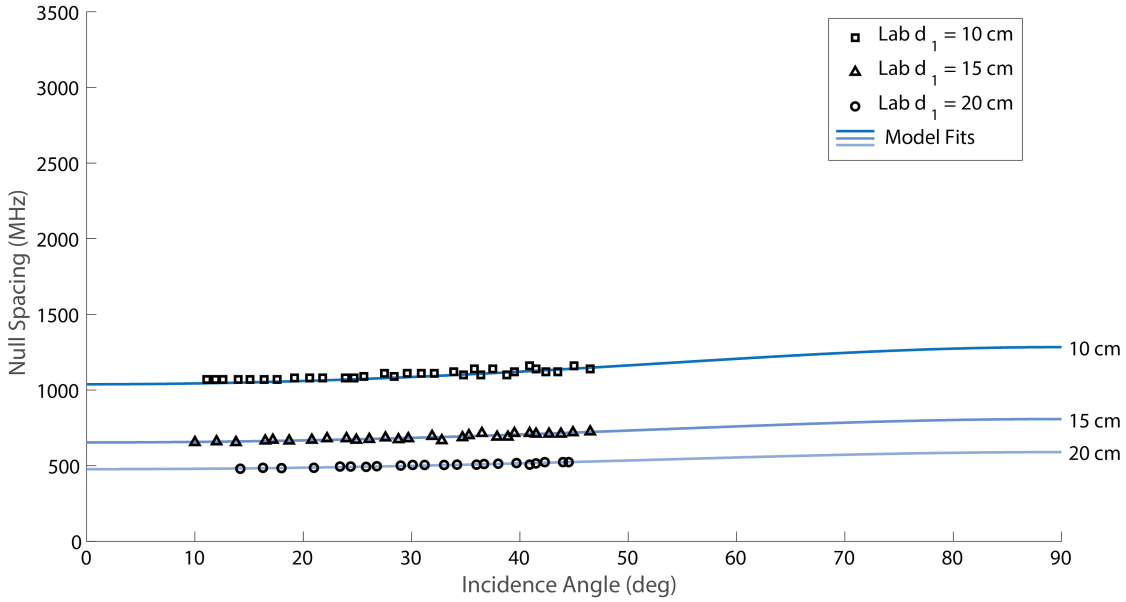

Figure 52. The null spacing (Δf) as a function of the incidence angle (θ_i) for $d_1 = 10$, 15, and 20 cm.

5.6 The Impact of Rocks and Periodic Ripples

The final round of experiments we conducted were designed to look at the impact of disturbed surfaces and scatters such as rocks on the retreival. We explored for different test cases: (1) surface ripples with a 3 cm peak to peak width and 1 cm depth, (2) surface ripples with a 12 cm peak to peak width and 3 cm depth, (3) rocks on the surface distributed evenly with a density of ~100 rocks/m^2, and (4) rocks embedded in the sand with a density of ~200 rocks/m^3.

The rocks used were a volcanic pumice with an average diameter of 3.5 cm and specific density of 1.49 g/cm^3. Figure 53 shows a picture depicting the three surface tests with a standard ruler for scale (30.5 cm in length). For reference, the wavelength of the signal is on the order of 2.7 cm (11 GHz) to 4.3 cm (7 GHz). That means that the 3 cm ripple and the rocks are both close to the scale of the wavelength, while the 12cm ripple is of the same scale or larger. In all cases, the surface was smoothed and leveled at 10 cm depth before introducing the texture for test.

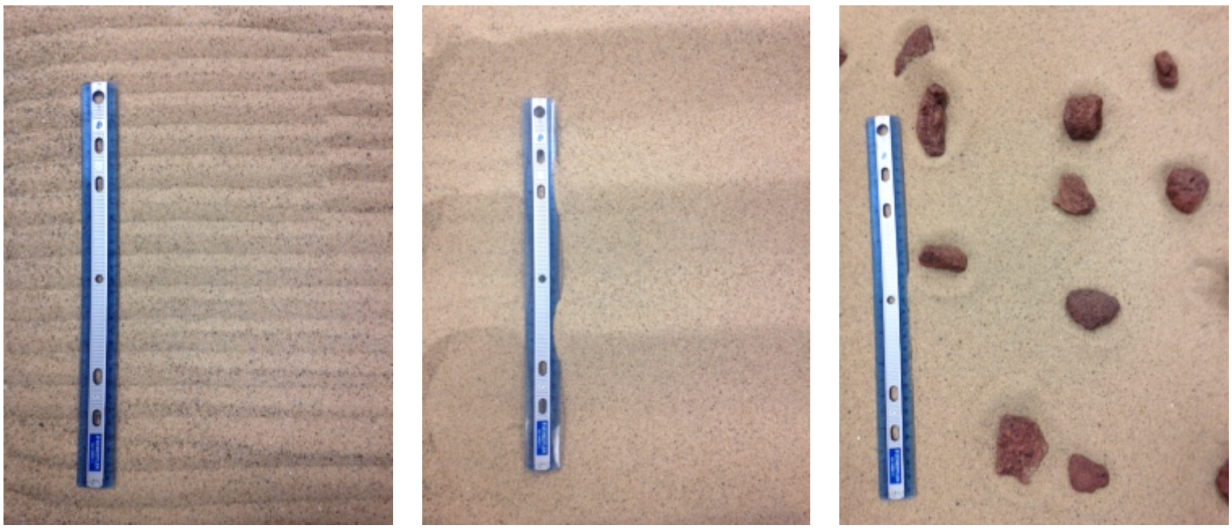

Figure 53. Examples of rough and periodic surfaces tested in the lab (Left) ripples with a 3 cm peak to peak width and 1 cm in depth, (Middle) ripples with a 12 cm peak to peak width and 3 cm deep, (Right) evenly distributed rocks with a density of ~100 rocks/m^2.

Looking at the raw interference pattern for these cases we tend to see a bit more noise or a more complex interference pattern than in the case of a smooth surface. In Figure 53 we have a smooth sand (top), sand with rocks on the surface (middle), and sand with rocks embedded in the layer (bottom). The depth and location of the nulls may vary between the three plots, but the mean null spacing (Δf) remains 480 MHz.

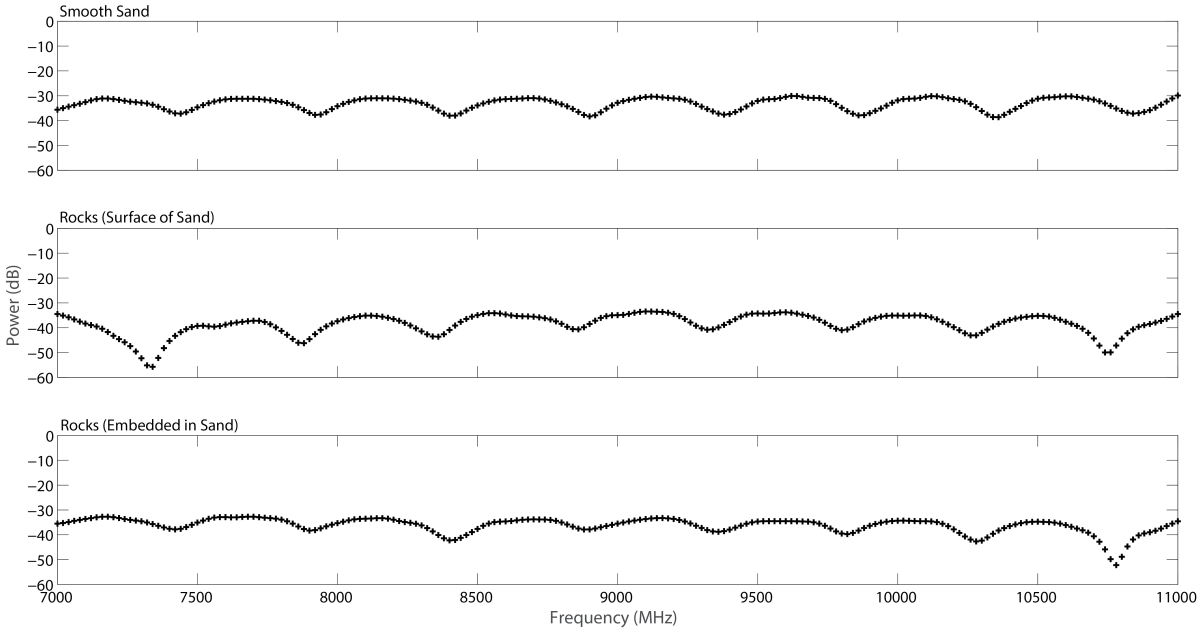

Figure 54. Interference pattern resulting from smooth sand (top), sand with rocks scattered on the surface (middle), and sand with rocks embedded in the first layer (bottom).

Next, we wanted to investigate the impact of different sizes and orientations of periodic ripples on the surface of the sand. The first was with the ripples aligned with the V-pol electric field an orientation we will call parallel. The second was with the lines cutting across the sandbox horizontally so that they were aligned perpendicular to the V-pol electric field. A sketch of these orientations is shown in Figure 55 with example interference patterns in Figure 56.

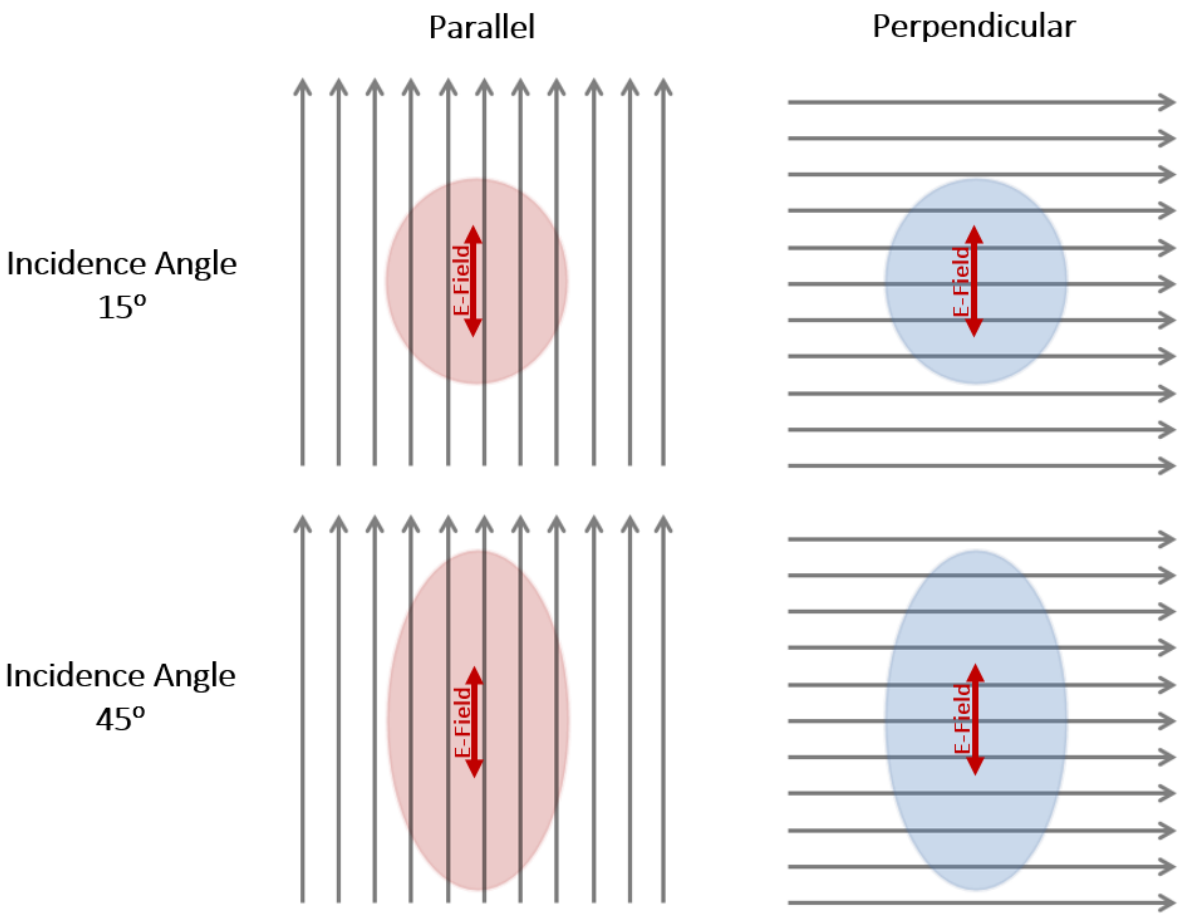

Figure 55. Orientation of the ripple aligned in two different vectors.

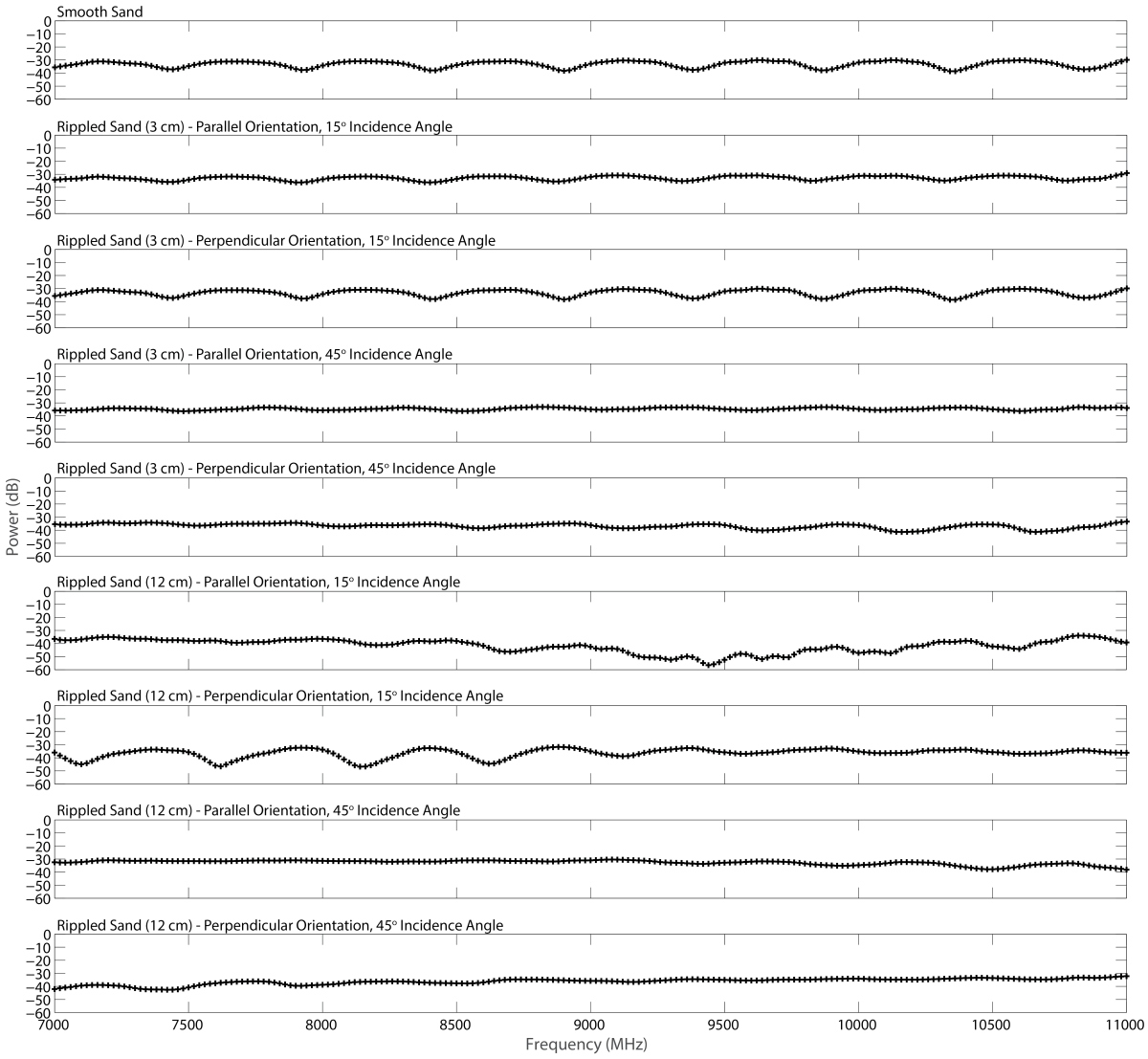

Figure 56. Interference pattern resulting from smooth sand (top) and periodic ripples of different sizes and orientations.

These plots show that the presence of periodic ripples will reduce the depth of the nulls and weaken the interference pattern. This is more noticeable in the interference patterns taken at 45° than those at 15°, implying that if we encounter disturbed surfaces there is an advantage to taking the measurements at lower incidence angles. Also, we see a greater perturbation to the interference pattern in the cases where the ripples are parallel to the V-pol electric field than

when it is perpendicular. This means some care should be taken when choosing the orientation of the receiver with respect to the ripple. Finally, we see a much larger impact when the size of the ripples exceeds the wavelength of the signal. In this case, the 12 cm ripple is much harder to analyze than the 3 cm ripple. This agrees with what we would expect from theory. Our model assumes a smooth surface which is an assumption which holds until the surface features approach the size of the wavelength. Even with all these considerations, the null spacing (Δf) is only slightly perturbed. With a frequency range spanning from 7 to 11 GHz we can still calculate the mean null spacing in all of our test cases and we see little change from that of the smooth sand. In Figure 57, a plot of the null spacing (Δf) for our four scenarios is compared against the smooth sand.

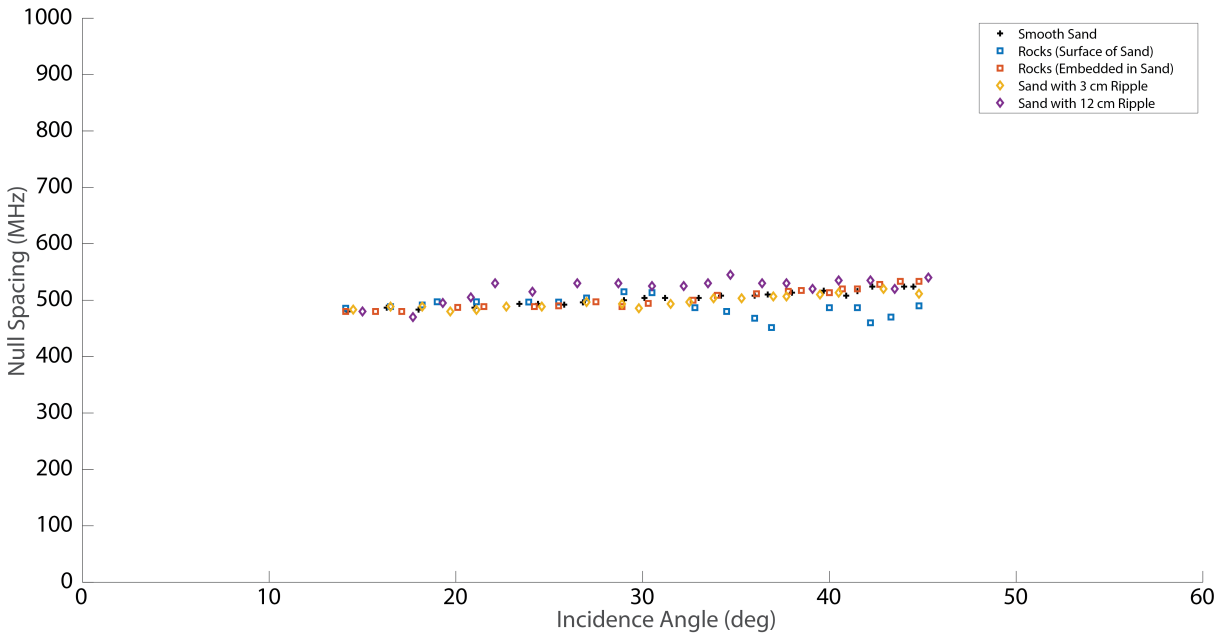

Figure 57. Comparison of the null spacing (Δf) for smooth surface, with rocks scattered on the surface, with rocks embedded in the sand, and with periodic ripples (perpendicular).

From this result, we conclude that small surface roughness features, even on the order of a wavelength have little effect on the null spacing (Δf) of the interference pattern. While a rough surface can result in more noise and a small offset when we look at the interference pattern, it doesn't appear to have a large effect on the Δf or retrieval of the layer depth. This is especially true when the incidence angle is small ($\theta_i < 20°$). This bodes well for the capacity to apply this type of measurement in the real world.

Chapter 6. Applications to Mars and Other Planetary Bodies

6.1 The Deep Space Network and a Circularly Polarized Signal

The Deep Space Network (DSN) consists of three facilities: Goldstone, California; Madrid, Spain; and Canberra, Australia. These sites are equidistant from each other and spaced approximately 120° of longitude apart, so that an interplanetary spacecraft can maintain constant communication with the Earth (Wolff, 2003; McConnell, 2018). Each site contains multiple radio antennas with parabolic dishes ranging in diameter from 26 meters to 70 meters. Most interplanetary spacecraft communicate to one of six 34-meter antennas. These are the newest and most efficient of the antennas at the DSN facilities and handle the majority of the throughput. Each facility also has one 70-meter antenna, which is the most sensitive (McConnell, 2018).

The first large antenna, DSS-14, was built at Goldstone in 1966 to track the Mariner 4 spacecraft on its journey past Mars. To maintain contact with the Voyager 2 spacecraft as it encountered Neptune, DSS-14 was then upgraded to 70 meters and two other 70-meter antennas were built at Madrid and Canberra (Wolff, 2003). These huge radio antennas are among the largest and most powerful in the world. The DSS-14 at Goldstone is particularly impressive and as part of the Solar System Radar program (Calhoun et al. 2007) was upgraded beyond the others to transmit a staggering 450 kW signal at X-band frequencies (Naidu et al. 2016). The transmitter is now capable of bouncing a signal off the moons of Jupiter and receiving the

reflection back on Earth (Slade, Benner and Silva, 2010). With this capability, it is possible to conduct experiments probing the subsurface of Mars.

The DSN dishes are built to transmit and receive circularly polarized signals. Thus far, we have considered the vertical and horizontal signal polarizations separately. In this chapter, we combine the two linear polarizations to simulate a circularly polarized signal.

6.2 Data from the Opportunity Rover

On January 25, 2004, a 34-meter Deep Space Network dish at Goldstone was making an open loop recording of the received X-band carrier during the Opportunity Rover's entry, descent and landing (EDL) sequence. The spacecraft entered the Martian atmosphere around 5:00 UTC and started a rapid series of deployments described by Figure 58 before coming to a rest at 5:07:15 UTC, upside down on panel 2 of the landing platform. A sketch showing the rough orientation of the lander on the surface is shown in Figure 59.

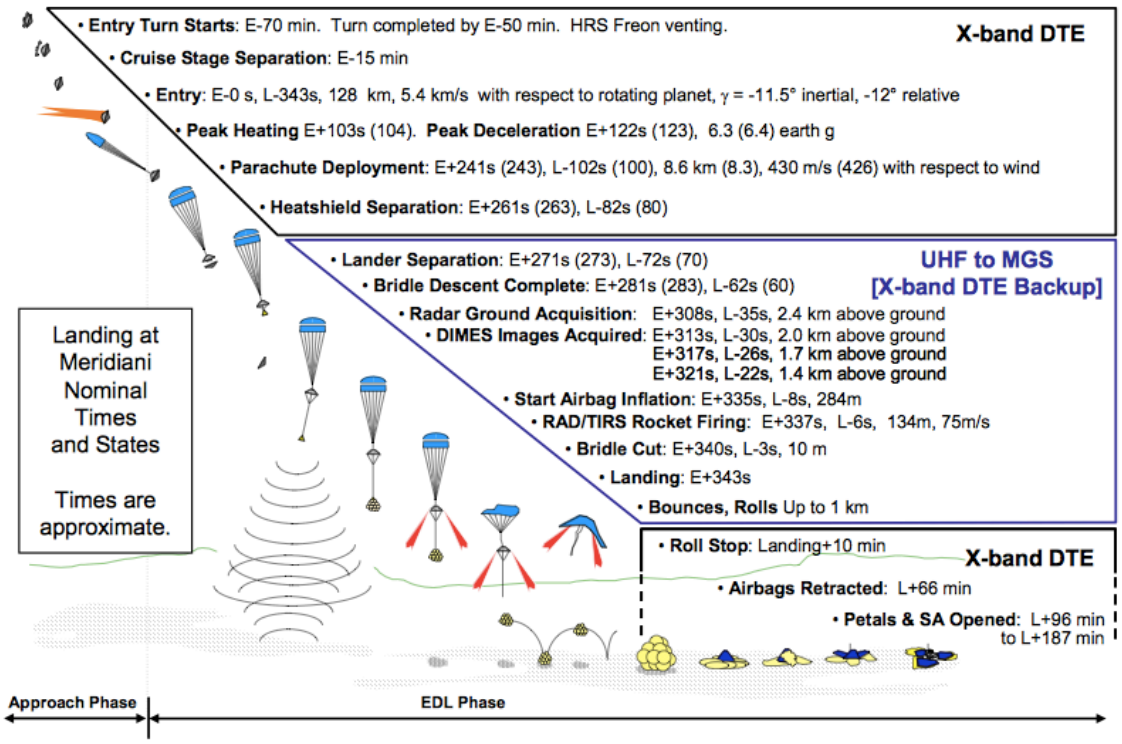

Figure 58. Opportunity Rover EDL Sequence reproduced from Taylor et al., 2005.

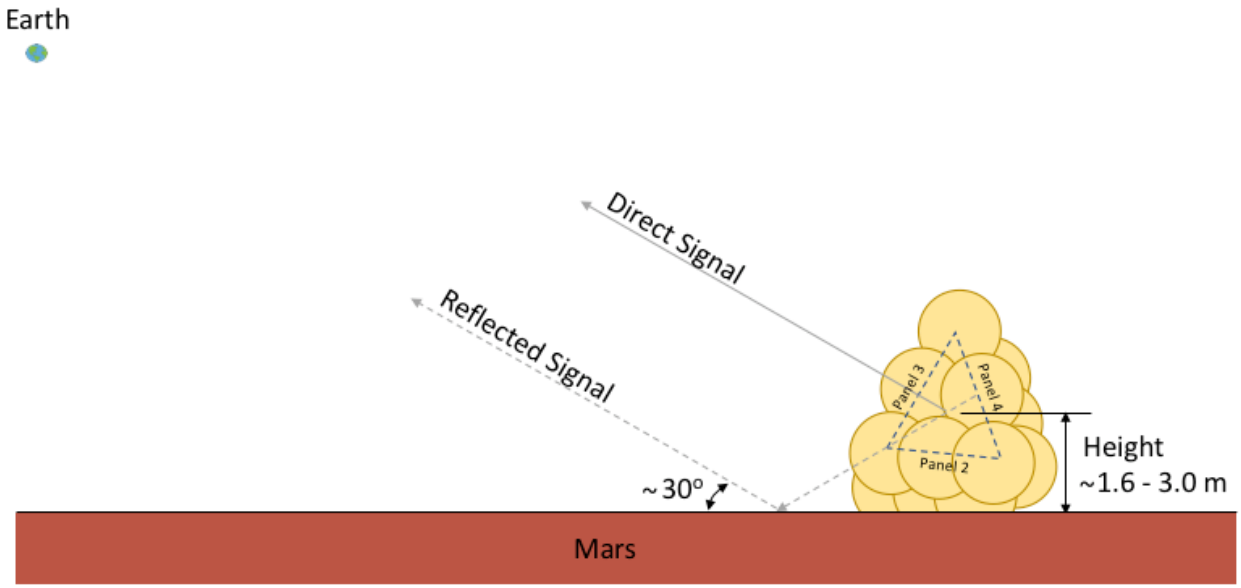

Figure 59. Opportunity Rover orientation after landing.

In this orientation, the spacecraft Petal Low Gain Antenna (PLGA) was pointed slightly down towards the surface of Mars and multipath fading was observed in the downlink. A plot of the open loop recording of the spacecraft's direct-to-Earth signal to noise ratio showing the multipath fading is shown in Figure 60.

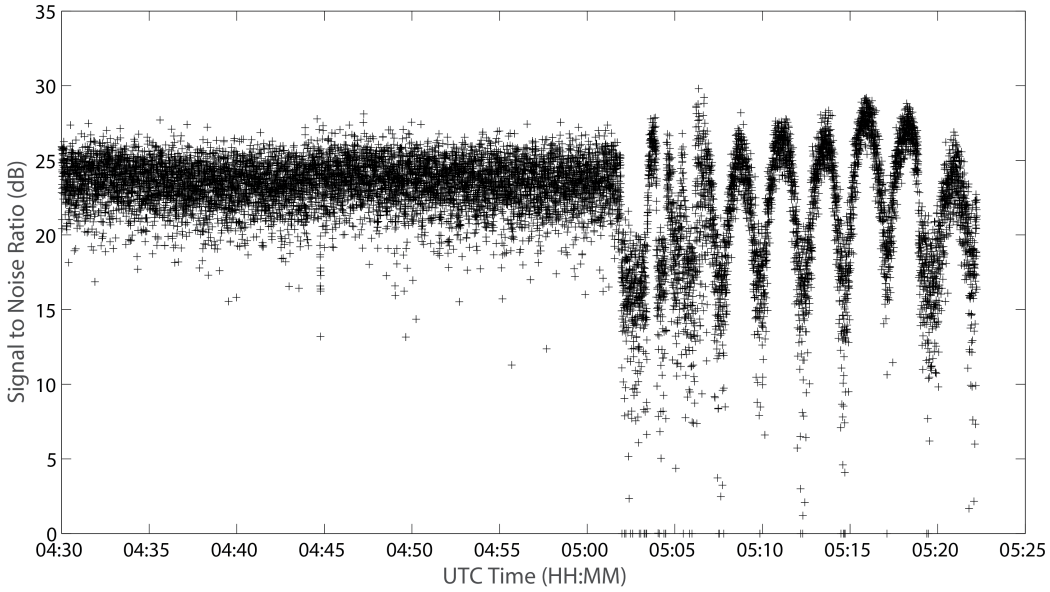

Figure 60. Opportunity Rover X-band carrier received power during Opportunity's EDL.

We can use the spacecraft's inertial sensors and results from the Satellite Tool Kit to determine the transmission geometry during this comm link. This allows us to convert the raw data in units of time to units of incidence angle and compare them with results from our numerical ray tracing model. Taking a moving average of the received power and binning the data to 0.01° steps we see seven distinct nulls in the data at 62.05°, 62.53°, 63.08°, 63.57°, 64.13°, 64.07°, and 65.2° (see Figure 64). The average spacing between nulls is 0.53° and the mean depth is 10.7 dB. Such a narrow spacing implies that the antenna height is on the order of meters. Using the numerical model developed for an X-band downlink at 8.425 GHz and a single

surface reflection we find the relationship between the antenna height and the null spacing (see Figure 61). If we draw a horizontal line across from a null spacing of 0.53° we can see that this corresponds to a range of antenna heights between 199.7 and 255.2 cm with a median value of 221.0 cm. This is reasonable considering each airbag is 1.6 to 1.8 m in diameter when deployed, each side of the tetrahedron is 3.5 m in length, and the PLGA is roughly centered on Panel 4 (Cadogan et al. 2002, Stein and Sandy, 2003).

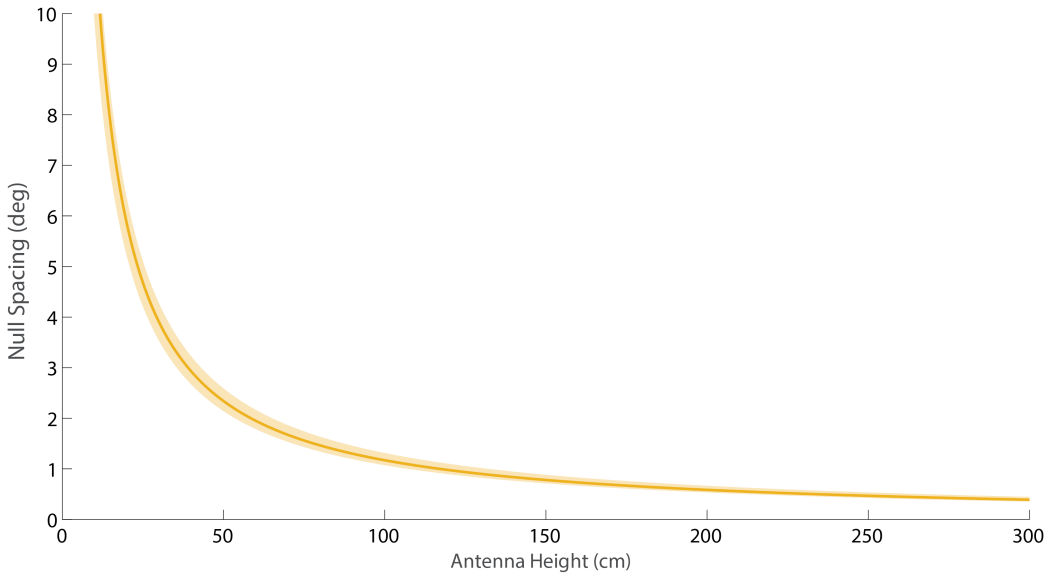

Figure 61. Relationship between the null spacing ($\Delta\theta_i$) and antenna height (h) derived from the model.

To refine this height measurement and determine the relative permittivity of the soil we want to match the magnitude of the null. We begin by importing the PLGA radiation pattern described in Section 3.8. We will assume that this antenna is pointed down such that its main beam is centered at -30°. With this information the model will allow us to plot a relationship between the average null magnitude and the relative permittivity of the soil (see Figure 62).

Drawing a horizontal line at an average null magnitude of 10.7 dB we find that relative permittivity of the soil is $\varepsilon_1 = 3.3$.

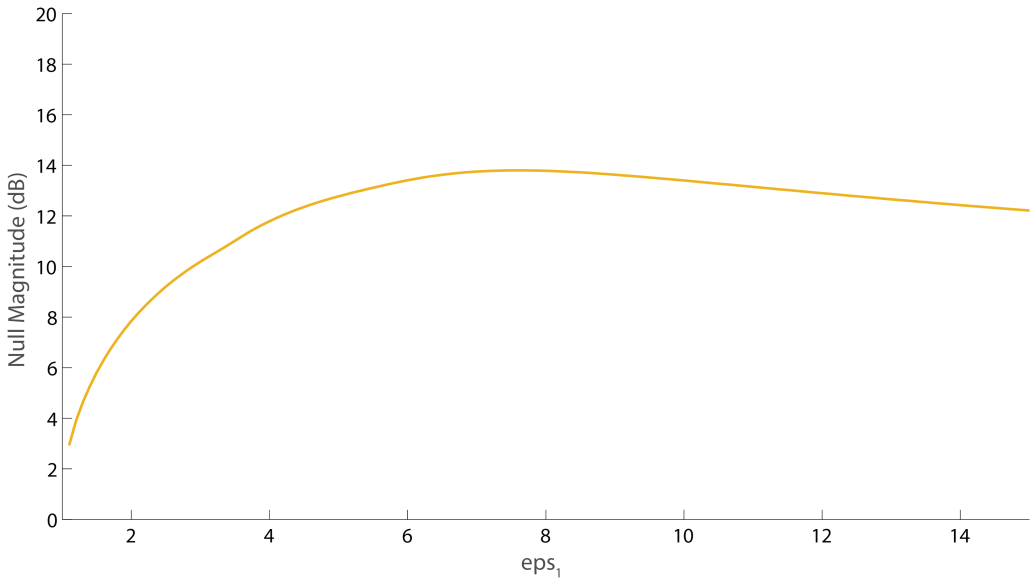

Figure 62. Relationship between the null magnitude (ΔP) and relative permittivity of the soil derived from the model.

Using $\varepsilon_1 = 3.3$ in our model, we can then improve the antenna height measurement and look for the best match to the observed signal. For example, in Figure 63 the black dots represent the range of potential antenna heights when $\varepsilon_1 = 3.3$. If we examine the line where the null spacing is 0.53°, we can refine the range of potential antenna heights to be between 208.9 to

224.4 cm. We then use this range of potential heights and search for the interference pattern which best fits the observed data.

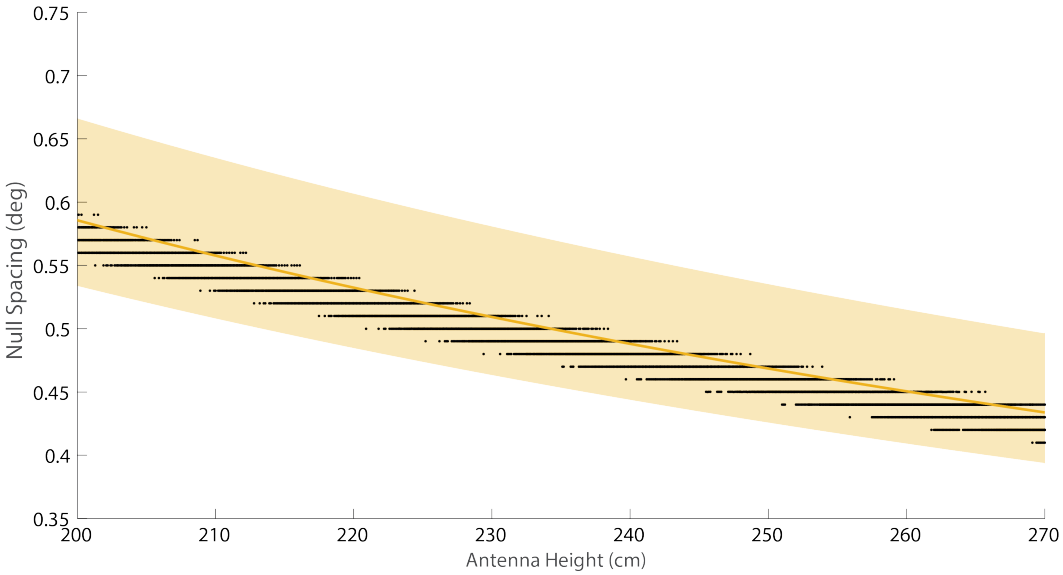

Figure 63. An improved estimate of the antenna height (black) with the knowledge that the relative permittivity of the soil is $\varepsilon_1 = 3.3$.

Figure 64 shows the interference pattern produced by numerical model with the best fit to the observed data. This is a single layer soil model with a relative permittivity of ε_1 = 3.3 and an antenna height of 219.6 cm. We can see that this matches the null spacing and magnitude well with a mean squared error of 4.94 dB.

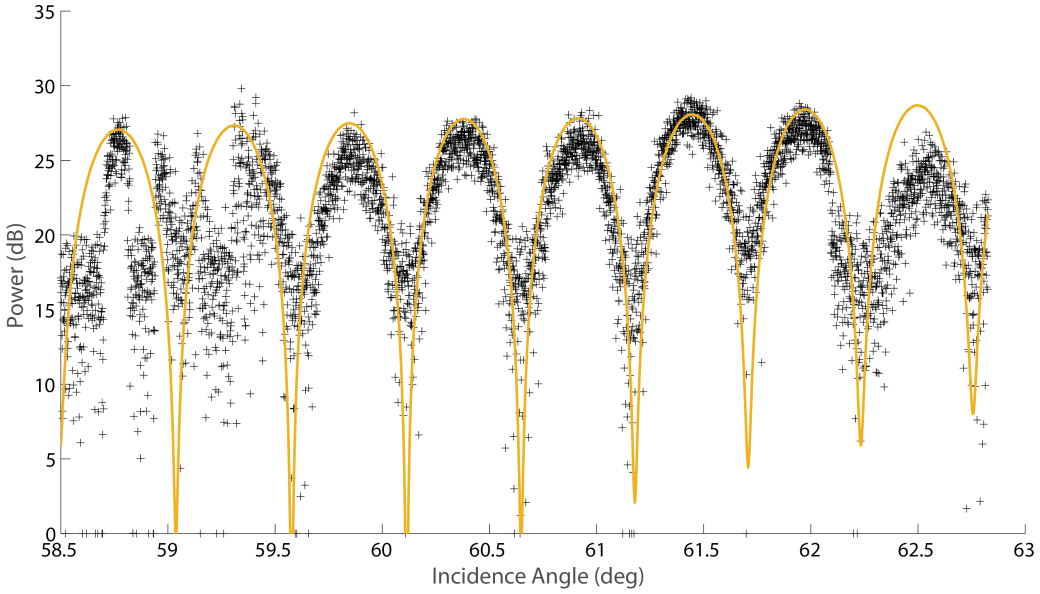

Figure 64. Opportunity Rover X-band carrier power as a function of incidence angle (black) and model fit (yellow).

6.3 Capabilities of the Curiosity Rover

One of the motivating factors behind this work was a proposal to use the Curiosity Rover or the 2020 Mars rover to make measurements of the soil properties on Mars. Here we demonstrate the potential to measure the relative permittivity of the soil and identify dielectric discontinuities along the rover's traverse. This scheme assumes a bistatic radar experiment using the existing spacecraft's telecommunications equipment including the MSL High Gain Antenna described in Section 3.8 and the Small Deep Space Transponder. The quantity we measure is the received signal power or alternatively the signal to noise ratio at the spacecraft. We will assume a continuous wave transmission using the 70-meter DSS-14 antenna and transmitter at Goldstone, and will assume a maximum transmission power of 450 kW (Naidu et al. 2016) at 7.145 GHz. In this experiment the spacecraft's High Gain Antenna points down at the surface of

Mars and follows the specular reflection point. To help build our understanding, we begin by imagining a scenario where the antenna is at a fixed height on the rover deck (1 meter) and able to point straight down. The resulting received power normalized to the power of the direct signal is shown in Figure 65.

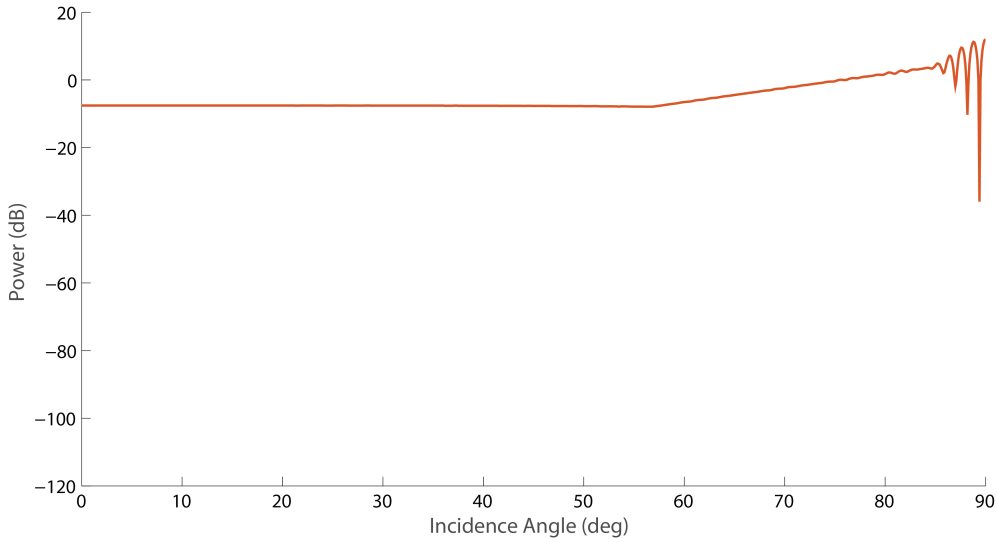

Figure 65. Reflected signal power received by MSL HGA with no pointing restrictions.

From 0° to 55°, the received power is constant because the main beam of the antenna is able to track the specular reflection point. At around 57° a notch is observed in the received signal which corresponds to the Brewster angle of the soil. Then, the reflected power gradually rises until ~85° where large interference nulls appear. In the region above 85°, both the direct and the reflected signals are received in the main beam of the antenna resulting in the interference nulls seen. Much like the case we observed with the Opportunity Rover in Section 6.2 these interference nulls are a function of the antenna height from the surface.

Now, let us consider the case in which the antenna has a hard stop at -35° like the Curiosity and Mars 2020 antennas. Figure 66 shows the reflected signal power in the case where

the pointing of the antenna is restricted. We still see the notch caused by the Brewster angle around 57° and the interference nulls near the horizon, but now we also have several deep nulls at incidence angles below 55°. These nulls are due to the radiation pattern of the antenna and will complicate our analysis techniques. To avoid confusion we will now define a region of interest between 55° and 85° that we will use for scientific observation.

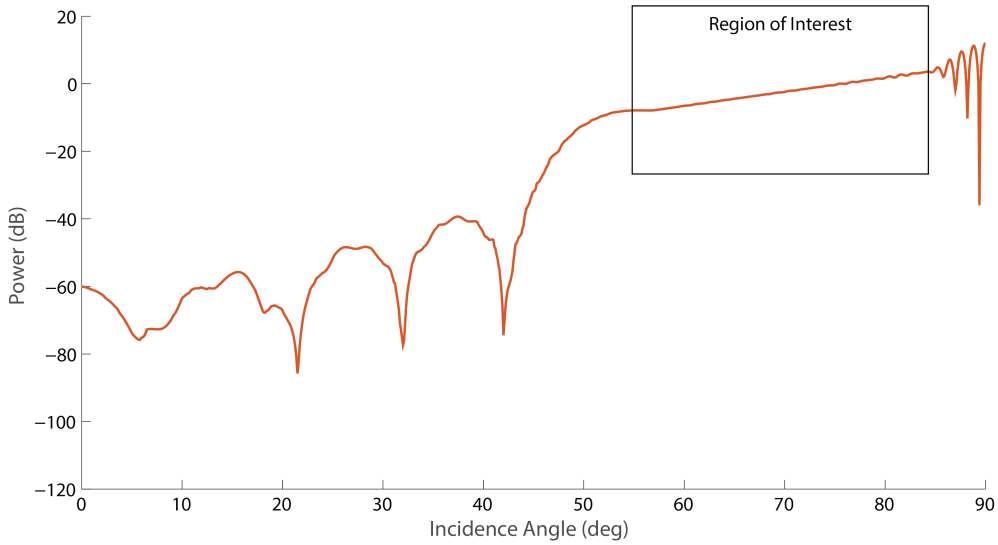

Figure 66. Reflected signal power received by MSL HGA with a hard stop at -35°.

Examining this region of interest more closely we can now look at what happens when we change the relative permittivity of the top soil. For consistency with earlier chapters we will choose various values of ε_1 which correspond to a sandy soil with water content ranging from 0% to 10% weight water. Using a shading profile which fades from dry sand ($\varepsilon_1 = 2.34 - 0.01i$, 0% water, lightest color) to wet sand ($\varepsilon_1 = 5.15 - 0.85i$, 10% water, darkest color) in Figure 67 we observe a gradual shift in the location of the Brewster angle and a change in the magnitude of the received signal near 55°. This leads us to conclude that MSL or Mars 2020 would be able to

measure the relative permittivity of the soil simply by pointing the antenna down and searching for the Brewster angle.

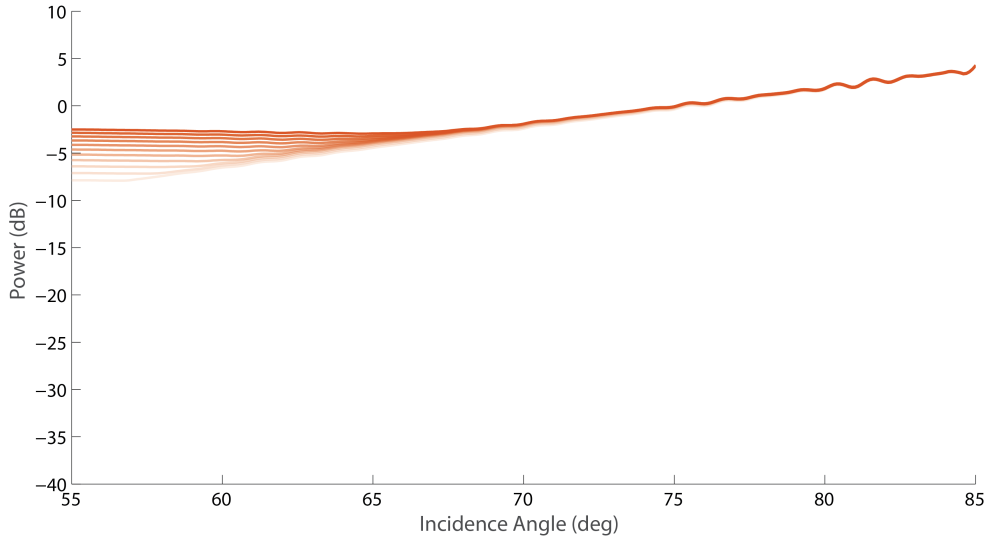

Figure 67. Reflected signal power received by MSL HGA from various one-layer soil models with different relative permittivities.

Next, we look at our two-layer soil model to understand what the signal reflection would look like if there is a dielectric discontinuity in the subsurface. In Figure 68 we start at a depth of 9 cm (lightest color) and step up to a depth of 10 cm (darkest color) in 1 mm increments. Here we see the tell-tale interference pattern caused by the reflection from multiple soil layers. However, note that the distance between the nulls is much closer than it was in our laboratory experiments. This is due to additional interference caused by the direct ray path being received though the sidelobes of the antenna.

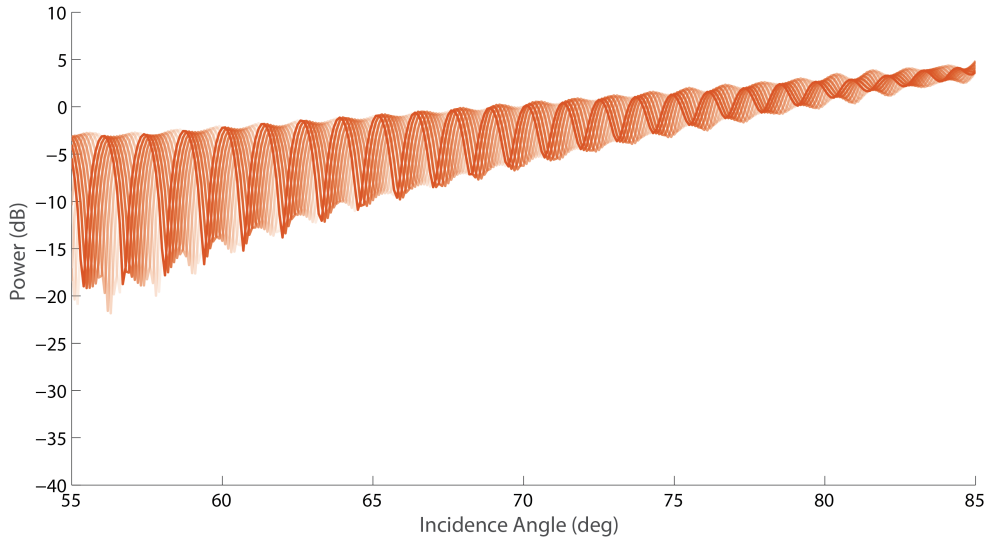

Figure 68. Reflected signal power received by MSL HGA from various two-layer soil models with different soil depths.

In Figure 69, we see the null spacing as a function of the layer depth for the MSL High Gain Antenna. While the MSL HGA may not be as sensitive to the layer depth as our model results showed in Chapter 4, it can still be used to constrain the thickness of the top layer. From these results, we believe this measurement has merit as a technical demo and could be used to identify the presence of layering up to 3 meters in depth.

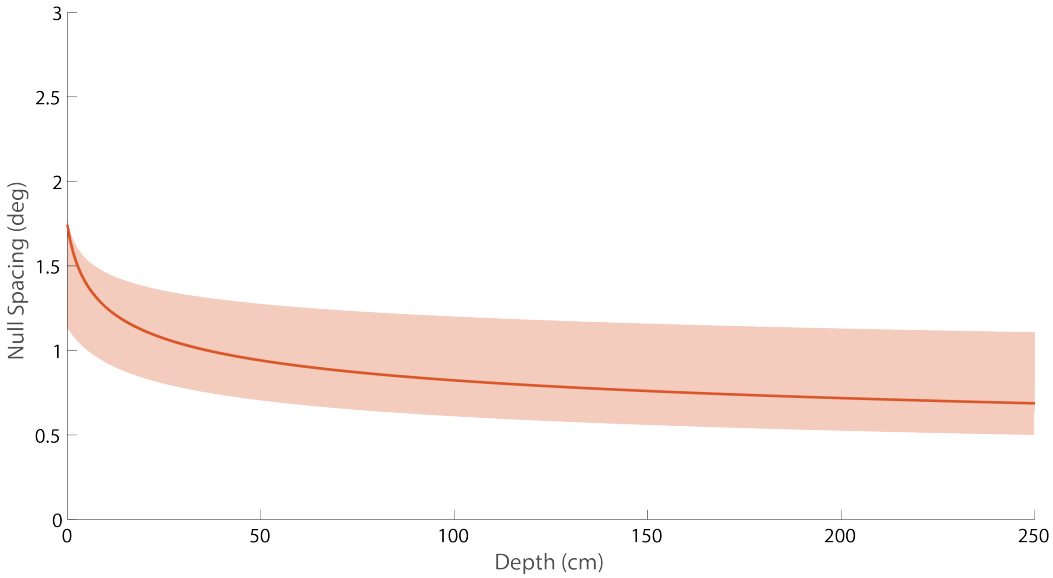

Figure 69. Relationship between the null spacing and layer depth derived from the model for the MSL HGA.

Chapter 7. Conclusions

We have developed and validated a ray tracing model that considers the relative position, orientation and velocity of two antennas and calculates the power transferred from one to the other. In addition to the direct path, this ray tracing model accounts for multi-signal reflection from the surface and subsurface layers as well. Another unique aspect of this model is the ability to look at different antenna designs and orientations. We allow the user to input the frequency, radiation pattern and orientation of an antenna to create a vertical, horizontal, right hand or left hand circularly polarized signal. This allows greater flexibility in instrument design than previous GNSS-R based models. Users are now free to explore the pros and cons of different antenna systems and mounting configurations.

In addition to the model formulation, we have explored the potential to conduct bistatic radar measurements of soil properties using a common spacecraft telecommunications system. In the two cases studied, we showed that the Deep Space Network in combination with the Small Deep Space Transponder on a Mars rover can be used to measure the relative permittivity of a soil and identify the presence of subsurface layering. The relative permittivity is of interest as it is directly related to the soil water content and an observation of a layered soil can help to characterize the environment around a spacecraft and identify both potential hazards and regions of interest for further assessment. Ultimately, this type of measurement could help in the assessment of the past and present-day habitability of Mars.

In future work, we would like to investigate the application of this technique to measurements from an orbiter. We envision this technique being especially effective for spacecraft altimetry and ranging. This could be an alternative ranging method for small spacecraft which may not have the mass or power allocation necessary to support a dedicated radar or lidar instrument. Work is already under way to see if this technique could be utilized by Mars Helicopter which is due to fly as a piggyback payload on the Mars 2020 rover. While we have conducted experiments with a network analyzer in the laboratory, no dedicated instrument has yet been built to conduct measurements of this type and at X-band frequencies. We intend to continue building hardware and pursuing the maturation of this promising methodology.

References

Altheide, T., Chevrier, V., Nicholson, C., & Denson, J. (2009). Experimental investigation of the stability and evaporation of sulfate and chloride brines on Mars. *Earth and Planetary Science Letters*, *282*(1), 69-78.

Beckmann, Petr. "Scattering of light by rough surfaces." *Progress in optics* 6 (1967): 53-69.

Briggs, G. (2000). Follow the water. *Meteoritics & Planetary Science*, *35*(5), 892-893.

Cadogan, D., Sandy, C., & Grahne, M. (2002). Development and evaluation of the mars pathfinder inflatable airbag landing system. *Acta Astronautica*, *50*(10), 633-640.

Calhoun, M., Huang, S., & Tjoelker, R. L. (2007). Stable photonic links for frequency and time transfer in the deep-space network and antenna arrays. *Proceedings of the IEEE*, *95*(10), 1931-1946.

Chevrier, V. F., Hanley, J., & Altheide, T. S. (2009). Stability of perchlorate hydrates and their liquid solutions at the Phoenix landing site, Mars. *Geophysical Research Letters*, *36*(10).

Chevrier, V. F., and Altheide, T. S. (2008). "Low temperature aqueous ferric sulfate solutions on the surface of Mars." *Geophysical Research Letters* 35(22).

Chinnery, H. E., Hagermann, A., Kaufmann, E., & Lewis, S. R. (2018). The penetration of solar radiation into carbon dioxide ice. *Journal of Geophysical Research: Planets*, *123*(4), 864-871.

Clifford, S. M. (1993). A model for the hydrologic and climatic behavior of water on Mars. *Journal of Geophysical Research: Planets*, *98*(E6), 10973-11016.

Cockell, C. S., et al. "Habitability: a review." *Astrobiology* 16.1 (2016): 89-117.

Corbel, C., Hamram, S., Ney, R., Plettemeier, D., Dolon, F., Jeangeot, A., ... & Berthelier, J. (2006, December). WISDOM: an UHF GPR on the Exomars Mission. In *AGU Fall Meeting Abstracts*.

Cuzzi, J. N., & Muhleman, D. O. (1972). The microwave spectrum and nature of the subsurface of Mars. *Icarus*, *17*(2), 548-560.

Davis, J. L., & Chudobiak, W. J. (1975). In situ meter for measuring relative permittivity of soils. *Geol. Surv. Can. Pap*, *75*(1A), 75-79.

Elliott, H. M., & Renno, N. O. (2015). Measurements of Dielectric Discontinuities in Planetary Subsurfaces with a Passive Instrument. In *AGU Fall Meeting 2015*.

Elliott, H. M., Martinez, G. M., Halleaux, D. G., Braswell, S. F., & Renno, N. O. (2012). The Michigan Mars Environmental Chamber (MMEC): Determining the conditions at which liquid brines form on Mars. In *Lunar and Planetary Science Conference* (Vol. 43).

Elliott, H. M., Renno, N. O., Preston, R. A., Ruf, C. S., Oudrhiri, K., Hensley, S., & Tamppari, L. (2014). A Novel Bistatic Radar and Radiometer to Investigate Shallow Planetary Subsurfaces. *AGU Fall Meeting 2014.*

Fischer, E., Martinez, G., Elliott, H. M., Borlina, C., & Renno, N. O. (2013, December). The Michigan Mars Environmental Chamber: Preliminary Results and Capabilities. In *AGU Fall Meeting Abstracts*.

Fischer, E., Martinez, G., Elliott, H., Borlina, C., & Renno, N. (2014, May). Experimental Demonstration of the Formation of Liquid Brines under Martian Polar Conditions in the Michigan Mars Environmental Chamber. In *EGU General Assembly Conference Abstracts* (Vol. 16).

Fischer, E., Martínez, G. M., Elliott, H. M., & Rennó, N. O. (2014). Experimental evidence for the formation of liquid saline water on Mars. *Geophysical research letters*, *41*(13), 4456-4462.

Fouchet, T., Lellouch, E., Ignatiev, N. I., Forget, F., Titov, D. V., Tschimmel, M., ... & Encrenaz, T. (2007). Martian water vapor: Mars Express PFS/LW observations. *Icarus*, *190*(1), 32-49.

Gough, R. V., Chevrier, V. F., & Tolbert, M. A. (2014). Formation of aqueous solutions on Mars via deliquescence of chloride–perchlorate binary mixtures. *Earth and Planetary Science Letters*, *393*, 73-82.

Gough, R. V., Chevrier, V. F., Baustian, K. J., Wise, M. E., & Tolbert, M. A. (2011). Laboratory studies of perchlorate phase transitions: Support for metastable aqueous perchlorate solutions on Mars. *Earth and Planetary Science Letters*, *312*(3), 371-377.

Grant, J. A., Schutz, A. E., & Campbell, B. A. (2003). Ground-penetrating radar as a tool for probing the shallow subsurface of Mars. *Journal of Geophysical Research: Planets*, *108*(E4).

Haberle, R. M., McKay, C. P., Schaeffer, J., Cabrol, N. A., Grin, E. A., Zent, A. P., & Quinn, R. (2001). On the possibility of liquid water on present-day Mars (Paper 2000JE001360). *Journal of Geophysical Research, 106*(10; SECT 5), 23-317.

Hamran, S. E., Berger, T., Brovoll, S., Damsgård, L., Helleren, Ø., Øyan, M. J., ... & Mellon, M. (2015, July). RIMFAX: A GPR for the Mars 2020 rover mission. In *Advanced Ground Penetrating Radar (IWAGPR), 2015 8th International Workshop on* (pp. 1-4). IEEE.

Hallikainen, M. T., Toikka, M. V. O., & Hyyppa, J. M. (1988). Microwave dielectric properties of low-salinity sea ice. In *Geoscience and Remote Sensing Symposium, 1988. IGARSS'88. Remote Sensing: Moving Toward the 21st Century., International* (Vol. 1, pp. 419-420). IEEE.

Hallikainen, M., & Winebrenner, D. P. (1992). The physical basis for sea ice remote sensing. *Microwave remote sensing of sea ice*, 29-46.

Hecht, M. H. (2002). Metastability of liquid water on Mars. *Icarus*, *156*(2), 373-386.

Hecht, M. H., Kounaves, S. P., Quinn, R. C., West, S. J., Young, S. M. M., Ming, D. W., ... & DeFlores, L. P. (2009). Detection of perchlorate and the soluble chemistry of martian soil at the Phoenix lander site. *Science*, *325*(5936), 64-67.

Henderson-Sellers, Ann, and A. J. Meadows. "The evolution of the surface temperature of Mars." *Planetary and Space Science* 24.1 (1976): 41-44.

Hoekstra, P., & Cappillino, P. (1971). Dielectric properties of sea and sodium chloride ice at UHF and microwave frequencies. *Journal of Geophysical Research*, *76*(20), 4922-4931.

Holt, J. W., Safaeinili, A., Plaut, J. J., Head, J. W., Phillips, R. J., Seu, R., ... & Biccari, D. (2008). Radar sounding evidence for buried glaciers in the southern mid-latitudes of Mars. *Science*, *322*(5905), 1235-1238.

IEEE Standard Letter Designations for Radar-Frequency Bands," in *IEEE Std 521-2002 (Revision of IEEE Std 521-1984)*, pp. 1-3, 2003 doi: 10.1109/IEEESTD.2003.94224

Imbriale, William A. *Large antennas of the deep space network*. Vol. 1. John Wiley & Sons, 2005.

Ingersoll, A. P. (1970). Mars: Occurrence of liquid water. *Science*, *168* (3934), 972-973.

Jakosky, Bruce M., and Robert M. Haberle. "The seasonal behavior of water on Mars." *Mars* (1992): 969-1016.

Jones, E. G., & Lineweaver, C. H. (2010). To what extent does terrestrial life “follow the water”?. *Astrobiology*, *10*(3), 349-361.

Jones, E. G., & Lineweaver, C. H. (2012). Using the phase diagram of liquid water to search for life. *Australian Journal of Earth Sciences*, *59*(2), 253-262.

Kounaves, S. P., Chaniotakis, N. A., Chevrier, V. F., Carrier, B. L., Folds, K. E., Hansen, V. M., ... & Weber, A. W. (2014). Identification of the perchlorate parent salts at the Phoenix Mars landing site and possible implications. *Icarus*, *232*, 226-231.

Kounaves, S. P., Hecht, M. H., Kapit, J., Gospodinova, K., DeFlores, L., Quinn, R. C., ... & Ming, D. W. (2010). Wet Chemistry experiments on the 2007 Phoenix Mars Scout Lander mission: Data analysis and results. *Journal of Geophysical Research: Planets*, *115*(E1).

Larson, K. M., Gutmann, E. D., Zavorotny, V. U., Braun, J. J., Williams, M. W., & Nievinski, F. G. (2009). Can we measure snow depth with GPS receivers?. *Geophysical Research Letters*, *36*(17).

Ludwig, A. C. (1973). The definition of cross-polarization, *IEEE Trans. Antennas Propagat.*, vol. AP-21, 116-119.

Mahaffy, P. R., Webster, C. R., Atreya, S. K., Franz, H., Wong, M., Conrad, P. G., ... & Owen, T. (2013). Abundance and isotopic composition of gases in the Martian atmosphere from the Curiosity rover. *Science*, *341*(6143), 263-266.

Makovsky, A., Ilott, P., & Taylor, J. (2009). Mars science laboratory telecommunications system design. Descanso Design and Performance Summary Series, Article, 14.

Martínez, G. M., and Nilton O. Renno. "Water and brines on Mars: current evidence and implications for MSL." *Space Science Reviews* 175.1-4 (2013): 29-51.

Martínez, G. M., N. O. Renno, and H. M. Elliott. "The evolution of the albedo of dark spots observed on Mars polar region." *Icarus* 221.2 (2012): 816-830.

Martínez, G. M., Newman, C. N., De Vicente-Retortillo, A., Fischer, E., Renno, N. O., Richardson, M. I., ... & Harri, A. M. (2017). The Modern Near-Surface Martian Climate: A Review of In-situ Meteorological Data from Viking to Curiosity. *Space Science Reviews*, 1-44.

Matsuoka, T., Fujita, S., & Mae, S. (1996). Effect of temperature on dielectric properties of ice in the range 5–39 GHz. *Journal of Applied Physics*, *80*(10), 5884-5890.

McConnell, S. (2018, October 8). About the Deep Space Network. https://deepspace.jpl.nasa.gov/about/

McKay, D. S., Gibson Jr, E. K., Thomas-Keprta, K. L., & Vali, H. (1996). Search for past life on Mars: possible relic biogenic activity in Martian meteorite ALH84001. *Science*, *273*(5277), 924.

Mironov, V.L.; Kosolapova, L.G.; Fomin, S.V. (2009) Physically and mineralogically based spectroscopic dielectricmodel for moist soils. *IEEE Trans. Geosci. Remote Sens.,* 47, 2059–2070.

Mironov, V. L., De Roo, R. D., & Savin, I. V. (2010). Temperature-dependable microwave dielectric model for an arctic soil. *IEEE Transactions on Geoscience and Remote Sensing*, *48*(6), 2544-2556.

Möhlmann, D. (2010). The three types of liquid water in the surface of present Mars. *International Journal of Astrobiology*, *9*(1), 45-49.

Mouginot, J., Pommerol, A., Beck, P., Kofman, W., & Clifford, S. M. (2012). Dielectric map of the Martian northern hemisphere and the nature of plain filling materials. *Geophysical research letters*, *39*(2).

Mullins, C. E. (1977). Magnetic susceptibility of the soil and its significance in soil science–a review. *European Journal of Soil Science*, *28*(2), 223-246.

Naidu, S. P., Benner, L. A., Margot, J. L., Busch, M. W., & Taylor, P. A. (2016). Capabilities of Earth-based radar facilities for near-Earth asteroid observations. *The Astronomical Journal*, *152*(4), 99.

Nikolakakos, G., & Whiteway, J. A. (2015). Laboratory investigation of perchlorate deliquescence at the surface of Mars with a Raman scattering lidar. *Geophysical Research Letters*, *42*(19), 7899-7906.

Nuding, D. L., Rivera-Valentin, E. G., Davis, R. D., Gough, R. V., Chevrier, V. F., & Tolbert, M. A. (2014). Deliquescence and efflorescence of calcium perchlorate: an investigation of stable aqueous solutions relevant to Mars. *Icarus*, *243*, 420-428.

Park, C. H., Behrendt, A., LeDrew, E., & Wulfmeyer, V. (2017). New Approach for Calculating the Effective Dielectric Constant of the Moist Soil for Microwaves. *Remote Sensing*, *9*(7), 732.

Pettinelli, E., Vannaroni, G., Cereti, A., Paolucci, F., Della Monica, G., Storini, M., & Bella, F. (2003). Frequency and time domain permittivity measurements on solid CO2 and solid CO2–soil mixtures as Martian soil simulants. *Journal of Geophysical Research: Planets*, *108*(E4).

Pozar, D. M. (1998). Microwave Engineering.

Rennó, N. O., Bos, B. J., Catling, D., Clark, B. C., Drube, L., Fisher, D., ... & Kounaves, S. P. (2009). Possible physical and thermodynamical evidence for liquid water at the Phoenix landing site. *Journal of Geophysical Research: Planets*, *114*(E1).

Rodriguez-Alvarez, N., Aguasca, A., Valencia, E., Bosch-Lluis, X., Ramos-Pérez, I., Park, H., ... & Vall-Llossera, M. (2011, July). Snow monitoring using GNSS-R techniques. In *Geoscience and Remote Sensing Symposium (IGARSS), 2011 IEEE International* (pp. 4375-4378). IEEE.

Rodriguez-Alvarez, N., Bosch-Lluis, X., Camps, A., Vall-Llossera, M., Valencia, E., Marchan-Hernandez, J. F., & Ramos-Perez, I. (2009). Soil moisture retrieval using GNSS-R techniques: Experimental results over a bare soil field. *IEEE Transactions on Geoscience and Remote Sensing*, *47*(11), 3616-3624.

Ruf, Christopher S., et al. "The CYGNSS nanosatellite constellation hurricane mission." *Geoscience and Remote Sensing Symposium (IGARSS), 2012 IEEE International*. IEEE, 2012.

Rust, A. C., Russell, J. K., & Knight, R. J. (1999). Dielectric constant as a predictor of porosity in dry volcanic rocks. *Journal of Volcanology and Geothermal Research*, *91*(1), 79-96.

Savijärvi, H. (1995). Mars boundary layer modeling: Diurnal moisture cycle and soil properties at the Viking Lander 1 site. *Icarus*, *117*(1), 120-127.

Scott, J. H. (1983). *Electrical and magnetic properties of rock and soil* (No. 83-915). US Geological Survey.

Sears, D. W., & Moore, S. R. (2005). On laboratory simulation and the evaporation rate of water on Mars. *Geophysical research letters*, *32*(16).
Soutsos, M. N., Bungey, J. H., Millard, S. G., Shaw, M. R., & Patterson, A. (2001). Dielectric properties of concrete and their influence on radar testing. *NDT & e International*, *34*(6), 419-425.

Slade, M. A., Benner, L. A., & Silva, A. (2011). Goldstone solar system radar observatory: Earth-based planetary mission support and unique science results. *Proceedings of the IEEE*, *99*(5), 757-769.

Stein, J., & Sandy, C. (2003). Recent developments in inflatable airbag impact attenuation systems for Mars exploration. *AIAA*, *1900*, 7-10.

Stillman, D.E., 2006, Frequency and Temperature Dependence in Electromagnetic Properties of Martian Analog Minerals., PhD thesis, Dept. of Geophysics, Colorado School of Mines, Golden, 199 p.

Taylor, J. Makovsky, A., Barbieri, A. Tung, R., Estabrook, P. Thomas, A.G., 2005, Article 10 Mars Exploration Rover Telecommunications, DESCANSO Design and Performance Summary Series, Jet Propulsion Laboratory, California Institute of Technology, Pasadena, CA.

Titov, D. V., Markiewicz, W. J., Thomas, N., Keller, H. U., Sablotny, R. M., Tomasko, M. G., ... & Smith, P. H. (1999). Measurements of the atmospheric water vapor on Mars by the Imager for Mars Pathfinder. *Journal of Geophysical Research: Planets*, *104*(E4), 9019-9026.

Ulaby, F. T., Bengal, T. H., Dobson, M. C., East, J. R., Garvin, J. B., & Evans, D. L. (1990). Microwave dielectric properties of dry rocks. *IEEE Transactions on Geoscience and Remote Sensing*, *28*(3), 325-336.

Ulaby, F. T., Moore, R. K., & Fung, A. K. (1981). Microwave Remote Sensing: Active and Passive. Vol. 1.

Ulaby, F. T., Long, D. G., Blackwell, W. J., Elachi, C., Fung, A. K., Ruf, C., ... & Van Zyl, J. (2014). *Microwave radar and radiometric remote sensing* (Vol. 4, No. 5, p. 6). Ann Arbor: University of Michigan Press.

Vacchione, J., Thelen, M., Brown, P., Hiang, J., Kelly, K., Cable, V., & Krishnan, S. (2014). *Antenna Designs for the Mars Exploration Rover (MER) Spacecraft, Lander, & Rover,* Presentation to IEEE, Los Angeles.

Vant, M. R., Gray, R. B., Ramseier, R. O., & Makios, V. (1974). Dielectric properties of fresh and sea ice at 10 and 35 GHz. *Journal of Applied Physics*, *45*(11), 4712-4717.

Vant, M. R., Ramseier, R. O., & Makios, V. (1978). The complex-dielectric constant of sea ice at frequencies in the range 0.1–40 GHz. *Journal of Applied Physics*, *49*(3), 1264-1280.

Wolff, S. E. (2003). Deep Space Network.

Xu, H., Li, B., Xu, S., & Feng, H. (2008, November). The measurement of dielectric constant of the concrete using single-frequency CW radar. In *Intelligent Networks and Intelligent Systems, 2008. ICINIS'08. First International Conference on* (pp. 588-591)

Zent, A. P., Hecht, M. H., Cobos, D. R., Wood, S. E., Hudson, T. L., Milkovich, S. M., ... & Mellon, M. T. (2010). Initial results from the thermal and electrical conductivity probe (TECP) on Phoenix. *Journal of Geophysical Research: Planets*, *115*(E3).